OPTICAL SENSORS FOR BACTERIA DETECTION BASED ON NANOSTRUCTURES FABRICATED BY DYNAMIC SHADOWING GROWTH

by

JUNXUE FU

(Under the Direction of Yiping Zhao)

ABSTRACT

Several optical sensors based on nanostructures for *Salmonella* detection have been developed by taking the advantage of the dynamic shadowing growth (DSG).

Based on fluorescence detection principle and the advantage of high surface area of nanorods, heterostructured silicon/gold nanorod array fabricated by DSG was functionalized with anti-*Salmonella* antibodies and organic dye molecules, which produced an enhanced fluorescence upon capture and detection of *Salmonella.*

To reduce the multiple functionalization steps, a simpler detection technique is explored on the basis of the localized surface plasmon resonance (LSPR) properties of Ag and Au nanoparticles (NPs). By using DSG technique, one can produce uniform Ag or Au NPs substrate with fine tunable LSPR wavelength. The sensor ability of Ag nanoparticles was demonstrated by detecting 10^{-10} M NeutrAvidin. Due to the better stability in aqueous solutions, Au nanoparticles were used as a LSPR sensor for the whole cell detection of *Salmonella*. The results showed a plasmon peak shift due to the *Salmonella* antigen and anti-*Salmonella* antibody binding. However, this shift was not sensitive to the concentration of the bacteria, which is due to the

rigid structure of the bacteria. A theoretical model based on Mie theory and Effective Medium theory has been proposed for this detection.

A more conventional method for bacteria detection is surface plasmon resonance (SPR) sensor. Ag nanorod mediated SPR sensor for sensitivity enhancement was first investigated using four-layer Fresnel equations and effective medium theory. Compared to the conventional thin metal film SPR configuration, the nanorod mediated SPR sensor presented a larger resonance angle shift and the sensitivity increased with increasing refractive index of the target analyte. The experimental results of Ag film and Ag nanorods/film fabricated by DSG in air and distilled water were analyzed by the theoretical results.

In summary, the optical sensors, such as fluorescence immunosensor, LSPR sensor and SPR sensor, based on nanorods or NPs fabricated by DSG technique have shown promising results for bio-molecules and bacteria detection. Also, the unique properties of the nanostructures have great potential for further improvement.

INDEX WORDS: dynamic shadowing growth, glancing angle deposition, oblique angle deposition, nanorod, nanoparticle, fluorescence, localized surface plasmon resonance, surface plasmon resonance, sensor, *Salmonella* detection

OPTICAL SENSORS FOR BACTERIA DETECTION BASED ON NANOSTRUCTURES FABRICATED BY DYNAMIC SHADOWING GROWTH

by

JUNXUE FU

B.S., Northern Jiao Tong University, 2000

A Dissertation Submitted to the Graduate Faculty of The University of Georgia in Partial Fulfillment of the Requirements for the Degree

DOCTOR OF PHILOSOPHY

ATHENS, GEORGIA

2009

OPTICAL SENSORS FOR BACTERIA DETECTION BASED ON NANOSTRUCTURES FABRICATED BY DYNAMIC SHADOWING GROWTH

by

JUNXUE FU

Major Professor: Yiping Zhao

Committee: William S. Kisaalita
Bosoon Park
Zhengwei Pan
Susanne Ullrich

Electronic Version Approved:

Maureen Grasso
Dean of the Graduate School
The University of Georgia
August 2009

ACKNOWLEDGEMENTS

This is a great opportunity to express my respect to my advisor, Dr. Yiping Zhao, for his generous support, encouragement and supervision throughout my Ph.D. study. Dr. Zhao is a diligent and scholarly mentor. His invaluable suggestions and guidance enabled me to accomplish these research projects. His creative thinking and careful attitude towards research inspired me a lot.

I would like to thank my committee, Dr. Bosoon Park, Dr. William Kissalita, Dr. Susanne Ullrich and Dr. Zhengwei Pan, for their guidance and support throughout this study.

I am also highly thankful to Dr. Ralph Tripp, Dr. Les Jones, Dr. Greg Siragusa, for their valuable suggestions regarding these research projects. And I really appreciate the kindness of Ms. Johnna Garrish, who was willing to help me and answer my questions without hesitation.

I am pleased to thank all my labmates, Dr. Yuping He, Dr. Jianguo Fan, Dr. Vivien Chu, Dr. Yu Zhu, Yongjun Liu, Zhongyue Zhang, Justin Abell, Wilson Smith, John Gibbs, for the teamwork. I always enjoyed the discussions with them.

TABLE OF CONTENTS

Page

ACKNOWLEDGEMENTS iv

LIST OF TABLES vii

LIST OF FIGURES viii

CHAPTER

1 INTRODUCTION 1

1.1 Overview of current *Salmonella* detection methods 1

1.2 Overview of different optical sensors for *Salmonella* detection 3

1.3 Dynamic shadowing growth 28

2 AU/SI HETERO-NANOROD-BASED SENSOR FOR *SALMONELLA* DETECTION 33

2.1 Introduction 33

2.2 Experimental Methods 33

2.3 Results and Discussion 37

2.4 Conclusions 46

3 LOCALIZED SURFACE PLASMON RESONANCE SENSOR BASED ON NANOPARTICLES FABRICATED BY DYNAMIC SHADOWING GROWTH 48

3.1 Introduction 48

3.2 Localized surface plasmon resonance property of Ag nanoparticles fabricated by dynamic shadowing growth 48

3.3 Ag nanoparticle based localized surface plasmon resonance biosensor for biotin-neutravidin interaction 60
3.4 Au nanoparticle based localized surface plasmon resonance biosensor for *Salmonella* detection 66
3.5 Conclusion 83
4 AG NANOROD MEDIATED SURFACE PLASMON RESONANCE SENSOR FOR *SALMONELLA* DETECTION 86
4.1 Introduction 86
4.2 Effective medium theory based Ag nanorod mediated SPR sensor 87
4.3 Experimental investigation of Ag nanorod mediated SPR sensor 104
4.4 Conclusion 117
5 CONCLUSIONS AND FUTURE WORK 119
REFERENCES 123
APPENDICES 135
A ABSORPTION EFFICIENCY OF METAL SPHERE BY MIE THEORY 135
B MAXWELL-GARNETT THEORY AND BRUGGEMAN'S THEORY 142
C FRESNEL EQUATION OF THREE-LAYER STRUCTURE CONTAINING AN ANISOTROPIC LAYER 147

LIST OF TABLES

Page

Table 4.1: Comparison of the Q-factor between Ag film and Ag nanorods / film 113

LIST OF FIGURES

Page

Figure 1.1: *Salmonella* observed under the optical microscope (Olympus BX60, 100×) 1

Figure 1.2: Morse potential curve of the diatomic molecule 5

Figure 1.3: Illustration of the potential energy curves of ground and excited states 6

Figure 1.4: Jablonski diagram 8

Figure 1.5: Relaxation from higher vibrational state to lower vibrational state 9

Figure 1.6: Process of a typical fluorescence based immunosensor 10

Figure 1.7: Structures of FITC and Alexa 488 dye 10

Figure 1.8: Fluorescence image of *Salmonella* bacteria bound by FITC labeled anti-*Salmonella* antibodies 11

Figure 1.9: A surface plasmon wave is propagating along the interface between a metal and a dielectric 12

Figure 1.10: Illustration of a *p*-polarized light incident on an interface between medium *a* and medium *m* 13

Figure 1.11: The dispersion of the surface plasmon $(\hbar\omega_p = 15eV)$ along the interface between medium *a* and medium *m* (solid line) and the dispersion of plane wave in medium *a* (dotted line). At short wavelength, the surface plasmon approaches asymptotically the frequency $\omega_{a2} = \frac{\omega_p}{\sqrt{2}}$ (dashed line) 16

Figure 1.12: Otto configuration for surface plasmon excitation 18

Figure 1.13: Curves ω_{am} - k_x and ω_{pm} - k_x are dispersions of surface plasmon along the interface between air and metal and between prism and metal, respectively. Lines ω_{a1} - k_x and ω_{p1} - k_x are the dispersions of plane waves in air and prism, respectively. Line ω_{pa} - k_x is dispersion of the evanescent wave in air with an incident angle θ 19

Figure 1.14: Kretschmann configuration for surface plasmon excitation.....20

Figure 1.15: Typical SPR reflectance curves by (a) angular interrogation at a fixed wavelength (632.8 nm) and (b) wavelength interrogation at a fixed incident angle (50°) 21

Figure 1.16: (a) Illustration of localized surface plasmon resonance. (b) A typical absorption spectrum of Ag nanoparticles.....24

Figure 1.17: (a) Illustration of the change of surrounding dielectric around the Au NPs. (b) The shift of absorbance spectra of Au NPs from ε = 1 to ε = 1.21.....26

Figure 1.18: (a) A schematic of oblique angle deposition setup. (b) and (c) Shadowing effect....28

Figure 1.19: SEM images of (a)-(b) the tilted Si nanocolumns and (c)-(d) the straight Si nanocolumns 30

Figure 2.1: Process flow for the *Salmonella* detection by bio-functionalized Au/Si nanorods. (a) Au/Si nanorods fabrication; (b) Dye immobilization onto Si nanorod; (c) Antibody conjugation onto Au tip; (d) *Salmonella* detection via the antibody-antigen reaction..34

Figure 2.2: (a) Typical TEM image of Au/Si nanorod. (b) Au distribution on the Si nanorods with different thickness of Au sputtering.....38

Figure 2.3: Fluorescence scans for Alexa 488 dye immobilization on silicon surface (532nm excitation / 526nm short pass emission filter). (a) Si film/Alexa 488; (b) Si nanorods; (c) Si nanorods/Alexa 488; (d) Au/Si nanorods/Alexa 488 39

Figure 2.4: UV-Vis spectrum of Si nanorods (square) and Au/Si nanorods before and after the fluorescein-5-isothiocyanate (FITC) dye immobilization (dot and triangle) 40

Figure 2.5: (a) Fluorescence image of Au/Si nanorods/Alexa488 (DNRs). (b) *Salmonella* observed under the optical microscope 41

Figure 2.6: Fluorescence images of (a) anti-*Salmonella*-DNR and (b) DNR treated *Salmonella* detection slides 42

Figure 2.7: Fluorescence scans for *Salmonella* slides by Typhoon scanner. (a) 50 μl anti-*Salmonella*-DNR with 2% BSA treated slide; (b) 50 μl DNR with 2% BSA treated slide; (c) 50 μl DNR (no BSA treatment) treated slide 42

Figure 2.8: Images for Salmonella detection. (a) 50 μl anti-*Salmonella*-DNR with 2% BSA treated slide under the fluorescence excitation (488 nm excitation); (b) 50 μl anti-*Salmonella*-DNR with 2% BSA treated slide under the white light; (c) 50 μl DNR with 2% BSA treated slide under the fluorescence excitation (488 nm excitation); (d) 50 μl DNR with 2% BSA treated slide under the white light. The inserts in Figure 2.8(a) and Figure 2.8(b) are the blow-up of the corresponding locations in the two images 43

Figure 2.9: TEM image of RSV antibody (131-2A)/Au/Si nanorods/FITC 45

Figure 2.10: *Respiratory syncytial virus* (RSV) infected cells detection by Au/Si hetero-nanorod-based biosensor. (a) ¼ bio-functional nanorods dilution was applied to the RSV infected cells; (b) ½ bio-functional nanorods dilution was applied to the RSV infected cells; (c) ¼ bio-functional nanorods dilution was applied to the uninfected cells; (d) ½ bio-functional nanorods dilution was applied to the uninfected cells 46

Figure 3.1: (a) A schematic of oblique angle deposition setup. (b) Sketch of polarized UV-Vis measurements 49

Figure 3.2: AFM images of representative Ag films on the glass substrates for different film thickness d and deposition angle θ 51

Figure 3.3: (a) The relationship between the particle diameter D and the film thickness d. (b) The relationship between the RMS roughness and the film thickness d for different deposition angle θ.....52

Figure 3.4: (a) The characteristic 2D power spectra of d = 35 nm, θ = 0° sample. (b) The characteristic 2D power spectra of d = 35 nm, θ = 85° sample. (c) The characteristic circular averaged power spectra of d = 10 nm at θ = 0° and 85°. (d) The characteristic circular averaged power spectra of 35 nm at θ = 0° and 85°.....54

Figure 3.5: The relationship between the averaged wavelength of the periodic morphology ζ and the film thickness d.....55

Figure 3.6: (a) Representative UV-Vis absorption spectra of Ag films at d = 5nm. (b) Representative UV-Vis absorption spectra of Ag films at d = 50nm.....56

Figure 3.7: The relationship between the SPRW λ_p and the film thickness d. (b) The relationship between the FWHM $\Delta\lambda$ and the film thickness d 57

Figure 3.8: (a) Typical polarized UV-Vis absorption spectra of the Ag film (d = 25 nm, θ = 80°). (b) The relationship between the SPRW ratio r_{ps} and the film thickness d 59

Figure 3.9: (a) Stability test for Ag nanoparticle film in DI water. (b) Stability test for SSC coated Ag nanoparticle film in DI water 61

Figure 3.10: Process flow for monitoring the specific binding of NeutrAvidin to Biotin on the Ag nanoparticle film.....63

Figure 3.11: (a) Representative absorption spectra of Biotin/NeutrAvidin binding process. (b) The SPRW λ_p shift during Biotin/NeutrAvidin binding process 64

Figure 3.12: Concentration dependence of NeutrAvidin for SPRW shift $\Delta\lambda_p$ 65

Figure 3.13: Absorbance spectra of Au NPs made by (a) OAD and (b) GLAD 67

Figure 3.14: (a) Normalized absorbance spectra of substrates A, A/B and A/B/A. A: Au NPs made by GLAD (QCM reading 30 nm). B: TiO_2 deposition by GLAD (QCM reading 5 nm). AFM images of substrates (b) A, (c) A/B and (d) A/B/A.....68

Figure 3.15: Relationship between the plasmon peak shift of Au NPs and (a) thickness of Ti d_{Ti} at θ_{Ti} = 0°; (b) deposition angles of Ti θ_{Ti} at d_{Ti} = 2 nm; (c) thickness of Ti d_{Ti} at θ_{Ti} = 85°. (d) A representative AFM image of Au nanoparticles (D = 30 nm) 70

Figure 3.16: Flow chart of Salmonella detection by Au NP based LSPR sensor.....71

Figure 3.17: (a) Absorbance spectrum (b) Plasmon peaks of Salmonella detection by LSPR sensor.....74

Figure 3.18: (a) SEM image (cross section) and (b) Fluorescence image of the Au nanoparticles substrate after 107 cfu/ml Salmonella detection 75

Figure 3.19: Absorbance spectra of (a) silica beads and (b) polystyrene coated Au nanoparticles substrates 76

Figure 3.20: (a) SEM top view image and (b) SEM cross section image of silica beads coated on Au nanoparticles substrates.....77

Figure 3.21: (a) Theoretical model of Polystyrene or silica bead detection by single Au NP. (b) The relationship between the plasmon peak shift $\Delta\lambda$ and the thickness of effective medium layer t.....80

Figure 3.22: (a) Theoretical model of Salmonella detection by single Au NP. (b) The relationship between the plasmon peak shift $\Delta\lambda$ and the thickness of effective medium layer t *Salmonella* observed under the optical microscope (Olympus BX60, 100×).....81

Figure 3.23: Dielectric constant of EML ε calculated from Maxwell-Garnett theory and Bruggeman theory 82

Figure 4.1: (a) A schematic of prism-metal film-nanorods-sensing layer model. (b) Incident plane and the plane defined by nanorods and normal direction of interface are all in the *xz* plane. The *x'*,*y'*,*z'* system has each axis parallel to one of the optical axes defined by the nanorod. (c) Multireflected ray in anisotropic nanorod layer.....87

Figure 4.2: (a) Representative SEM image of the cross section of Ag nanorods fabricated by OAD. (b) Representative AFM image of the Ag nanorods fabricated by OAD. (c) Bearing curve of the AFM image. (d) Geometry relationship between effective layer thickness d_e and tilting angle β, length of nanorod *l*, diameter of nanorod *D*.....93

Figure 4.3: (a) Typical nanorod mediated SPR curves with d_f = 40 nm, *D* = 30 nm at (a) *n* = 1.00 and (b) *n* = 1.33 96

Figure 4.4: (a) Reflectance minimum R_m, (b) SPR angle θ_r and (c) SPR curve width *w* as a function of length of nanorod *l* at *n* = 1.00. (d) Reflectance minimum R_m, (e) SPR angle θ_r and (f) SPR curve width *w* as a function of length of nanorod *l* at *n* = 1.33...97

Figure 4.5: (a) Reflectance minimum R_m, (b) SPR curve width *w* as a function of length of nanorod *l* at different film thickness d_f = 30, 40, 50 nm and diameter of nanorod *D* = 5, 10, 30 nm.....98

Figure 4.6: Dynamic range of nanorod mediated SPR sensor with d_f = 40nm at fixed diameter of nanorod (a) *D* = 5 nm, (b) *D* = 10 nm, (c) *D* = 30 nm. (d) Typical dynamic range at a fixed length of nanorod *l* = 20 nm.....100

Figure 4.7: Sensitivity *s* of nanorod mediated SPR sensor with d_f = 40 nm and *D* = 5, 10, 30 nm (a) from *n* = 1.00 to *n* = 1.05 and (b) from *n* = 1.30 to *n* = 1.34 101

Figure 4.8: (a) Sensitivity comparison between nanorod mediated SPR sensor and conventional SPR sensor, and (b) the corresponding SPR curves from n = 1.00 to n = 1.05 102

Figure 4.9: (a) Sensitivity comparison between nanorod mediated SPR sensor and conventional SPR sensor, and (b) the corresponding SPR curves from n = 1.30 to n = 1.34 102

Figure 4.10: Optical path of SPR sensor.....104

Figure 4.11: Side view of the dashed part in Figure 4.10.....105

Figure 4.12: Illustration of measurement method.....106

Figure 4.13: AFM images of (a) Ag film 40 nm and (b) Ag nanorods 200 nm on Ag film 40 nm. The thickness is the QCM reading and the scan size is 5 μm ×5 μm 107

Figure 4.14: SEM top views of Ag nanorods with a nominal thickness of (a) 200 nm; (b) 300 nm; (c) 600nm and (d) 800nm. The cross sections have been inserted on top of each image and have the same scale bar 108

Figure 4.15: (a) Top view of the prism and the sample (without the flow cell). (b) Side view of flow cell.....109

Figure 4.16: SPR reflectance curves of Ag film 40 nm.....110

Figure 4.17: Measurement orientations of the Ag nanorods/Ag film sample.....111

Figure 4.18: (a) SPR measurements in different orientations for Ag nanorods 200 nm/Ag film 40 nm sample. (b) SPR resonance angle vs. different locations for each orientation. 112

Figure 4.19: SPR reflectance curve of Ag film 50 nm/Ti film 1 nm (a) in air and (b) in water..113

Figure 4.20: SPR reflectance curve of Ag nanorods 200 nm/Ag film 50 nm/Ti film 1 nm in air114

Figure 4.21: Relationships between SPR angle or width and the thin film thickness 116

CHAPTER 1

INTRODUCTION

1.1 Overview of current *Salmonella* detection methods

Salmonella is a genus of rod-shaped, predominantly motile enterobacteria with diameters around 0.7 to 1.5 μm, lengths from 2 to 5 μm, as shown in Figure 1.1 This bacterium causes illnesses in humans and many animals, such as typhoid fever, paratyphoid fever, and the foodborne illness salmonellosis. Therefore, *Salmonella* contamination of food can cause big economic losses and most importantly be a threat to public health. Though various analytical methods have been developed to detect the *Salmonella* bacteria, the efficiency and the sensitivity of *Salmonella* detection still remains a challenging and crucial issue for food safety and security. The conventional microbiological technique, i.e. ISO method 6579 often requires up to 5-7 days to obtain a positive result. [1-5] These culture methods have been reported to show poor sensitivity for low-level contamination in samples.[6]

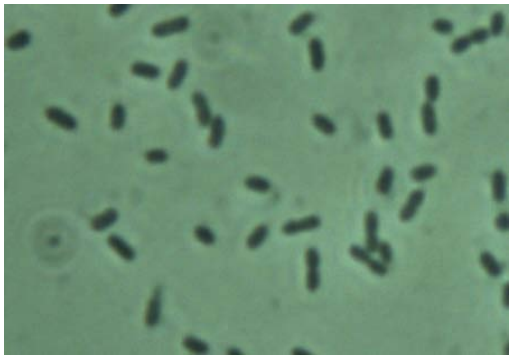

Figure 1.1 *Salmonella* observed under the optical microscope (Olympus BX60, 100×).

Several rapid detection methods have been developed over the past few years. Based on the specific binding reaction that occurs between an antibody and the antigen, fluorescent-antibody (FA) [7-11] and immunoassays including enzyme-linked immunosorbent assay (ELISA) [12-14] are widely used for *Salmonella* detection. The FA procedure is to label the anti-*Salmonella* antibody with fluorescence dyes and detect the Salmonella by examining the fluorescent signals. ELISA becomes more popular and this method measures the interaction between antibody and antigen with the aid of an enzyme-substrate reaction.[15-18] These ELISA methods are considered highly sensitive, and provide specific and rapid screening of large number of samples for presence of *Salmonella*. Some research reported that the detection sensitivity of the ELISA was 10^5 CFU (colony-forming unit) of *Salmonella* spp. (= species) per mi of culture.[14] Since the *Salmonella* numbers are usually low in the samples, the enrichment step, which takes hours, is usually necessary for immunoassays before the detection of pathogens.

Other methods that also provide accurate detection of *Salmonella* are based on the specific nucleic acid target sequence, such as the most popular technique, polymerase chain reaction (PCR).[19-21] PCR is based on isolating the bacteria and exponentially amplifying a DNA fragment or sequence of interest via enzymatic replication.[6, 22, 23] Among the PCR applications, Real-time PCR offers the advantage of semi-quantification of the bacterial DNA and no post-PCR handling of the sample thus reducing the risk of false-positive results.[4, 5, 24, 25] However, the first step in the genetic method is usually lysis of the cells and followed by purification of the released nucleic acid, which needs professional technique and personnel.

Biosensor development has shown great potential for rapid, real-time and high-throughput detection of *Salmonella* bacteria. Among them, the commercially available surface plasmon resonance sensors for *Salmonella* detection have been conveniently studied. [26-28]

Electrochemical biosensor has also been listed as one of the fast and sensitive method for *Salmonella* detection. [29, 30] By measuring the resonance frequency shift, quartz crystal microbalance and piezoelectric material based biosensors have indicated the potential to directly detect *Salmonella*. [31-33] Other alternative ways for bacteria detection are to measure the change of pH value,[34] interference fringe,[35] fluorescence intensity,[36, 37] magnetoelastic resonance,[38] electrical property[39] and chemiluminescence[40] caused by the bacteria-related binding events. The drawback of these biosensors is that most of these apparatus are highly sophisticated and expensive.

1.2 Overview of different optical sensors for *Salmonella* detection

An optical sensor is a device that measures an optical quantity, such as luminance, fluorescence, absorption, reflection and etc., from a detection process and converts it into a signal which can be read by an observer or by an instrument. Due to the unique physical or chemical properties of the nanostructures, the optical signal can be amplified and therefore the sensor sensitivity is enhanced. Recently, highly sensitive optical sensors based on nanostructures have shown great potential for pathogen detection. Among them, there are detections by luminescence using quantum dots,[41, 42] localized surface plasmon resonance of metallic nanoparticles,[43] enhanced fluorescence,[44] dye immobilized nanoparticle,[45, 46] or Raman reporter molecule immobilized metallic nanoparticles.[47] In this study, our target is to incorporate the nanostructures fabricated by dynamic shadowing growth into different optical sensors such as fluorescence immunosensor, surface plasmon resonance sensor and localized surface plasmon resonance sensor for *Salmonella* detection. To obtain a basic understanding of these sensors, their basic principles will be introduced in the following sections.

1.2.1 Basics of fluorescence

Fluorescence is widely used in the field of optical sensor application. It will be very informative to discuss the physical principle of fluorescence and introduce the basic fluorescence based immunosensor for bacteria detection.

1.2.1.1 Energy levels of molecules

Fluorescence is a luminance process where the molecule in the singlet state emits a photon upon the absorption of the excited photon. This process is based on the understanding of the energy levels of molecules. As we know, electrons of molecules only can take discrete energy values, which are defined as different electronic energy levels. They can be complicated since the electrons are moving in the electric field of two or more nuclei. In the case of diatomic molecules, the energy difference between the electronic energy states is given by [48]

$$E_{electronic} \sim \frac{\hbar^2}{md^2}, \tag{1.1}$$

where m is the mass of the electron, and d is the size of the molecule.

Within each of these electronic states, there are various vibrational states caused by relative motion of the electrons and the nuclei. To know the vibrational energy states, we need to solve the Schrödinger equation. For the diatomic molecule, Morse potential function is popularly used for the potential term in Schrödinger equation [49]:

$$V = D\{1 - \exp[-A(r - r_e)]\}^2, \tag{1.2}$$

where V is the potential, r_e is the equilibrium internuclear distance, D, called as electronic dissociation energy, and A are constants.

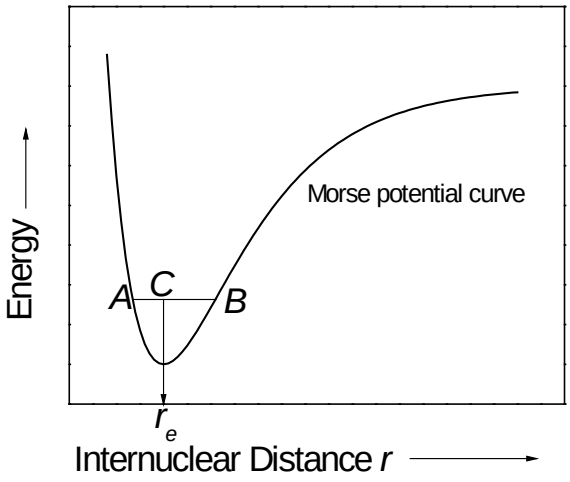

Figure 1.2 Morse potential curve of the diatomic molecule.

At a given vibrational energy level, due to the attractive force between the positive ion and the negative ion, the ions are moving towards each other. However, the repulsive forces between the two nuclei and between the electrons make the ions move apart. Therefore, the ions are vibrating along the axis of the molecule. Figure 1.2 shows a Morse potential curve of the diatomic molecule and the molecule vibrates between points A and B: at points A and B, the potential energy reaches maximum and the velocity is zero; at equilibrium position C, the velocity is maximum and the potential energy is zero. The energy E_v of the vibrational state can be solved as [49]:

$$E_v = h\nu_e(v+\frac{1}{2}) - \frac{h^2c}{4D}\nu_e{}^2(v+\frac{1}{2})^2,\ v = 0, 1, 2, 3, \ldots \qquad (1.3)$$

where $\nu_e = \frac{1}{2\pi}\sqrt{\frac{k}{\mu}}$ is the vibrational frequency of the molecule, k is the force constant, μ is the reduced mass of the system, v is vibrational quantum number. In equation (1.3), the first term is

the vibrational energy of the harmonic oscillator, and the second term is an anharmonic term, which is treated as a perturbation in most cases.

Besides the electronic and vibrational energy states, the molecules have rotational energy states, which is caused by the rotation of the whole molecule. Thus, the total energy of the molecule is: [48]

$$E_{total} = E_{electronic} + E_{vibrational} + E_{rotational}, \tag{1.4}$$

and the energy gaps between the adjacent electronic, vibrational or rotational energy levels are:

$$\Delta E_{electronic} = 10^2 \Delta E_{vibrational} = 10^4 \Delta E_{rotational}. \tag{1.5}$$

The wavelength corresponding to quantum transitions between electronic energy states, vibrational energy states and rotational energy states is ultraviolet and visible region, infrared region and microwave region, respectively. Compared to electronic and vibrational energy states, the spacing between rotational energy states is very small, therefore it is not concerned here.

1.2.1.2 Absorption and emission

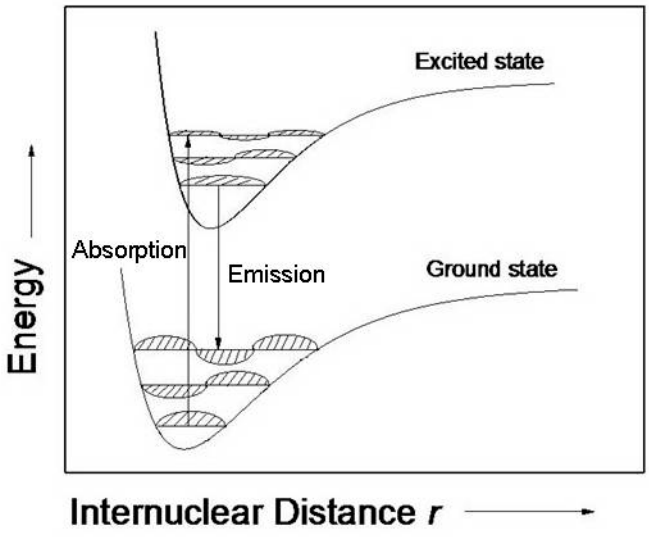

Figure 1.3 Illustration of the potential energy curves of ground and excited states.

Absorption of light is a quantum transition process to excite electrons from the lower energy states to higher energy states. By visualizing the molecule as an oscillating dipole, the quantized energy of the light can be absorbed when the resonance between the oscillating dipole and electromagnetic light wave occurs.

Figure 1.3 illustrates the potential energy curves of ground and excited states. These two energy wells are displaced from one another, reflecting the difference in the electronic structure of these states. Around the equilibrium position, since the potential curve of the molecule is similar to that of the harmonic oscillator, the eigen functions of the vibrational states can be analogous to the harmonic oscillations, as shown by the shaded area. Also, the shaded areas reflect the probability of where the electron would be if it were in that vibrational level. If the absorbed photon has more energy than needed for a simple electronic transition, the molecule jumps to one of the higher vibrational energy level in the excited state. Then usually the molecule will relax to the lowest vibrational energy level in the excited state, and lose some energy in the form of heat, due to that the energy spacing between the vibrational states is in the infrared wavelength region. After that, a photon may be emitted to make the molecule go back to the ground state. This process is called fluorescence. And the most favored transitions will be those in which the shaded areas of both the ground and excited states are a maximum, as shown in Figure 1.3. [50]

To describe the absorption and emission processes more clearly, Jablonski diagram is used to illustrate the transitions between the energy states. A typical Jablonski diagram is shown in Figure 1.4. In the beginning, the molecule stays at the singlet ground state S_0. When it absorbs (A) light energy, it is excited to an excited state S_n ($n > 0$). In about a picosecond or less, the molecule rapidly relaxes to the lowest vibrational energy level in the first excited state S_1, which

is called internal conversion (IC). Because the transition between electronic states falls in the visible and ultraviolet wavelength region, the molecule emits a photon to go back to the ground state, and this process is called fluorescence (F) emission. Since the molecule loses some energy before it emits the fluorescence photon, the emission wavelength is larger than the excitation wavelength. Also, the molecule can go through some non-radiative relaxation to go back to the ground state, such as dissipation as heat, fluorescence quenching with a second molecule. Another way to relaxation is phosphorescence (P) emission: the electron undergoes a spin conversion into a triplet state T_n ($n > 0$), a process know as intersystem crossing (ISC), and then emit a photon to return to the ground state, though the probability of this kind of relaxation is low.

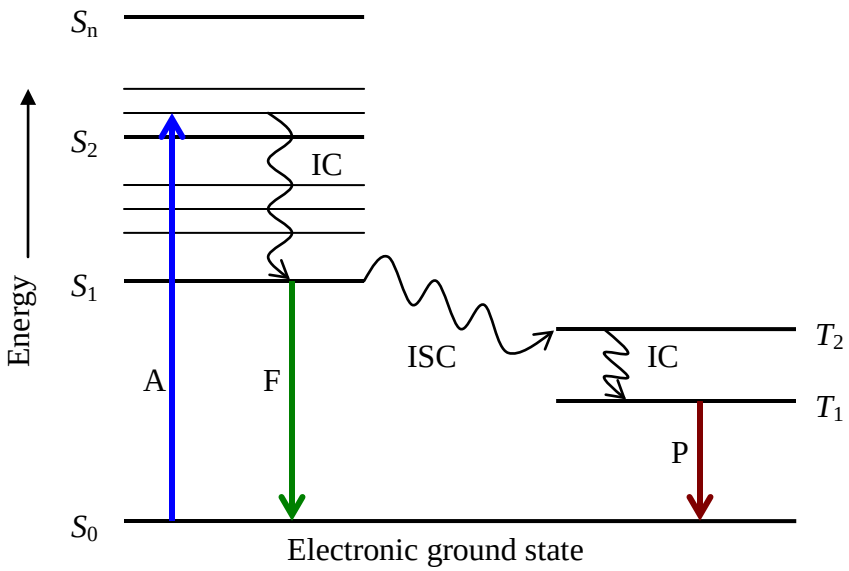

Figure 1.4 Jablonski diagram.

The relaxation from the higher vibrational state to the lower vibrational state in the excited state may be explained by the solvent effects.[50] As shown in Figure 1.5, the molecule, which has a given dipole moment with respect to the molecular axis, absorbs a photon and jumps from the ground state G to a higher vibrational energy level S_1 in excited state. Upon excitation,

which occurs in approximately 10^{-15} sec, the excited solute molecule has a dipole moment which is oriented differently from that of the ground state G. After approximately 10^{-10} sec, the nearby solvent molecules rearrange themselves into the most favorable alignment with the excited solute dipole. This results in a loss of the excited state energy and the solute molecules jump to the lower excited state S_1'. And then the solute molecule emits a photon and goes back to a vibrational energy level G' in about 10^{-9} sec. After the dipole moment rearrangement of the solvent molecules, the solute molecule returns to the original ground state G.

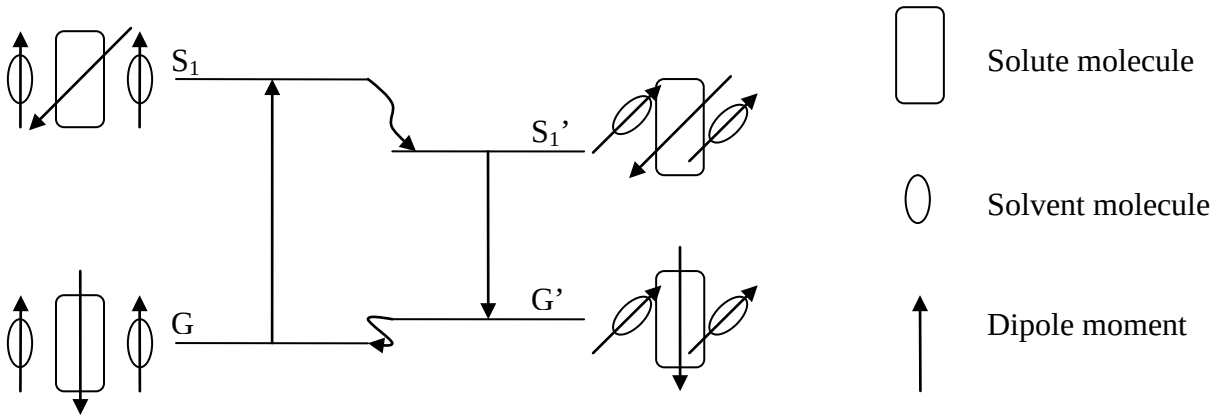

Figure 1.5 Relaxation from higher vibrational state to lower vibrational state.

1.2.1.3 Fluorescence based sensor

Fluorescence has provided a number of sensor applications in biological science especially in immunoassays. [51-54] There are two ways to observe the signal from a fluorescence based sensor. One is fluorescence spectroscopy, where the fluorescence intensity will be recorded as a function of the wavelength. Another is fluorescence imaging, where the fluorescence image will be seen by examining the dominant color (wavelength).

The most common process of fluorescence based immunosensor is illustrated as follows (Figure 1.6): (a) A fluorophore is attached to an antibody; (b) the fluorophore labeled antibody is

applied to the antigen; (c) the antigen bound with the antibody can be seen by the fluorescence upon the excitation.

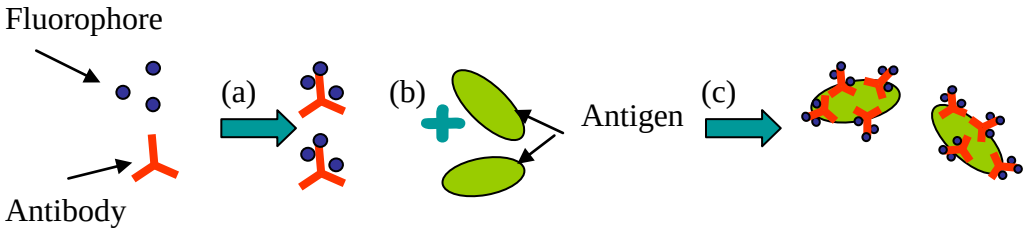

Figure 1.6 Process of a typical fluorescence based immunosensor

The fluorophore is a functional group in a molecule, which absorbs energy of the excitation light with a specifc wavelength and emits fluorescence at a longer wavelength. Fluorescein-5-isothiocyanate (FITC) has been one of the most common fluorophores chemically attached to non-fluorescent molecules, while new generations of fluorophores such as the Alexa Fluors is generally more photostable, brighter and less *p*H-sensitive. Figure 1.7 shows the chemical structures of FITC and Alexa 488 dye.

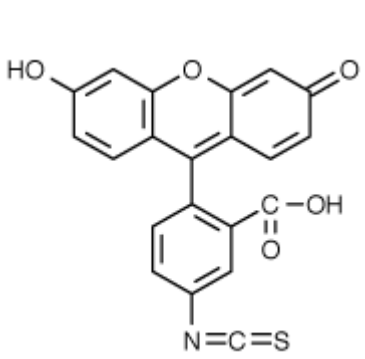

Fluorescein-5-isothiocyanate

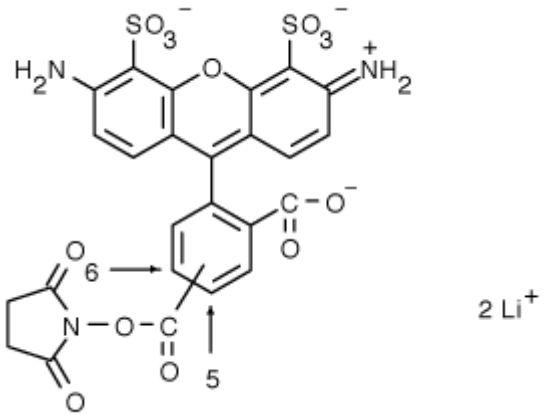

Alexa 488 carboxylic acid, succinimidyl ester

Figure 1.7 Structures of FITC and Alexa 488 dye.

As an example, the following fluorescence microscope image shows the *Salmonella* bacteria bound by FITC labeled anti-*Salmonella* antibodies, which make the elongated elliptical shape of the bacteria can be clearly seen (Figure 1.8).

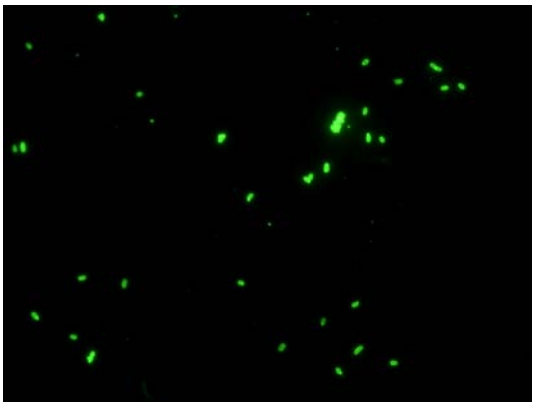

Figure 1.8 Fluorescence image of *Salmonella* bacteria bound by FITC labeled anti-*Salmonella* antibodies

1.2.2 Surface plasmon resonance based biosensor

As described above, the fluorescence based sensor is to observe the excited fluorescence signal by examining the reaction between the fluorophore labeled analyte and the target. As another popular optical sensor, surface plasmon resonance sensor is to directly observe the change of the reflection of the light when it interacts with the target. The sensor principle is discussed below.

1.2.2.1 Bulk plasmon

Metal is a lattice of positive ions surrounded by a sea of free electrons. Due to the ability of the electrons to move independently, they respond strongly to electromagnetic field and can perform a collective oscillation under certain condition. The plasmon is this collective excitation of the electron gas, a coherent oscillation of all of the electrons. The electrons oscillate back and forth at the plasma frequency, which is usually characterized as [55]

$$\omega_p = \sqrt{\frac{ne^2}{m\varepsilon_0}}, \tag{1.6}$$

where n is the conduction electron density, e is the elementary charge, m is the electron mass and ε_0 the permittivity of free space.

1.2.2.2 Surface plasmon wave

In the presence of a planar boundary between a metal and a dielectric, the plasmons are confined to the surface and called surface plasmons. As shown in Figure 1.9, under certain resonant conditions, the surface plasmons are excited and traveling along the interface (x direction). This charge density oscillation is called surface plasmon wave (SPW) and includes a longitudinal wave character,

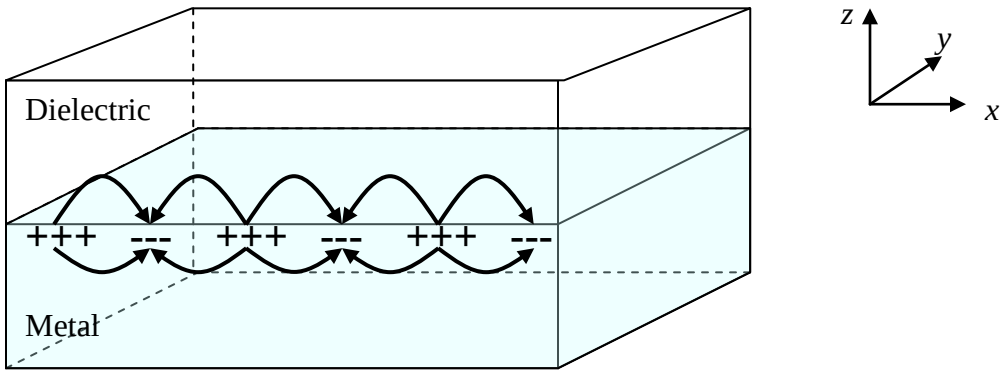

Figure 1.9 A surface plasmon wave is propagating along the interface between a metal and a dielectric.

A lot of work has been done to verify that the SPW is the solutions of Maxwell's equations as illustrated below with proper boundary conditions and constitute equations. [56, 57] As showing in Figure 1.10, a light beam incidents onto the interface between medium a (for example, air) and medium m (for example, metal), and the plane composed of the incident beam and refracted beam is defined as the incident plane. Since the s-polarized electric field of the

light (the oscillation direction of the electric field is perpendicular to the incident plane) is continuous at the interface, we only consider the *p*-polarized electric field of the light (the oscillation direction of the electric field is parallel to the incident plane). The wave vectors in the two media are:

$$k_j = \frac{\omega}{c}\sqrt{\varepsilon_j}\ ,\ \ j = a, m, \tag{1.7}$$

$$k_{jz}{}^2 = \frac{\omega^2}{c^2}\varepsilon_j - k_x{}^2,\ \ j = a, m, \tag{1.8}$$

where ω is the angular frequency of the incident light, ε is the dielectric constant and c is speed of light. The x component of the wave vector k_x is conserved due to the continuity of the tangential electric field.

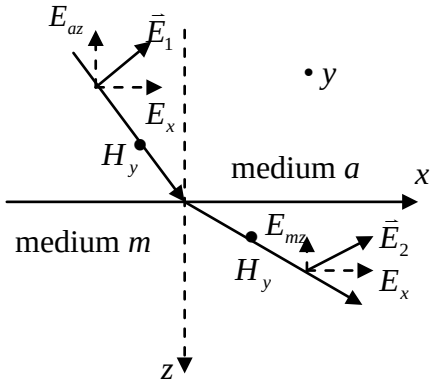

Figure 1.10 Illustration of a *p*-polarized light incident on an interface between medium *a* and medium *m*.

The generation of a SPW can be described as: a beam of *p*-polarized light incidents onto an interface of two different media, and then only propagates along the direction of the interface; the tangential components of the electric field, magnetic field and wave vector are continuous. Therefore, the components of the electric field and the magnetic field of the SPW can be written as:

$$\vec{E}_a = E_x e^{i(k_x x-\omega t)} e^{ik_{az} z}\hat{x} + E_{az} e^{i(k_x x-\omega t)} e^{ik_{az} z}\hat{z}\,, \tag{1.9}$$

$$\vec{E}_m = E_x e^{i(k_x x-\omega t)} e^{ik_{mz} z}\hat{x} + E_{mz} e^{i(k_x x-\omega t)} e^{ik_{mz} z}\hat{z}\,, \tag{1.10}$$

$$\vec{H}_a = H_y e^{i(k_x x-\omega t)} e^{ik_{az} z}\hat{y}\,, \tag{1.11}$$

$$\vec{H}_m = H_y e^{i(k_x x-\omega t)} e^{ik_{mz} z}\hat{y}\,. \tag{1.12}$$

If we apply Maxwell's equations

$$\nabla \cdot \vec{E} = 0\,, \tag{1.13}$$

$$\nabla \times \vec{E} = -\mu \frac{\partial H}{\partial t}\,, \tag{1.14}$$

we find

$$\frac{\varepsilon_a}{k_{az}} = \frac{\varepsilon_m}{k_{mz}}\,. \tag{1.15}$$

One should note that we start the derivation by examining an existed SPW and then obtain equation (1.15). In other word, to generate a SPW, the equation (1.15) must be fulfilled. Because the dielectric function of the metal has a negative real portion, whose magnitude is greater than that of the imaginary portion, the *z* components of the wave vectors in air and in metal should have opposite sign. Also, since SPW propagates along the interface and decays into both media, that the *z* component of the wave vector should be imaginary and $ik_{jz}z$ ($j = a, m$) should be negative:

$$k_{az} = -i\sqrt{k_x{}^2 - \frac{\omega^2}{c^2}\varepsilon_a}\,,\ z < 0, \tag{1.16}$$

$$k_{mz} = i\sqrt{k_x{}^2 - \frac{\omega^2}{c^2}\varepsilon_m}\,,\ z > 0. \tag{1.17}$$

We may substitute expressions for k_{az} and k_{mz} into equation (1.15), and obtain

$$k_x = \frac{\omega}{c}\sqrt{\frac{\varepsilon_a \varepsilon_m}{\varepsilon_a + \varepsilon_m}}. \tag{1.18}$$

Since ε_m is negative, $|\varepsilon_m| > \varepsilon_a$ is required for a real k_x. We also notice that $k_x^2 - \frac{\omega^2}{c^2}\varepsilon_m$ is automatically positive, while $(k_x^2 - \frac{\omega^2}{c^2}\varepsilon_a) > 0$ is required for an imaginary k_{az}, which is equivalent to

$$v_{SPW} = \frac{\omega}{k_x} < \frac{c}{\sqrt{\varepsilon_a}}, \tag{1.19}$$

where v_{SPW} is the phase velocity of SPW. This means the phase velocity of SPW should be less than that of plane waves in the medium *a*. In summary, the conditions for SPW excitation are $|\varepsilon_m| > \varepsilon_a$ and equations (1.18) and (1.19).

1.2.2.3 Generation of surface plasmon resonance

To generate a SPW, it is easy to have $|\varepsilon_m| > \varepsilon_a$, but efforts are needed to fulfill equation (1.19). If a light beam with an incident angle θ directly incident onto the interface, the velocity of points of fixed phase along the interface between media *a* and *m* is $\frac{c}{\sqrt{\varepsilon_a}\sin\theta}$, which is always larger than $\frac{c}{\sqrt{\varepsilon_a}}$. Therefore, the SPW can not be excited.

We first look into the dispersion relation of the SPW. Drude model gives a simple dielectric function of the metal as: [58]

$$\varepsilon_m = 1 - \frac{\omega_p^2}{\omega(\omega + i\eta)}, \tag{1.20}$$

where η is the damping constant, and is related to the average time τ between collisions of the electrons with lattice vibration by $\eta = 1/\tau$.. For most metals, η is much less than the bulk plasmon frequency ω_p at room temperature. Hence, substituting equation (1.20) into (1.18) yields

$$k_x = \frac{\omega}{c}\sqrt{\frac{\varepsilon_a\omega^2 - \varepsilon_a\omega_p^2}{\varepsilon_a\omega^2 + \omega^2 - \omega_p^2}}\,. \tag{1.21}$$

Therefore we have the dispersion relation between ω and k_x

$$\omega^2 = \frac{(\varepsilon_a\omega_p^2 + \varepsilon_a c^2 k_x^2 + c^2 k_x^2) \pm \sqrt{\Delta}}{2\varepsilon_a}, \tag{1.22}$$

where

$$\Delta = c^4 k_x^4(\varepsilon_a + 1)^2 + 2\varepsilon_a(\varepsilon_a - 1)c^2\omega_p^2 k_x^2 + \varepsilon_a^2\omega_p^4. \tag{1.23}$$

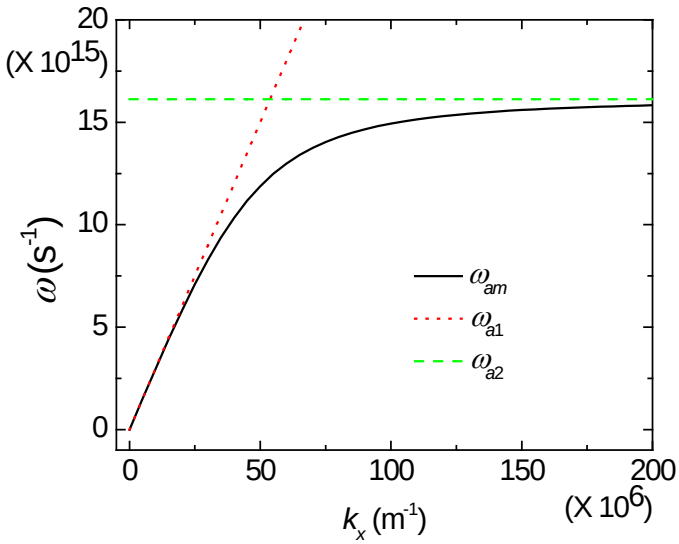

Figure 1.11 The dispersion of the surface plasmon ($\hbar\omega_p = 15eV$) along the interface between medium *a* and medium *m* (solid line) and the dispersion of plane wave in medium *a* (dotted line). At short wavelength, the surface plasmon approaches asymptotically the frequency $\omega_{a2} = \frac{\omega_p}{\sqrt{2}}$ (dashed line).

In the case of the interface between air and metal, ε_a =1, we have

$$\omega_{am}^2 = \frac{\omega_p^2}{2} + c^2 k_x^2 - \sqrt{\frac{\omega_p^4}{4} + c^4 k_x^4} \,. \tag{1.24}$$

The solution with "plus" sign has been omitted by considering equation (1.19). Also, the dispersion relation for a plane wave in the medium *a* (ε_a =1) is

$$\omega_{a1}^2 = \frac{c^2 k_x^2}{\varepsilon_a} = c^2 k_x^2 \,, \tag{1.25}$$

and for a large k_x,

$$\omega_{a2}^2 = \frac{\omega_p^2}{2} + c^2 k_x^2 - \sqrt{\frac{\omega_p^4}{4} + c^4 k_x^4} = \frac{\omega_p^2}{2} + c^2 k_x^2 - \sqrt{c^4 k_x^4} = \frac{\omega_p^2}{2} \,. \tag{1.26}$$

We have presented the dispersion relation ω_{am} - k_x ($\hbar\omega_p = 15eV$) in Figure 1.11 by a solid curve. The dotted line $\omega_{a1} = ck_x$ and the dashed line $\omega_{a2} = \frac{\omega_p}{\sqrt{2}}$ are asymptotic tangents.

Now let's consider the dispersion relation ω_{pm} - k_x of the SPW along the interface between another dielectric medium with a larger dielectric constant ε_p (for example, a prism) than ε_a and the metal. The shape of ω_{pm} - k_x is similar with ω_{am} - k_x though the asymptotic tangents are different. The dispersion relation for plane wave in the medium *p* is

$$\omega_{p1}^2 = \frac{c^2 k_x^2}{\varepsilon_p} \,. \tag{1.27}$$

For a large k_x,

$$\omega_{p2}^2 = \frac{(\varepsilon_p \omega_p^2 + \varepsilon_p c^2 k_x^2 + c^2 k_x^2) - (\sqrt{(\varepsilon_p c^2 k_x^2 + c^2 k_x^2)^2} + \delta_1)}{2\varepsilon_p} = \frac{\omega_p^2}{2} - \delta_2 \,, \tag{1.28}$$

where δ_1, δ_2 are positive real numbers.

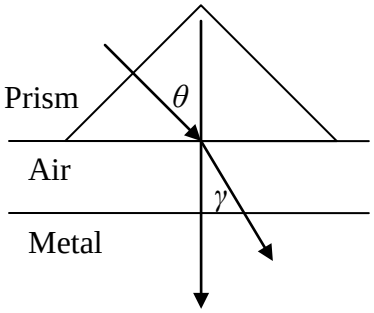

Figure 1.12 Otto configuration for surface plasmon excitation.

Otto firstly proposed a three layer structure composed of prism-air-metal to excite SPW, as shown in Figure 1.12. [59] If a *p*-polarized light beam incidents from medium *p* onto the surface of medium *a*, at some critical angle, the total reflection will occur due to $\varepsilon_p > \varepsilon_a$. According to Snell's law,

$$\sqrt{\varepsilon_p}\sin\theta = \sqrt{\varepsilon_a}\sin\gamma\,, \tag{1.29}$$

where γ is the refracted angle, the critical angle $\theta_c = \sin^{-1}\sqrt{\frac{\varepsilon_a}{\varepsilon_p}}$. If the incident angle θ is larger than the critical angle θ_c, we have

$$\sin\gamma = \sqrt{\frac{\varepsilon_p}{\varepsilon_a}}\sin\theta > \sqrt{\frac{\varepsilon_p}{\varepsilon_a}}\sin\theta_c = 1, \tag{1.30}$$

which results that cos γ is imaginary. Also, the *z* component of the wave vector

$$k_{pz} = \frac{\omega}{c}\sqrt{\varepsilon_p}\cos\gamma \tag{1.31}$$

becomes imaginary. As a result, the refracted wave propagates only parallel to the surface and is attenuated exponentially beyond the interface. This evanescent wave will be able to be resonant with the SPW at the air-metal interface if the conditions (1.18) and (1.19) can be fulfilled.

The velocity of points of fixed phase along the prism-air interface is

$$v_{pa} = \frac{\omega_{pa}}{k_x} = \frac{c}{\sqrt{\varepsilon_p}\sin\theta}, \tag{1.32}$$

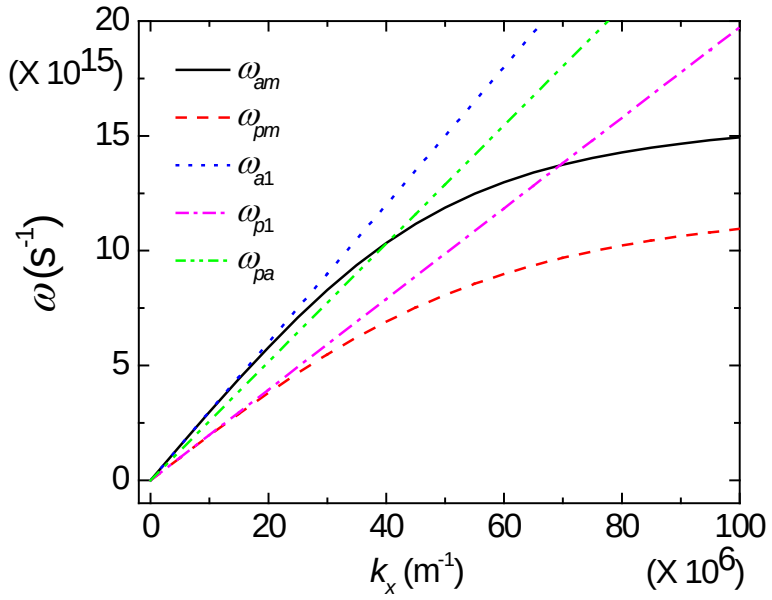

Figure 1.13 Curves ω_{am} - k_x and ω_{pm} - k_x are dispersions of surface plasmon along the interface between air and metal and between prism and metal, respectively. Lines ω_{a1} - k_x and ω_{p1} - k_x are the dispersions of plane waves in air and prism, respectively. Line ω_{pa} - k_x is dispersion of the evanescent wave in air with an incident angle θ.

which is plotted together with the dispersion relations ω_{am} - k_x and ω_{pm} - k_x, as shown in Figure 1.13. It can be seen that when $\sqrt{\frac{\varepsilon_a}{\varepsilon_p}} < \sin\theta < 1$, which is consistent with the excitation condition for the evanescent wave along the prism-air interface, the line ω_{pa} - k_x is between the dispersion lines ω_{a1} - k_x and ω_{p1} - k_x. So far, the equation (1.19) is satisfied. The cross point between ω_{pa} - k_x and ω_{am} - k_x means the resonance between the evanescent wave and the SPW at the air-metal interface, and the corresponding k_x will fulfill equation (1.18).

1.2.2.4 Principle of surface plasmon resonance based sensor

Since the thickness of air in Otto's model is hard to control, Kretschmann and Raether demonstrated another three layer structure composed of prism-metal-air, provided that the metal is thin enough to allow the evanescent wave to penetrate to the other side. This configuration is shown in Figure 1.14.

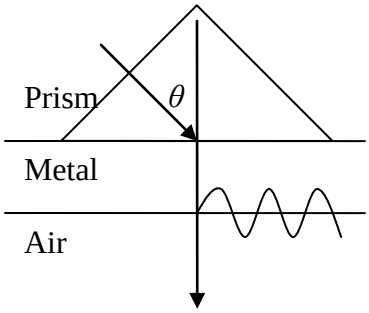

Figure 1.14 Kretschmann configuration for surface plasmon excitation.

We have successfully excited the SPW along the interface between the metal and the air either in Otto's configuration and the Kretschmann's configuration by producing a cross point between dispersion relation lines ω_{pa} - k_x and ω_{am} - k_x. The corresponding k_x means the resonance between the evanescent wave and the SPW at the interface. It is easy to write

$$k_x = \frac{\omega}{c}\sqrt{\varepsilon_p}\sin\theta, \tag{1.33}$$

therefore the SPR condition becomes

$$k_x = \frac{\omega}{c}\sqrt{\varepsilon_p}\sin\theta_{SPR} = \frac{\omega}{c}\sqrt{\frac{\varepsilon_m\varepsilon_a}{\varepsilon_m+\varepsilon_a}}. \tag{1.34}$$

The total reflectance from the three layer structure will be recorded, and a dip will be observed when SPR occurs since the energy of the incident light has been transferred to SPW.

There are two ways to manipulate the SPR configuration: angular interrogation is to fix the wavelength of the incident light thus fix the angular frequency ω, the dip will be found by scanning a range of incident angles and the angle corresponding to the dip position is called resonance angle θ_{SPR}; wavelength interrogation is to fix the incident angle and change the incident wavelength until the equation (1.18) is satisfied; and the wavelength corresponding to the dip position is called resonance wavelength λ_{SPR}. In either way, when the air is replaced by a sensing layer, which means the dielectric constant of the surrounding medium ε_a is changed, θ_{SPR} or λ_{SPR} will shift.

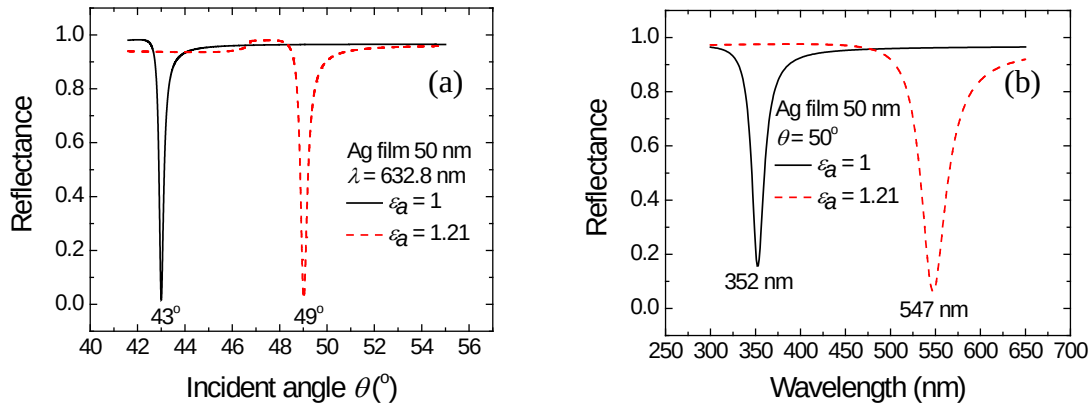

Figure 1.15 Typical SPR reflectance curves by (a) angular interrogation at a fixed wavelength (632.8 nm) and (b) wavelength interrogation at a fixed incident angle (50°).

Figure 1.15(a) shows typical SPR reflectance curves at a fixed wavelength 632.8 nm. The incident angle is scanned, and the SPR angle θ_{SPR} shifts from 43° to 49° when the dielectric constant of the surrounding medium ε_a is changed from 1 to 1.21. If the incident angle is fixed at 50°, the wavelength can be scanned, and the SPR wavelength λ_{SPR} shifts from 352 nm to 547 nm when the dielectric constant of the surrounding medium ε_a is changed from 1 to 1.21, as shown in Figure 1.15(b). Therefore, the binding events between the biomolecules on the metal surface

can be monitored by measuring the shift of θ_{SPR} or λ_{SPR}, which is the principle of the SPR based sensor.

SPR sensors have been widely used in the detection of proteins,[60, 61] DNA,[62-64] antibody[65] and toxins.[66-68] In the field of bacteria detection, SPR sensors have been applied for *E. coli* detection[69] and *Salmonella* detection. [26-28] Tremendous interest has been attracted on the sensitivity enhancement of SPR sensors. By optimizing the properties of the metal film and those of the prism, the light launching conditions, and the immobilization efficiency of the biocapturing elements on the sensor surface, efforts have been made by use of fibre optic sensor, [70-72] change of prism material, [73, 74] double layers such as gold-silver [71, 75] and Indium Tin Oxide (ITO)-silver, [76] and biochemical arrays. [65]

In recent years, localized surface plasmon (LSP), i.e. electrons collectively oscillating in the metal nanostructures, have drawn intensive attention for SPR signal amplification. [77-87] These LSPs allow strong optical coupling of incidence light into resonance and the momentum matching is usually achieved at higher momentum than bulk SPs modes. Based on this knowledge, modified SPR sensing systems, such as metallic nanoparticles conjugated with target analytes [80, 82] or used as local resonators, [87] two-dimensional nanohole array SPR sensor, [83] and metallic nanowires regularly patterned on a metal film, where LSPs inside the nanowires strongly interact with SPs inside the metal film, [77-79, 81, 84-86, 88] have been proposed theoretically and experimentally. These studies show that interactions between LSPs, SPs, and the analytes on the nanostructures can lead to various properties such as narrow SPR curve width or additional shift of resonance angle.

1.2.3 Localized Surface Plasmon Resonance based biosensor

We have discussed that the collective oscillation of the surface plasmon propagating along the interface between the metal and the dielectric has different response to the different dielectric. When the planar surface shrinks to a spherical surface within 100 nm, the collective oscillation of electrons will be confined in the sphere, and their response to different dielectric also can be used as a transducer for an optical sensor.

1.2.3.1 Localized surface plasmon resonance

As the size of a metal structure is within 100 nm, the movement of electrons through the internal metal framework becomes restricted. This confined plasmon is the localized surface plasmon. In the visible light range, the wavelength is larger than the size of the metal nanoparticle, the electron density in the particle can be polarized to one surface and oscillates in resonance with the light's frequency as the wave front of the light passes, as shown in Figure 1.16(a). This is called localized surface plasmon resonance. Because the frequency of the light matches with the collective oscillations of the confined electrons, the energy of the incident photons will be absorbed, corresponding to a peak in the absorbance spectrum (Figure 1.16(b)). The absorbance peak is called as the plasmon peak and the corresponding wavelength is called as the plasmon peak wavelength λ_p.

For a sufficiently small system, the electrons will sense the presence of the boundaries and modify their collective oscillation accordingly. As the shape or size of the nanoparticle changes, the surface geometry changes and causes a shift in the electric field density on the surface. Also, changing the dielectric constant of the surrounding material will have an effect on the oscillation frequency due to the varying ability of the surface to accommodate electron charge density from the nanoparticles. These will cause a change in the oscillation frequency of

the electrons, generating different cross-sections for the optical properties including absorption and scattering.

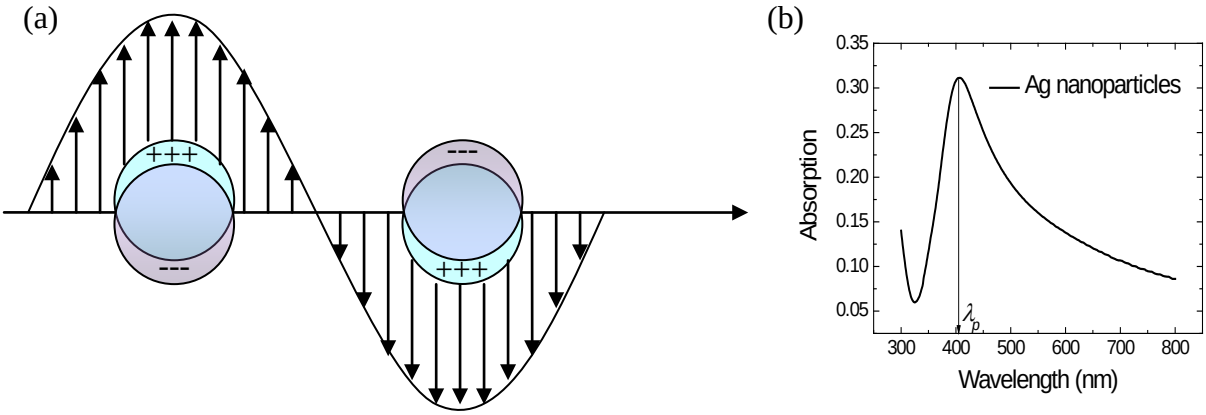

Figure 1.16 (a) Illustration of localized surface plasmon resonance. (b) A typical absorption spectrum of Ag nanoparticles.

1.2.3.2 Principle of localized surface plasmon resonance sensor

As described above, if the particle has a certain shape and size, the change of its absorption and scattering reflects the change of the surrounding medium. There have been solutions for the scattering and absorption properties of small particles in a beam of electromagnetic radiation. Mie originally calculated these properties by solving Maxwell's equations for small spheres interacting with an electromagnetic field. The derivation is outlined in the Appendix.[58] According to Mie's theory, for a metal sphere with a diameter *a*, its absorption efficiency is

$$Q_{abs} = \frac{24\pi a \varepsilon^{3/2}}{\lambda} \frac{\varepsilon_i}{(\varepsilon_r + 2\varepsilon)^2 + \varepsilon_i^2}, \tag{1.35}$$

$$\varepsilon_1 = \varepsilon_r + i\varepsilon_i, \tag{1.36}$$

where λ is the wavelength of the light, ε_1 and ε are dielectric functions inside and outside the sphere, respectively. One should note that, when the size of the metal sphere is in nanometer

scale, its dielectric function will be different from that of the bulk material and can be calculated by the following equations [89]:

$$\varepsilon_1 = \varepsilon_{bound-electrons} + \varepsilon_{free-electrons}, \tag{1.37}$$

$$\varepsilon_{bound-electrons} = Q_{bulk}\int_{\omega_g}^{\infty} \frac{\sqrt{x-\omega_g}}{x}[1-F(x,T)]\frac{(x^2-\omega^2+\gamma_b^2+i2\omega\gamma_b)}{(x^2-\omega^2+\gamma_b^2)^2+4\omega^2\gamma_b^2}dx, \tag{1.38}$$

$$F(x,T) = \frac{1}{e^{(\hbar x - E_F)/kT}+1}, \tag{1.39}$$

$$\varepsilon_{free-electrons} = 1 - \frac{\omega_p^2}{\omega^2 + i\gamma_{free}\omega}, \tag{1.40}$$

$$\gamma_{free} = \gamma_{bulk} + S\frac{v_F}{a}, \tag{1.41}$$

$$\omega = \frac{2\pi c}{\lambda}, \tag{1.42}$$

where Q_{bulk} is the coefficient for bound electron contribution, $E_g = \hbar\omega_g$ is the gap energy, E_F is the Fermi energy, γ_b is the damping constant for bound electrons, γ_{bulk} is the damping constant for free electrons, ω_p is the bulk plasmon frequency, S is the scattering constant and v_F is the electron velocity at the Fermi surface. The values of all the parameters can be found in Lucia B Scaffardi's work. [89]

The absorption Q_{abs} depends on the composition (ε_1), size (a), and shape (boundary conditions) of particles. More interesting, it will be influenced by the surrounding medium. When the surrounding medium around the Au NPs is changed (Figure 1.17 (a)), such as the analyte binding, the dielectric constant ε near Au surface is changed and therefore the plasmon peak wavelength λ_p will shift, as shown in Figure 1.17 (b). This is the basic principle of a LSPR sensor.

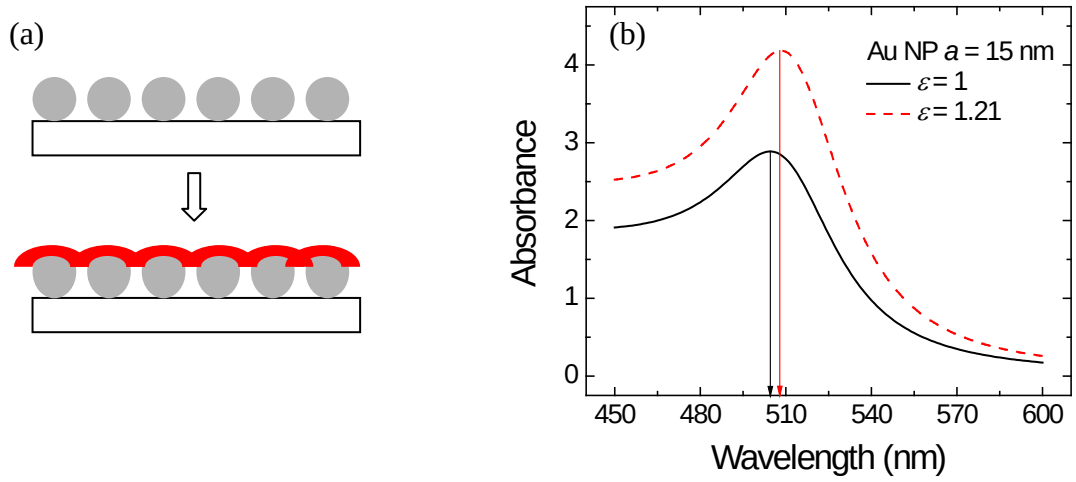

Figure 1.17 (a) Illustration of the change of surrounding dielectric around the Au NPs. (b) The shift of absorbance spectra of Au NPs from $\varepsilon = 1$ to $\varepsilon = 1.21$.

1.2.3.3 Overview of present localized surface plasmon resonance sensor

Recently, the LSPR property of the metal nanostructures has been intensively studied and broadly applied in various fields. Since the surrounding dielectric environment of the metal structure has a significant influence on the plasmon peak wavelength, the LSPR sensing process can be accomplished by observing the plasmon peak shift due to the binding of an analyte to the metal surface. With the advance in a simple optical setup, many kinds of sensors based on LSPR have been developed and applied in the detection of heavy metal ion,[90] toxin,[91] protein,[92] glucose,[93] nucleic acids,[94] biotin-strptavidin[95] and antigen-antibody[96, 97] reactions. Besides the sensor applications, LSPR properties of silver and gold nanoparticles have been used for surface enhanced vibrational spectroscopy, [98-101] and other important optical applications such as non-linear optics, photoluminescence and photonic devices. [102-105]

One of the important factors affecting these applications is the metal NPs fabrication. For sensor application, the uniform NPs substrate is able to produce a narrow width of the

absorbance spectrum and therefore enhance the sensitivity. For some other different applications, they may require different plasmon peak wavelength λ_p and absorbance peak properties. Thus, the ability to tune the LSPR property of silver or gold NPs has great significance in those technological applications. For example, the use of the tunable LSPR can increase the third-order nonlinear optical coefficient of the silver nanoparticles by a factor of 16. [106] By tuning the LSPR wavelength to be close to the excitation wavelength of the laser, the optimum substrate for surface plasmon-assisted enhanced spectroscopy has been demonstrated. [107]

Therefore, a great amount of effort has been devoted to the fabrication of tunable LSPR metallic nanostructures. For nanoparticle fabrication, reduction methods are widely accepted as practical and versatile approaches. [102, 108, 109] However, many of the applications require the nanoparticles to be supported on a substrate. Thus the nanoparticles produced by this traditional approach need to be immobilized onto a substrate uniformly. This immobilization step presents a great challenge for practical applications. To overcome this difficulty, many other fabrication methods that directly fabricate nanoparticles onto a substrate have been proposed. In particular, lithography methods such as nanosphere lithography (NSL) [110-112] and electron beam lithography (EBL) [113] provide an accurate way to control the size, shape and spacing of the surface-confined nanoarrays. Nevertheless, NSL is limited in terms of structures and topographies generated, whereas EBL is time-consuming, expensive, and not applicable in large-scale production. In addition, in order to achieve the goal of tuning the LSPR, one could also coat nanoparticles with transparent oxide to change the dielectric environment. [102, 109, 111, 114] Another economical and direct fabrication method to produce uniformly coated nanoparticle substrate is physical vapor depositions, such as thermal evaporation[115] and sputtering[116]. The dependence of localized surface plasmon resonance wavelength on the

deposition parameters substrate temperature, deposition rate, and film thickness for silver and gold films was explored quantitatively, though the optical properties of these films have not been discussed in detail. [115] As a result, a simple and low-cost method to produce the uniform and tunable metal NPs for the detection of molecular or bacteria interactions is desirable.

1.3 Dynamic shadowing growth

Dynamic shadowing growth (DSG) technique has evolved from the so-called oblique angle deposition (OAD) and glancing angle deposition (GLAD). OAD is a physical vapor deposition process where the collimated deposition flux is incident onto a substrate with a large angle θ (typically greater than 75°) with respect to the surface normal (Figure 1.18(a)).

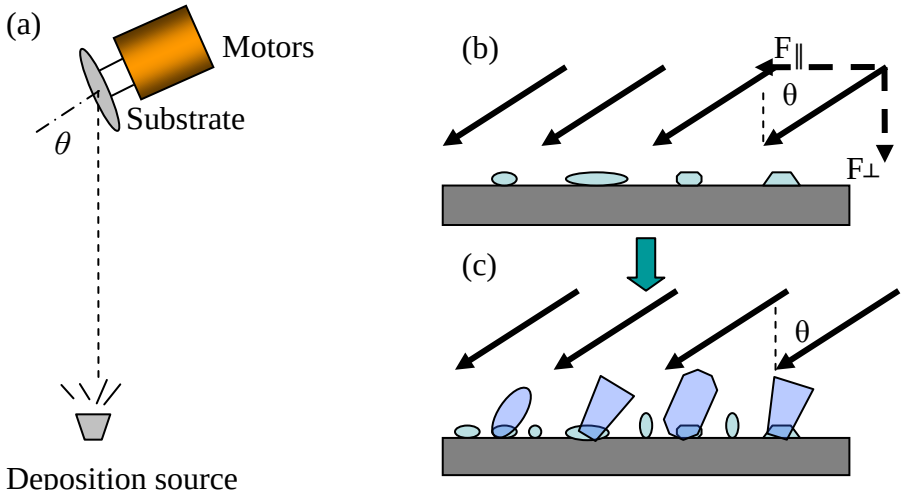

Figure 1.18 (a) A schematic of oblique angle deposition setup. (b) and (c) Shadowing effect.

Geometrical shadowing effect and surface diffusion are the dominant OAD mechanisms [5,6]. As shown in Figure 1.18(b), at the beginning of the deposition, there are random nuclei formed on the substrate. The adatom mobility characteristic of the material and deposition conditions will determine the size of the isolated nuclei: deposition with high adatom mobility

materials creates larger diameter nuclei than deposition with low adatom mobility materials. Since the deposition flux is not incident onto the substrate perpendicularly, the vapor flux can be decomposed into two components: a vertical component $F_{\perp}$, which is normal to the substrate, and a lateral component $F_{||}$, which is parallel to the substrate and contributes to the shadowing effect. The substrate will receive the vapor flux from both of the components. Clearly, due to the highly oblique angle, the vertical component is very small and the main growth source comes from the lateral component.

As deposition proceeds (Figure 1.18(c)), the taller islands will act as the shadowing centers and block the lateral component so as that the shorter ones will not receive more impinging atoms. Since the adatom mobility is too low for surface diffusion, the voids produced by shadowing effects cannot be filled. When the adatoms land on the top of the taller islands, they keep part of their momentum component parallel to the substrate and diffuse in the direction toward the substrate normal. Consequently, this competition process and the lack of significant surface or bulk diffusion will leave the taller islands grow into tilted nanocolumnars.

Figure 1.19 (a)-(b) show the scanning electron microscope (SEM) images of the top view and cross-sectional view of the tilted Si nanorods with 2000 nm normal film thickness in the normal direction deposited in a customer-designed e-beam evaporation system. During the deposition, the vapor incident angle was fixed at 86° and the deposition rate was monitored to be around 0.4 nm/s. In general, it is accepted that there is a fixed relationship between incident flux angle θ and column tilting angle α for a given set of deposition conditions, but it is complex and poorly understood. The empirical ‘‘tangent rule’’ $\tan\alpha = (1/2)\tan\theta$ [117] is a simple relationship based on near normal deposition but gives very poor results for θ greater than about 50°. A relationship by Tait *et al.*[118] based on geometrical analysis

$\alpha = \theta - \arcsin[(1-\cos\theta)/2]$ gives much better results for highly oblique angles. While these relationships give some qualitative predictions of column angle α, it is affected by the physical properties of the source material and the deposition parameter such as substrate and film temperature, angular distribution of the deposition flux, background gas pressure and composition, and flux energetics. The density of the nanocolumns decreases with the deposition angle and the materials with low bulk melting temperatures tend to produce more dense films.

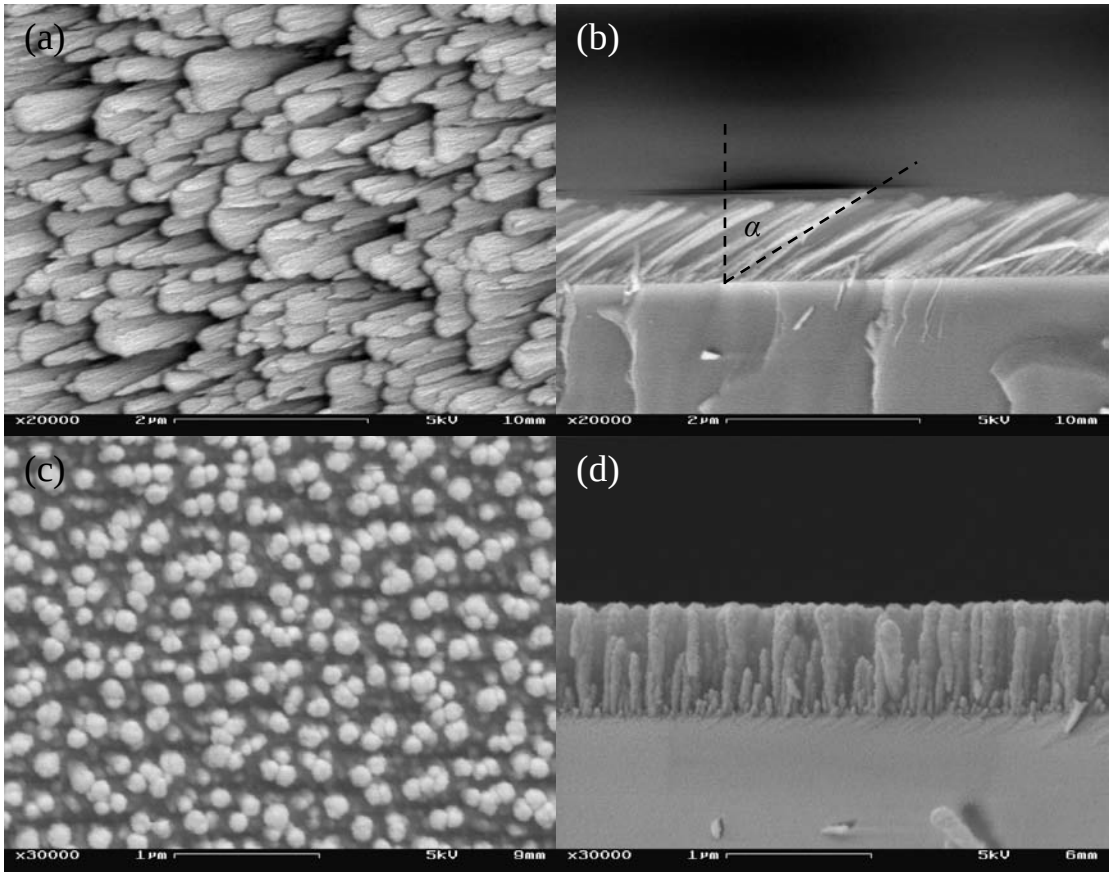

Figure 1.19 SEM images of (a)-(b) the tilted Si nanocolumns and (c)-(d) the straight Si nanocolumns.

Since the growth principle of OAD is closely related with the collimation of the incident evaporation flux, we will employ the electron beam evaporation and the thermal evaporation as the deposition techniques. To collimate the incident flux, a large distance of roughly 40 cm is

used. The general experimental conditions are the following: the experiments are performed in a high vacuum chamber with a background pressure of 1×10^{-6} Torr, and the nominal thickness is recorded by a quartz crystal microbalance which is perpendicular to the direction of the incident vapor.

Glancing angle deposition (GLAD) is the combination of OAD with substrate manipulation, and can be used as a novel approach to control the three dimensional film structures on the nanometer scale. By moving the substrate in a controlled way during the deposition, such as rotation azimuthally at a fixed incident angle, rotation back and forth by changing the incident angle, and rotation azimuthally and polarly simultaneously, the shape of the columns can be accurately tailored on a nanometer scale. The substrate will be manipulated by two stepper motors inside the vacuum chamber with custom computer software and electronics. One controls the incident angle θ and another is responsible for the azimuthal rotation of the substrate.

By fixing the incident angle and continuously rotating the substrate azimuthally with a suitable constant speed, the vertically aligned nanocolumns can be formed. During the rotation, the taller islands have an equal chance to receive the same amount of the lateral component F_{II} from all the directions. After a complete revolution, the total F_{II} is zero due to the cancellation of F_{II} at opposite directions, which means there is no preferred orientation of the nanocolumns. Eventually perpendicular and aligned columns with respect to the substrate surface are formed. Figure 1.19 (c)-(d) shows the SEM top view and cross section of the straight Si nanorods with 2000 nm normal film thickness in the normal direction. During the deposition, the vapor incident angle was fixed at 86°, the deposition rate was monitored to be around 0.4 nm/s and the substrate azimuthal rotation speed was 0.25 Hz. Other factors affecting the nanostructures are the

deposition rate, rotation speed and material specific parameters such as surface diffusion and crystal plane effects.

Through computer controlled substrate rotation, the nanocolumns can be engineered into a variety of unique shapes [119-123]. When the direction of arrival of the vapour flux is varied during deposition, the growth of individual columns will ‘‘follow’’ the position of the source and the desired nanostructure can be formed. By changing the incident angle, the nanocolumns with C shape and S shape, can be obtained [124]. With the change of only the azimuthal rotation of the substrate, zigzag shape, flower-like, helical columns and multilayer nanocolumns with different geometries can be achieved [121, 123]. By combining the change of the incident angle and the azimuthal rotation, sinusoidal modulated nanoculumns or honeycomb-like nanocolumns can be formed [125]. So far, most nanostructures fabricated by DSG were made of only one particular material, such as Si, Co, W, Ta, Cr, MgF_2, TiO_2, and SiO_2 [126-129]. The use of multiple materials within a single DSG nanostructure is also explored [130-133].

CHAPTER 2

AU/SI HETERO-NANOROD-BASED SENSOR FOR *SALMONELLA* DETECTION

2.1 Introduction

We have introduced the basic fluorescence based immunoassays in chapter 1. Obviously, the sensitivity depends on the number of the targets. If there are only few targets, methods need to be investigated to improve the fluorescence signal. In this chapter, we show that Au/Si "matchstick" nanorods used as a scaffold can be functionalized with anti-*Salmonella* antibodies and fluorescence dye (Alexa 488) to rapidly and sensitively detect *Salmonella*. We believe that this hetero-nanostructure not only can solve the difficulty that the recognition molecules and signaling molecules are immobilized onto single component nanostructures simultaneously, but also the Si nanorods with high surface-to-volume ratio can accommodate thousands of fluorescence molecules, and therefore improve the detection sensitivity.

2.2 Experimental Methods

Silicon wafers (Montco Silicon Technologies, INC.) were used as a substrate for the silicon (Si) nanorods growth. Gold (Au) target for SPI-MODULE™ Sputter Coater was purchased from SPI supplies (Structure Probe, Inc.). Fluorescent dye, Alexa Fluor® 488 carboxylic acid succinimidyl ester was purchased from Invitrogen (Carlsbad, California).

Unlabeled anti-*Salmonella* and killed *Salmonella* (*Salmonella typhimurium* strain) were obtained from Kirkegaard & Perry Laboratories, Inc. (KPL, Gaithersburg, Maryland). 3-Aminopropyltriethoxysilane (APTES) and Dithiobis-succinimidyl propionate (DSP) were from Sigma-Aldrich (St. Louis, MO) and Pierce Chemical (Rockford, IL), respectively.

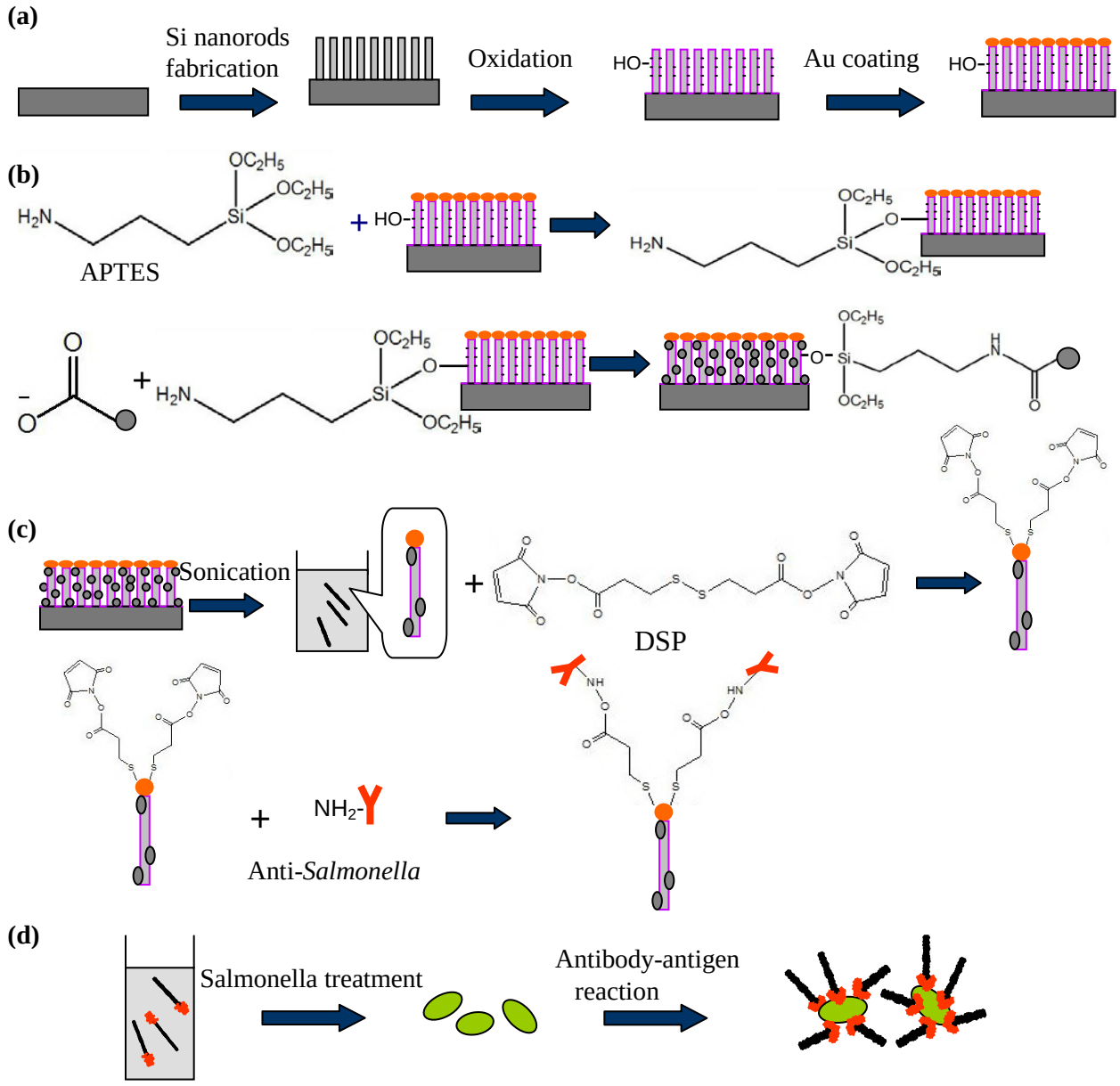

Figure 2.1 Process flow for the *Salmonella* detection by bio-functionalized Au/Si nanorods. (a) Au/Si nanorods fabrication; (b) Dye immobilization onto Si nanorod; (c) Antibody conjugation onto Au tip; (d) *Salmonella* detection via the antibody-antigen reaction.

Au/Si hetero-structured nanorod-based *Salmonella* detection is facilitated by the enhanced fluorescence signal elicited during the binding of *Salmonella* to the anti-*Salmonella* antibodies conjugated to the nanorods. The method is illustrated in Figure 2.1. The vertically-aligned Si nanorods are fabricated on the Si substrate and the subsequent oxidation process provides the hydroxyl groups on the nanorod surfaces. Then, a thin layer of Au is sputter-coated onto the nanorods (Figure 2.1(a)). Using APTES, the silica surface is silanized with amine groups, which form the peptide bond with the amine-reactive carboxylic groups in the Alexa 488-succinimide dye (Figure 2.1(b)). To immobilize antibodies onto the nanorods, a DSP crosslinker will chemisorb to the Au surface by breaking the disulfide bond and conjugation of anti-*Salmonella* antibody to Au is achieved by releasing of the N-hydroxysuccinimide leaving groups via the primary amines (Figure 2.1(c)). For detection, *Salmonella* can be fixed, reacted with the functionalized hetero-structured nanorods, and detected through signaling mediated by multiple Alexa 488 dye molecules bound on the Si nanorods, generate an intense fluorescence signals providing detection of the bound *Salmonella* (Figure 2.1(d)).

In this chapter, Si nanorods with a nominal thickness of 2000 nm were fabricated by GLAD method. During the deposition, the incident angle was fixed at 86°; the deposition rate was 0.4nm/s and the azimuthal substrate rotation speed is 0.05-0.25 Hz.

To oxidize the Si surface, Si nanorods were treated by SPI Plasma-Prep™ II Plasma Etcher (SPI supplies) with pure oxygen for 10 minutes. Following this, a thin layer of Au was sputtered onto the top of the Si nanorods by SPI-MODULE™ Sputter Coater system (SPI supplies). In this Coater chamber, the substrate of the Si nanorods was placed facing down to the Au target at a distance of 4 cm. The Au thickness was approximately monitored by the coating time.

After Au coating, 2% APTES in acetone, the coupling agent, was annealed to the hydroxyl groups on the oxidized Si nanorods (45 overnight). The excess reagent was separated from the Si nanorods by washing three times with acetone. Alexa488-succinimide ester was applied to the APTES/Si nanorods at room temperature for 1 hour and then transferred to 4°C overnight. The dye ester attached to the Si nanorods via the primary amine supplied by the APTES and excess dye was washed off by DI water. The Alexa488 dye immobilized on the Au-coated Si nanorods (DNRs, Au/Si nanorod/Alexa488) were air dried and dispersed in acetone using BRANSON MODEL 2510 ultrasonic cleaner (Kell-Strom, Wethersfield, CT). The sonication time was 1-2 hours. After sonication, the original substrate had a shining silicon surface looking. Approximately 80-90% nanorods came off from the surface and dispersed in the acetone uniformly by estimating the shining surface area of Si substrate before and after sonication.

The DNRs were centrifuged (Centronix microcentrifuge, National Labnet Co.) to the bottom of the glass vial. Then the supernatant was removed, and the DNRs were air dried. A 5 mg/ml solution of DSP in acetone was added to the DNRs and incubated for 30 minutes at room temperature. The DNRs/acetone suspension was centrifuged and the supernatant removed. Fresh acetone was added, and the DNRs were re-suspended by vortexing. By repeating this process, the DNRs were washed using acetone at least three times. Following the last wash, 100 μg/ml anti-*Salmonella* in Phosphate Buffered Saline buffer (FA Buffer, pH 7.2, for use with fluorescent antibody reagents, BD, Franklin Lakes, NJ) was added to the dried DNRs, and the DNRs were re-suspended in FA buffer by sonication. After 2 hours incubation at room temperature, the DNRs were transferred to the refrigerator for overnight. The anti-*Salmonella*-DNRs were then washed with FA buffer by centrifuge for several times to remove unbound anti-Salmonella

antibody. The final concentration of the anti-*Salmonella*-DNRs suspension was estimated to be ~ 3.6×10^9 nanorods/ml.

The microscope slides (Gold Seal, Portsmouth, NH) were cleaned using Piranah solution (one part Hydrogen Peroxide and four part Sulfuric acid) and rinsed with DI water. The slides were dried in nitrogen and prepared for use. A 2 μl suspension of 10^9 cfu/ml *Salmonella* bacterial (2×10^6 bacteria in total) was loaded onto the cleaned microscope slide and allowed to air dry. To fix the Salmonella antigen, the slide was placed in 95% ethanol for 1 min, removed, and allowed to air dry.

The DNR suspension was used as the negative control. In this case, both the anti-*Salmonella*-DNR suspension and the DNR suspension (50 μl) were applied onto the fixed bacteria for two hours under room temperature. The slides were maintained in a humidified atmosphere to avoid the suspensions from drying out during the incubation. After the incubation, the slides were washed by 0.05% Tween/FA buffer three times and once with DI water.

2.3 Results and Discussion

2.3.1 Au/Si nanorods fabrication

The SEM images (Figure 1.19(c)-(d)) show the top-view and cross-section images of the Si nanorods deposited as a 2000 nm normal film thickness on the substrate. The nanorods have a needle shape, and by estimation, the top diameter, the bottom diameter, and the length of the nanorod were 150 nm, 60 nm and 900 nm, respectively. The density of Si nanorods was estimated to be 20 μm^{-2}. The high aspect ratio of the nanorods can accommodate more dye

molecules than the flat surface. By assuming that the Si nanorod takes a cylindrical shape, we calculate the surface area ratio of the nanorod surface to the flat surface is 9.48.

A gold layer with a thickness of 5 nm was sputtered on the Si nanorods. As shown in the transmission electron microscopy (TEM) image (Figure 2.2(a)), the black areas are indicative of gold coating on the Si nanorods. Most of the gold was distributed on the top of the Si nanorod, however some gold clusters were deposited on the side wall of the Si nanorod, giving the appearance of a "match stick". Using TEM, the gold particle size was estimated as 1 to 3 nm. Since the sputtering method used is based on argon plasma, and the directionality of the incident vapor has a wide angular distribution, the side wall Au deposition is expected. If the electron beam or thermal evaporation is used for Au deposition, the side wall coating will be much less.

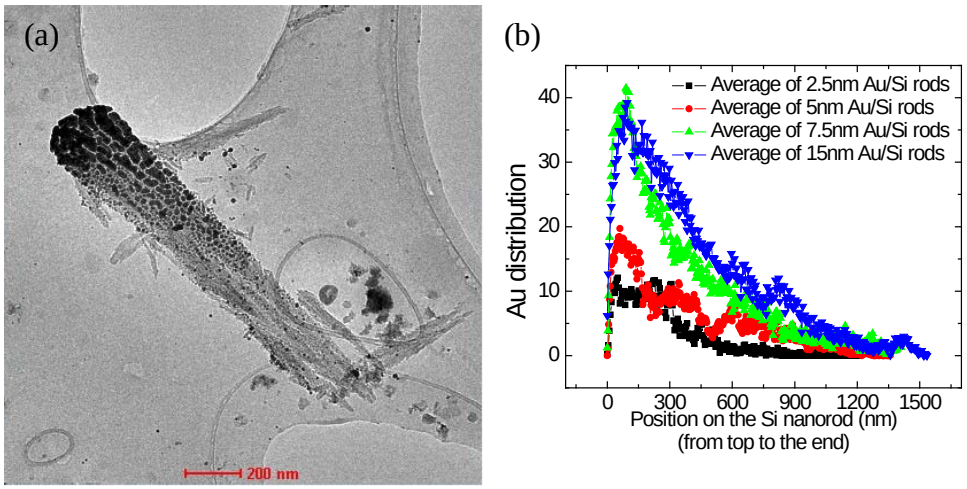

Figure 2.2 (a) Typical TEM image of Au/Si nanorod. (b) Au distribution on the Si nanorods with different thickness of Au sputtering.

An analysis of Au distribution on the Si nanorods with different thickness of Au sputtering was performed. A number of TEM images were taken and each image was processed by Image Tool which will only keep the black part and turn other part as white color. By means of Matlab 6.5, each pixel with black color will be counted as 1 and otherwise 0. As shown in

Figure 2.2(b), 7.5 nm and 15 nm Au coating will cover almost the entire surface of the Si nanorods, while 2.5 nm and 5 nm Au coating can leave bare Si surface for fluorescence dye molecules.

2.3.2 Fluorescence dye molecules immobilization

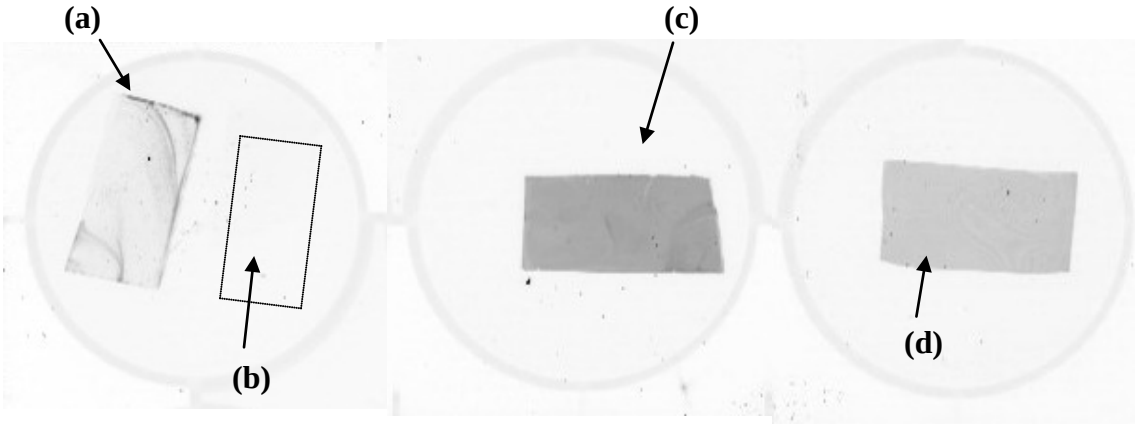

Figure 2.3 Fluorescence scans for Alexa 488 dye immobilization on silicon surface (532nm excitation / 526nm short pass emission filter). (a) Si film/Alexa 488; (b) Si nanorods; (c) Si nanorods/Alexa 488; (d) Au/Si nanorods/Alexa 488.

To examine the dye Alexa 488 immobilization on Si surface, four pieces were scanned by a fluorescence scanner (Typhoon Imager, Amersham): Si film/Alexa 488, Si nanorods, Si nanorods/Alexa 488 and Au/Si nanorods/Alexa 488, as shown in Figure 2.3. The fluorescence intensity ratio of the Si nanorods to that of the flat Si film is 9.45, which is consistent with the surface area ratio of these two surfaces, 9.48, estimated from the SEM images. After Au coating, the fluorescence intensity ratio of the nanorods to that of the flat Si surface reduces to 3.80, this is because the Au has covered part of the Si nanorods. If Au deposition can be improved by electron beam or thermal evaporation, there will be more space for dye molecules.

Besides Alexa 488, other fluorescence dyes also can be immobilized onto Si nanorods such as fluorescein-5-isothiocyanate (FITC). The procedure is as follows: 19.2 mg EDC and 11.2 mg Sulfo/NHS was dissolved in 400 μl DI water and then mixed with 8 mg FITC which has been dissolved in 100 μl DMSO. The mixture was magnetically stirred for 30 minutes and dropped onto APTES-treated Au/Si nanorods (250 μl for the entire surface). The chip was left under room temperature for one hour and then transferred at 4°C overnight.

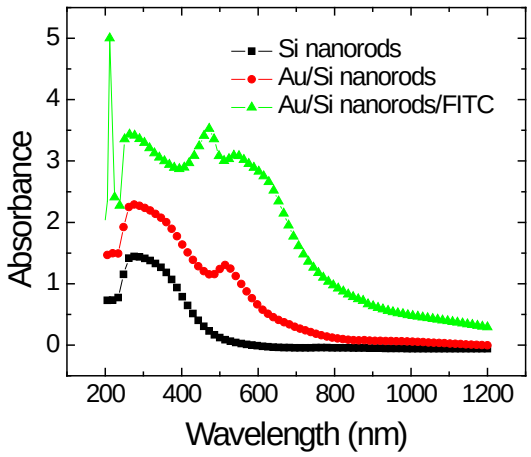

Figure 2.4 UV-Vis spectrum of Si nanorods (square) and Au/Si nanorods before and after the fluorescein-5-isothiocyanate (FITC) dye immobilization (dot and triangle).

After rinsed by DI water and dried by nitrogen, the Au/Si nanorods/FITC was measured with the absorption spectrum and shown in Figure 2.4. Also, a piece of Si nanorods and a piece of Au/Si nanorods were measured under the same conditions. The peaks around 280 nm, 520 nm and 480 nm are corresponding to Si, Au and FITC, respectively. The absorption spectra indicate the gold has been coated to the Si nanorods and the dye has been conjugated to the silica surface of the nanorods successfully.

In the process of dye immobilization, the Alexa 488-succinimide dye bound the amine group provided by APTES on the Si nanorods. To evaluate the effect of the immobilization, a 10

μl drop of Au-Si nanorods-Alexa488 suspension was sandwiched between the microscope slide and a cover slide and observed on fluorescence microscope (Olympus BX60). The fluorescent image of the DNR was observed under the 488 nm excitation and 100× objective as shown in Figure 2.5(a). The results show strong green fluorescence emitted from the nanorods demonstrating that the Alexa488 was successfully immobilized onto the Si nanorods.

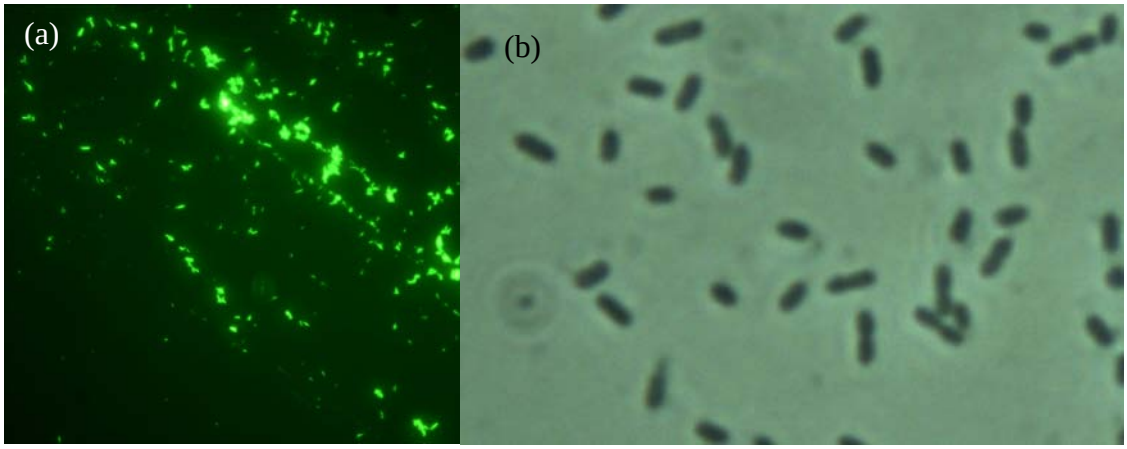

Figure 2.5 (a) Fluorescence image of Au/Si nanorods/Alexa488 (DNRs). (b) *Salmonella* observed under the optical microscope.

2.3.3 *Salmonella* detection by anti-*Salmonella*-DNR

To evaluate the efficacy of the hetero-nanostructured biosensor for detection of *Salmonella*, a 2 μl suspension of 10^9cfu/ml *Salmonella* bacterial (2×10^6 bacteria in total) was fixed onto the detection slides, incubated with the anti-*Salmonella*-DNR suspension and the DNR suspension, and washed as described in the Methods. Before the incubation, the *Salmonella* were observed by microscopy (Figure 2.5(b)) and they appeared as grey, thick elongated particles. After the washes, the slides were transferred to the fluorescence microscope. Figure 2.6 showed the fluorescence images taken from anti-*Salmonella*-DNR treated slide and control DNR treated slide. The anti-*Salmonella*-DNR treated slide exhibited strong fluorescent signaling compared to the control DNR treated slide (Figure 2.6), although some autofluorescence was

observable in the control. This may be due to non-specific interaction of the *Salmonella* specimen with the gold surface.

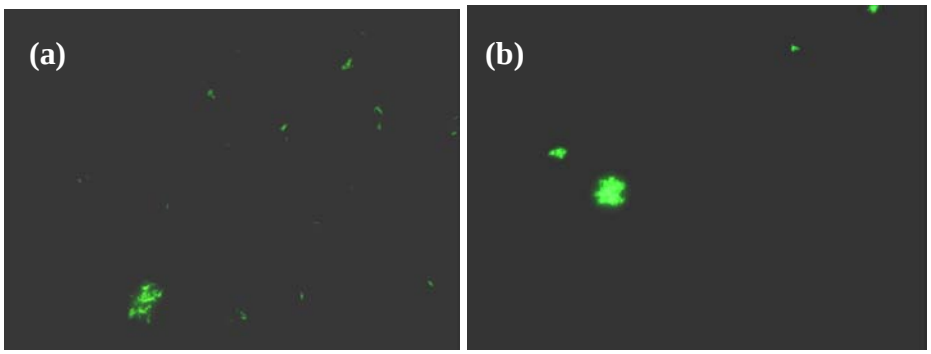

Figure 2.6 Fluorescence images of (a) anti-*Salmonella*-DNR and (b) DNR treated *Salmonella* detection slides.

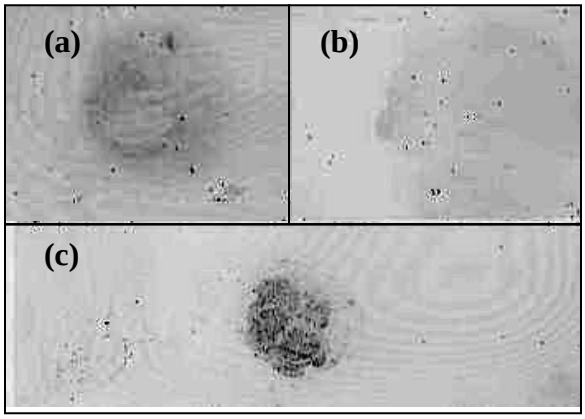

Figure 2.7 Fluorescence scans for *Salmonella* slides by Typhoon scanner. (a) 50 µl anti-*Salmonella*-DNR with 2% BSA treated slide; (b) 50 µl DNR with 2% BSA treated slide; (c) 50 µl DNR (no BSA treatment) treated slide.

To block non-specific reactivity on the gold surface, bovine serum albumin (BSA) solution was added in both the anti-*Salmonella*-DNR suspension and the DNR suspension. A 2% BSA blocking step effectively reduced or eliminated most of the non-specific binding. Using this blocking procedure, the anti-*Salmonella*-DNR treated slide yielded strong visible detection while the DNR treated slide showed almost no detectable signal (Figure 2.7(a)-(b)). As a comparison,

non-BSA treated DNR suspension was also applied to a *Salmonella* slide, and its fluorescence scanned image is shown in Figure 2.7(c).

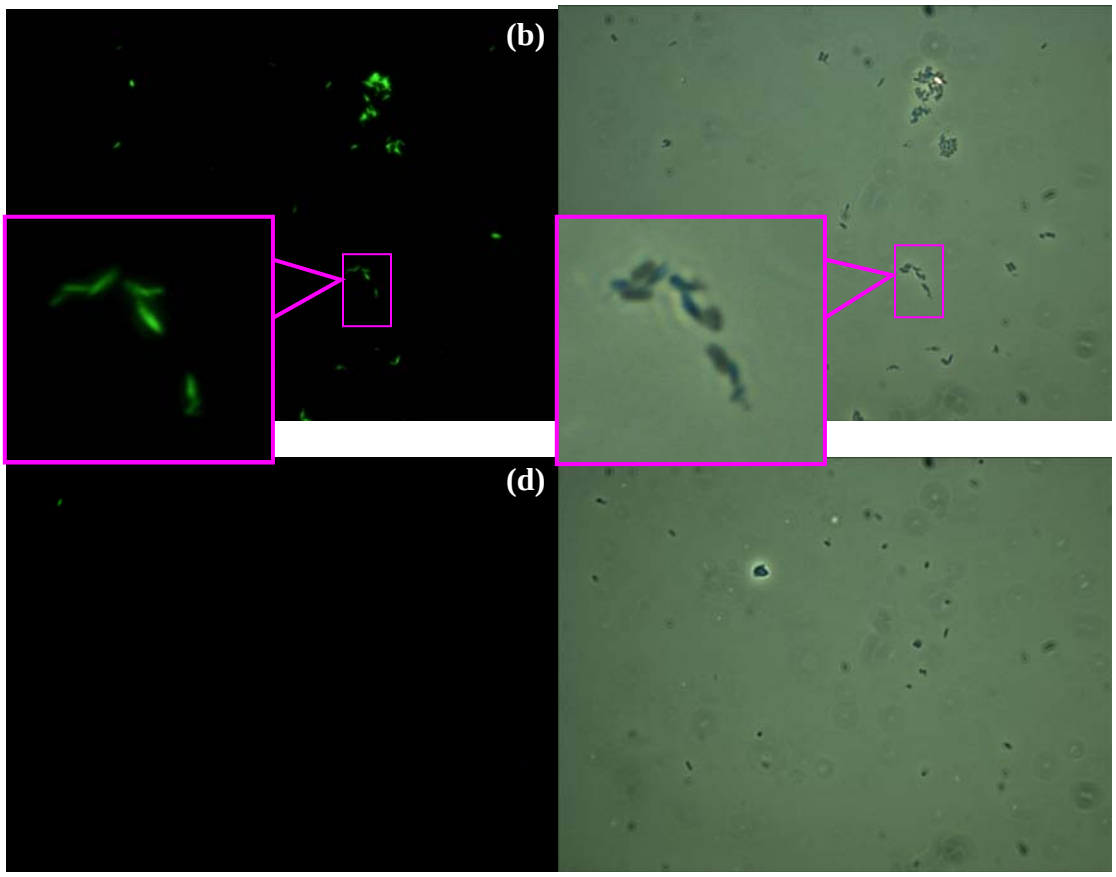

Figure 2.8 Images for Salmonella detection. (a) 50 μl anti-*Salmonella*-DNR with 2% BSA treated slide under the fluorescence excitation (488 nm excitation); (b) 50 μl anti-*Salmonella*-DNR with 2% BSA treated slide under the white light; (c) 50 μl DNR with 2% BSA treated slide under the fluorescence excitation (488 nm excitation); (d) 50 μl DNR with 2% BSA treated slide under the white light. The inserts in Figure 2.8(a) and Figure 2.8(b) are the blow-up of the corresponding locations in the two images.

The slides, as shown in Figures 2.7(a) and 2.7(b), were also evaluated by fluorescence microscope under an excitation laser with a wavelength of 488 nm and under the white light sequentially for the same location. Figures 2.8(a) and (b) show the anti-*Salmonella*-DNR treated *Salmonella* slide under laser excitation and white light, respectively. As shown in Figure 2.8(a), intense green spots indicating positive identification were observed on the sample that

corresponds to anti-*Salmonella*-DNRs. At the same location, under white light, there are also particles and aggregates observed in the image (Figure 2.8(b)). Comparing Figure 2.8(a) to Figure 2.8(b), there appears to be mostly a one-to-one correspondence between the particles or aggregates. To further illustrate this relationship, areas of the image in Figures 2.8(a) and (b) have been enlarged and presented in the inserts. The insert in Figure 2.8(a) shows 6-7 fluorescent particles with different orientations, while the corresponding insert in Figure 2.8(b) shows 11-12 particles. However, the particles have two different appearances, i.e grey, thick elongated particle and blue, thin longer particles. From the location and orientation of the particles (Figure 2.8(a)), it may be concluded that these blue longer particles correspond to the fluorescence particles, i.e., they are anti-*Salmonella*-DNRs, while the grey, thicker particles are *Salmonella* bacteria, similar to those shown in Figure 2.5(b). From the relative locations of the anti-*Salmonella*-DNRs and the *Salmonella* bacteria, one may conclude that each *Salmonella* bacterium binds with one anti-*Salmonella*-DNR. Although only one hetero-structured nanorod appears to capture one Salmonella bacterium, the fluorescence signal generated from the DNRs is strong enough for us to obtain single bacterium detection. It may be possible to increase the nanorod concentration in future studies in order to potentially improve the detection signal, i.e., one cell capturing two or more nanorods. For the negative control, we only found very few fluorescent spots as shown in Figure 2.8(c), demonstrates the specificity of this novel biosensor.

Though the detection limit and the specificity are under investigation, the results still show that multifunctional hetero-nanorods have promising potential for Salmonella detection. The Au/Si hetero-nanostructure based biosensor has several advantages in biological detection, particularly the potential sensitivity to detect a single bacterium. It may be possible to further

enhance detection, by improving Au layering on the nanorods, possibly by using a thermal or electron beam evaporation method.

2.3.4 *Respiratory Syncytial Virus* (RSV) infected cells detection by anti-RSV-DNR

Another beauty of this method is that, by varying the fluorescence dyes and antibodies, this biosensor technique can be used as a platform technique to detect other pathogens, or a mixture of pathogens. For example, by changing the anti-*Salmonella* antibody to the *Respiratory Syncytial Virus* (RSV) antibody, this nanorod based biosensor has also been successfully used to detect RSV infected cells.

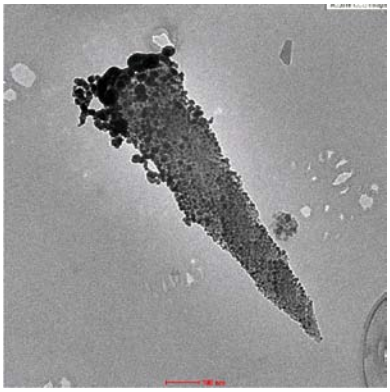

Figure 2.9 TEM image of RSV antibody (131-2A)/Au/Si nanorods/FITC.

The RSV antibody (131-2A) was conjugated to Au/Si nanorod/Alexa 488 nanostructures before they were sonicated into 3 ml PBS buffer. During the sonication, ice was added in the tray to keep the temperature low. A TEM image of the anti-RSV-DNR was taken and shown in Figure 2.9. The image shows after the dye immobilization and antibody conjugation, the nanostructure will not be changed.

Then both the ½ diluted and ¼ diluted nanorod suspensions were added to the RSV infected cells and uninfected cells. The uninfected cells were used as the control. After the

incubation and further rinses, the cells were scanned by the Typhoon fluorescence Scanner (532 nm excitation / 526 nm short pass emission filter), and the results are given in Figure 2.10. The uninfected cells do not show any significant fluorescence signals while the infected cells show different fluorescence intensities for different diluted nanorod suspensions. This result indicates that the fluorescence signal was detected as the RSV antibodies were specifically bound by the RSV antigen. All the results shown here demonstrate a novel means to sensitively detect the important pathogens.

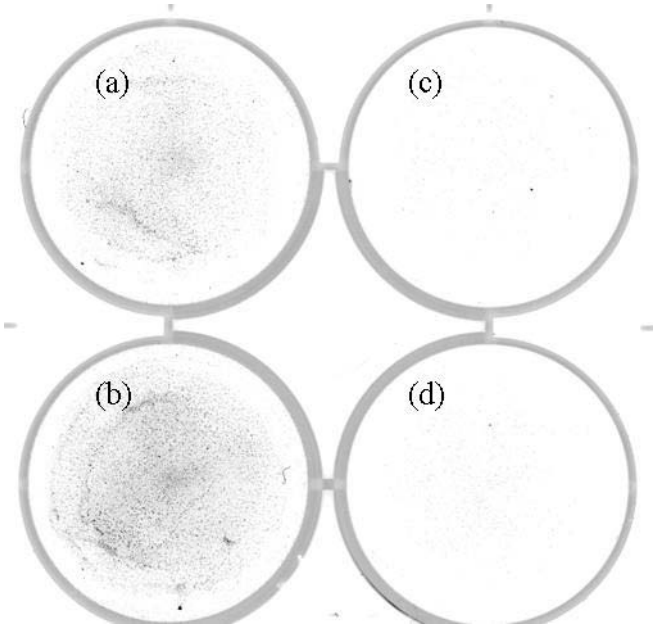

Figure 2.10 *Respiratory syncytial virus* (RSV) infected cells detection by Au/Si hetero-nanorod-based biosensor. (a) ¼ bio-functional nanorods dilution was applied to the RSV infected cells; (b) ½ bio-functional nanorods dilution was applied to the RSV infected cells; (c) ¼ bio-functional nanorods dilution was applied to the uninfected cells; (d) ½ bio-functional nanorods dilution was applied to the uninfected cells.

2.4 Conclusions

A novel Au/Si heterostuctutred nanorod-based detection method for *Salmonella* has been developed. Single bacterium was captured by the antibodies conjugated on the Au and detected by the thousands of dye molecules immobilized on the Si nanorods. This fluorescence-based detection method provides a platform technology that may be applied to detection strategies for

other pathogens as in principle, the antibody used for capture can be substituted as required. For example, we have changed the anti-*Salmonella* antibody to RSV antibodies, and have successfully detected the RSV infected cells. Additionally, the fluorescent detection dye can also be replaced by other types of dyes or potentially quantum dots that may allow for multiplex detection. In principle, other nano-building blocks such as the spherical silica nanoparticles or the commercially available fluorescent silica nanoparticles, after partially coated with Au, can also be used as the same detection biomarkers, though other techniques will be needed to deal with the Au coating and the antibody conjugation. In addition, this hetero-nanostructure based detecting method could expand the applications in many related fields such as pathogen detection, drug delivery and bio-engineering.

CHAPTER 3

LOCALIZED SURFACE PLASMON RESONANCE SENSOR BASED ON NANOPARTICLES FABRICATED BY DYNAMIC SHADOWING GROWTH

3.1 Introduction

In previous chapter, we have successfully demonstrated that the Au/Si nanorods based biosensor can be used to detect *Salmonella* by the enhanced fluorescence. However, the experimental process is a little complicated. Noble metal NPs, especially silver and gold, have attracted considerable interest due to their significant LSPR property and simple operation for sensor applications. To produce the uniform and tunable metal NPs for the detection of molecular or bacteria interactions, a simple and low cost fabrication method is desirable. By simply changing the thickness, deposition angle and rotation, DSG method can produce Ag or Au NPs with tunable LSPR property. Using the high affinity of avidin for *biotin*, Ag NPs based LSPR sensor showed promising capability of sensor development. To our knowledge, there has no report for the LSPR sensor for the whole bacteria detection. Therefore, Au NPs, which are more stable in aqueous solutions than Ag NPs, based LSPR sensor for *Salmonella* detection was investigated.

3.2 Localized surface plasmon resonance property of Ag nanoparticles fabricated by dynamic shadowing growth

In this section, the process of Ag NPs fabrication by OAD was introduced and the tunable LSPR properties of these Ag NPs were discussed.

3.2.1 Experiments

The thin silver NPs films were fabricated by the OAD method using a custom-designed electron-beam evaporation system (Torr International, Inc.). In order to perform a systematic study, five wedges with preset angles of θ = 45°, 70°, 75°, 80° and 85°, respectively, were all mounted onto a 3" diameter substrate holder, and a substrate was directly mounted to the same substrate holder to achieve θ = 0° deposition. The deposition for different incident angles was carried out simultaneously. To investigate how the optical property of Ag film changes as a function of film thickness d and deposition angle θ, we have prepared eleven depositions with the following QCM thickness reading: d = 5 nm, 10 nm, 15 nm, 20 nm, 25 nm, 30 nm, 35 nm, 50 nm, 65 nm, 80 nm and 100 nm, respectively. Note that, the actual film thickness of Ag films for the same d at different deposition angles would be different due to the geometric shadowing effect.

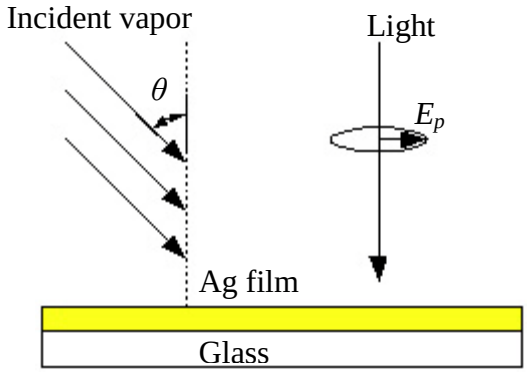

Figure 3.1 (a) A schematic of oblique angle deposition setup. (b) Sketch of polarized UV-Vis measurements.

Prior to deposition, all the glass slide substrates (Gold Seal® Catalog No. 3010) were cleaned using piranha solution (H_2SO_4:H_2O_2=4:1). The deposition rate is 0.7 ± 0.2 Å/s. The source material for evaporation was Ag pellets (99.999%, Alfa Aesar).

The optical properties of the Ag films were measured by an UV-vis-NIR double beam spectrophotometer (JASCO V-570). The light source was not polarized. In order to obtain the polarized UV-vis absorption spectra, the spectrophotometer was modified by placing two rotatable Glan Thompson polarizers (Thorlabs Inc.) in the paths of the sample and reference beams. During UV-Vis measurements, the incident light was perpendicular to the Ag film surface. The incident plane is determined by the normal direction of the Ag film surface and the direction of the incident vapor as shown in Figure 3.1. If the vibration direction of the electric field lies in the incident plane, we define the incident light as the *p*-polarized light.

The morphologies of the Ag films were characterized by an atomic force microscope (Veeco Dimension 3100) using the tapping mode. The scan rate was 1-2 Hz and the scan size was 1 μm×1 μm.

3.2.2 Particle size and roughness of Ag nanoparticles film

The typical AFM images for the Ag films with thickness d = 10 nm, 15 nm, 25 nm, 35 nm, 50 nm at deposition angles of θ = 0°, 70°, 80°, 85°, respectively, are shown in Figure 3.2. The images are all 1.0 μm×1.0 μm in dimension and arranged in the order of increasing d (row) and θ (column). The different contrast may come from the different scale used in the images. From visual inspection, a clear correlation between the particle size (diameter) D and θ or d is evident in the images. At θ = 0° and d < 25 nm, the Ag film is composed of small and uniform nanoparticles. As d increases, the particle size increases and the size distribution becomes more

random. When $d \geq 25$ nm, the surface morphology loses regularity. At $\theta \geq 70°$, the Ag nanoparticles grow slowly with thickness and the AFM images show regular surface features.

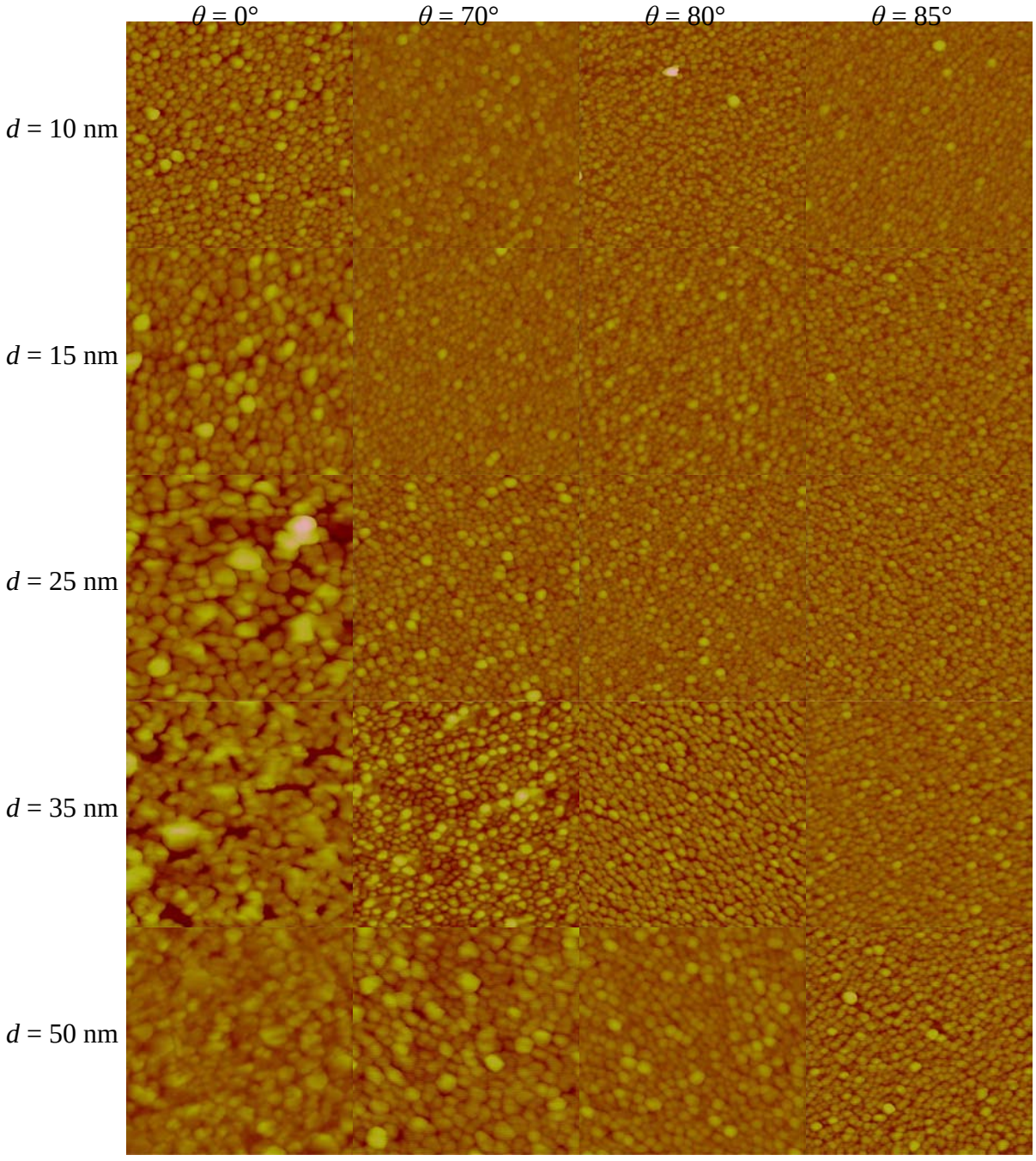

Figure 3.2 AFM images of representative Ag films on the glass substrates for different film thickness d and deposition angle θ.

Figure 3.3(a) plots the average particle size (diameter) D as a function of nominal film thickness d for $\theta = 0^o$, 70^o, 80^o and 85^o, respectively. The error bar was plotted and it became larger when the thickness increases to 50nm. The general trend is that the particle size increases with the increasing film thickness and the average particle growth rate r for $\theta = 0^o$, 70^o, 80^o and 85^o is 2.1, 0.65, 0.58 and 0.18 (unit: nm in particle size per nm in film thickness), respectively. It decreases monotonically with the increasing deposition angle. We found r drops from 2.1 to 0.2 - 0.6 when the deposition angle increases from $\theta = 0^o$ to $\theta \geq 70°$. In addition, we obtained the root-mean-square (RMS) roughness w, which describes the fluctuations of the surface heights around an average surface height, as a function of the thickness d. As shown in Figure 3.3(b), at $\theta = 0°$, the RMS roughness w increases first ($d \leq 25$nm) and then begins to decrease. This may be caused by the coalescence between the particles, which can produce broadly distributed particles on the surface and result in a small RMS roughness. For $\theta \geq 70°$, the RMS roughness w increases with the increasing film thickness monotonically.

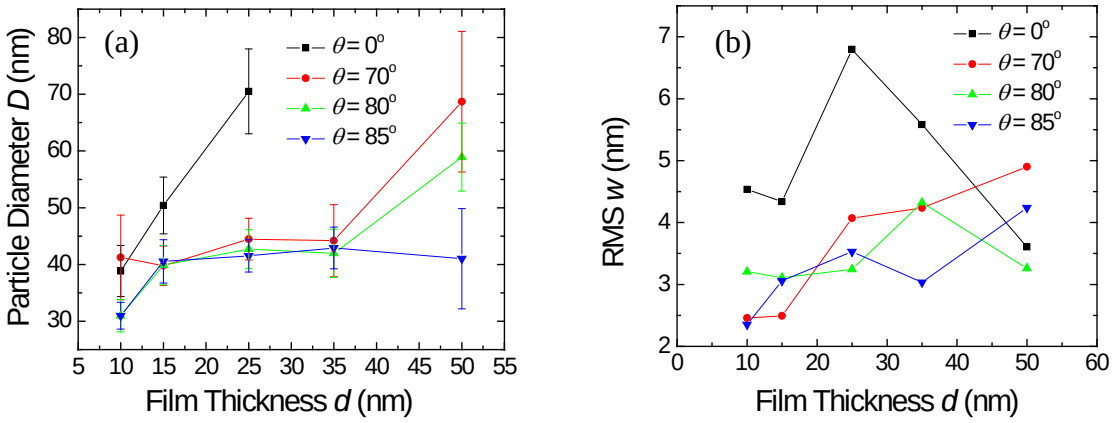

Figure 3.3 (a) The relationship between the particle diameter D and the film thickness d. (b) The relationship between the RMS roughness and the film thickness d for different deposition angle θ.

3.2.3 Power spectra of Ag nanoparticles film

For LSPR spectra, the particle size and the size distribution are critical. From the AFM images, we could not obtain the accurate distribution of particle sizes due to the difficulty to determine a threshold, but visually one could see that if there are more uniform particles on the surface (such as d = 25 nm, θ = 85° in Fig. 3.2), the surface morphology looks more regular. The regularity of surface feature can be characterized by power spectrum. Figures 3.4(a) and 3.4(b) shows two characteristic 2D power spectra of d = 35 nm, θ = 0°, and d = 35 nm, θ = 85° samples. From the AFM images, the d = 35 nm, θ = 0° sample has a broad distribution of particle sizes, and there is no surface regularity. The power spectrum shows a diffuse pattern symmetrically around the origin. For the d = 35 nm, θ = 85° sample, there are recognized periodicity, and the power spectrum shows a diffused ring structure, as shown in Figure 3.4(b). The power spectrum also shows a slightly anisotropic pattern. The location of the ring, k_c, reflects the spatial period, or the wavelength of the structure.

To determine k_c, a circular average power spectrum, which will include information from all the directions, can be obtained and fitted with a Gaussian function. If there is a ring structure, the circularly averaging will give a one-dimensional power spectrum with the peak position located at the center of the ring. Figures 3.4(c) and 3.4(d) show two pairs of characteristic circular averaged power spectra ($P(k)$) for d = 10 nm and 35 nm at θ = 0° and 85°, respectively. These spectra have been smoothened by five point adjacent average. The characteristic spatial frequency k_c, corresponding to the maximum intensity of the power spectrum, is inversely proportional to the averaged wavelength of the periodic morphology of the Ag nanoparticle surface, or the characteristic length ζ, the average distance between the centers of two adjacent Ag nanoparticles, which is defined as $\zeta = \frac{2\pi}{k_c}$. As long as the power spectrum shows a distinct k_c,

the particles are distributed uniformly, while if there is no k_c or $k_c \rightarrow 0$, the particles have a random distribution.

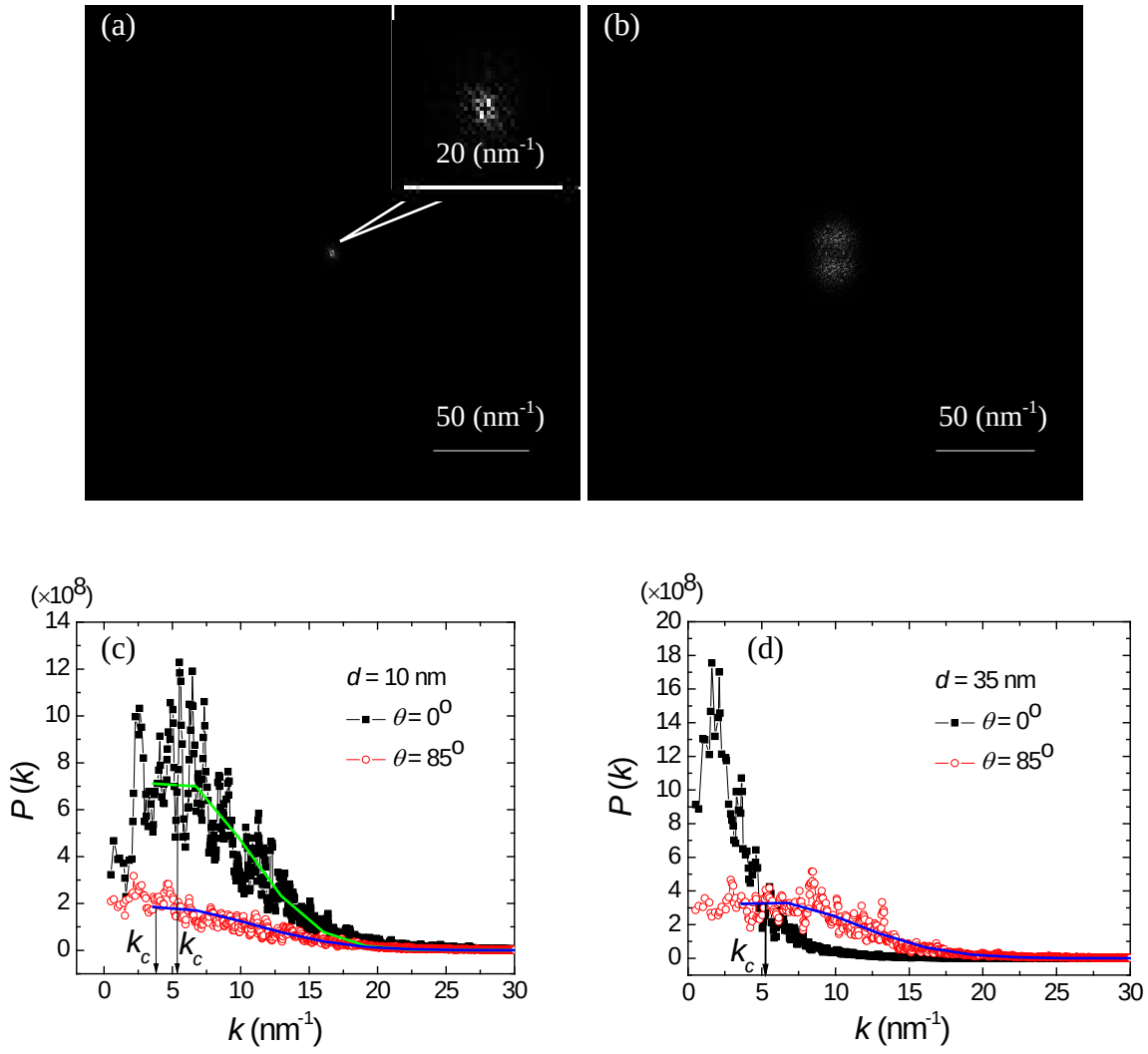

Figure 3.4 (a) The characteristic 2D power spectra of d = 35 nm, θ = 0° sample. (b) The characteristic 2D power spectra of d = 35 nm, θ = 85° sample. (c) The characteristic circular averaged power spectra of d = 10 nm at θ = 0° and 85°. (d) The characteristic circular averaged power spectra of 35 nm at θ = 0° and 85°.

As we can see in Figure 3.4(c), for d = 10 nm at θ = 0° and 85°, there is k_c for both cases. Normally, as k_c increases, the smaller the particle size distribution becomes.[134] From the AFM images, we observe the Ag nanoparticles at d = 10 nm and θ = 85° have more uniform size

distribution than those at d = 10 nm and θ = 0° but have a smaller k_c. The reason is that the particles are not close packed and the gap between the particles in the case of θ = 85° has also been counted into the particle size when the power spectrum calculation is used. As shown in Figure 3.4(d), when the thickness increases to 35 nm, in the case of θ = 0°, k_c is approaching to 0 and this is due to the coalescence between the large grains, which breaks the regularity of the surface.

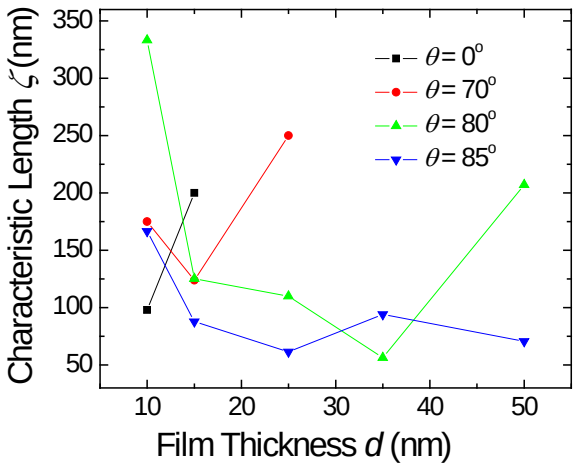

Figure 3.5 The relationship between the averaged wavelength of the periodic morphology ζ and the film thickness d.

The relationship between the k_c and the film thickness has been summarized in Figure 3.5. At θ = 0°, 70°, the characteristic length ζ ($=\frac{2\pi}{k_c}$) increases with the increasing d until the large particle starts to appear ($d \geq 20$ nm), which gives the random and rough morphology. At θ = 80°, 85°, ζ decreases first and then increases slightly with the increasing d. According to the AFM images, we can see that the nanoparticles did not form a closely packed monolayer at $d \leq 25$ nm, therefore the gap between the nanoparticles has also been counted into the characteristic length calculation. While increasing d, the gap between particles becomes smaller, which makes a small

ζ initially. After the gap closes, with increasing *d*, the particle size *D* increases of which leads to an increasing ζ. In addition, ζ is smaller at the larger deposition angle for the fixed thickness.

3.2.4 UV-Vis spectra of Ag nanoparticles film

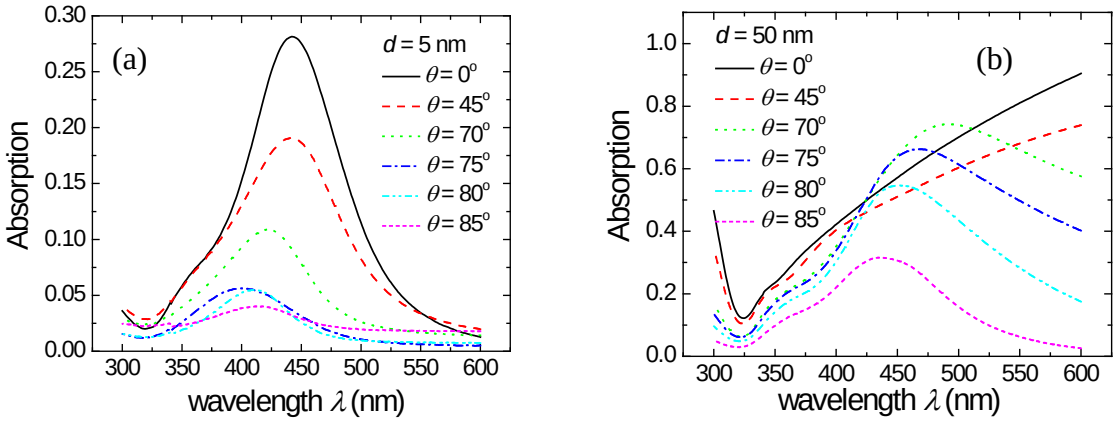

Figure 3.6 (a) Representative UV-Vis absorption spectra of Ag films at *d* = 5nm. (b) Representative UV-Vis absorption spectra of Ag films at *d* = 50nm.

Figures 3.6(a) and 3.6(b) show the typical un-polarized absorption spectra of thin Ag films on the glass substrates. For each UV-Vis spectrum, a SPRW λ_p was assigned as the wavelength corresponding to the extinction maximum. At *d* = 5 nm, the SPRW λ_p shows a clear trend of blue shift with increasing deposition angle. At *d* = 50 nm, we did not observe the SPRW for $\theta = 0°$ and $\theta = 45°$ in the wavelength range from 250 nm to 700 nm. For $\theta \geq 70°$, the SPRW λ_p decreases with the increasing deposition angle at a fixed film thickness. In fact, for each deposition angle, there is a critical thickness, d_c, beyond which one could not obtain the SPRW λ_p in the 250 nm-700 nm wavelength region. For example, at $\theta \geq 70°$, the critical thickness $d_c >$ 100 nm; at $\theta = 45°$, the critical thickness d_c = 35 nm; at $\theta = 0°$, the critical thickness d_c = 25 nm. We can expect that the Ag island film deposited at $\theta = 0°$ (normally d > 25 nm), which is

composed of large grains instead of nanoparticles, will have its plasmon peak located in the infrared region and the particle size distribution will be quite broad, which will result a broad width and is not favored by sensor application. These conditions make the normal deposited Ag island films not convenient and feasible for the biological test or sensor applications.

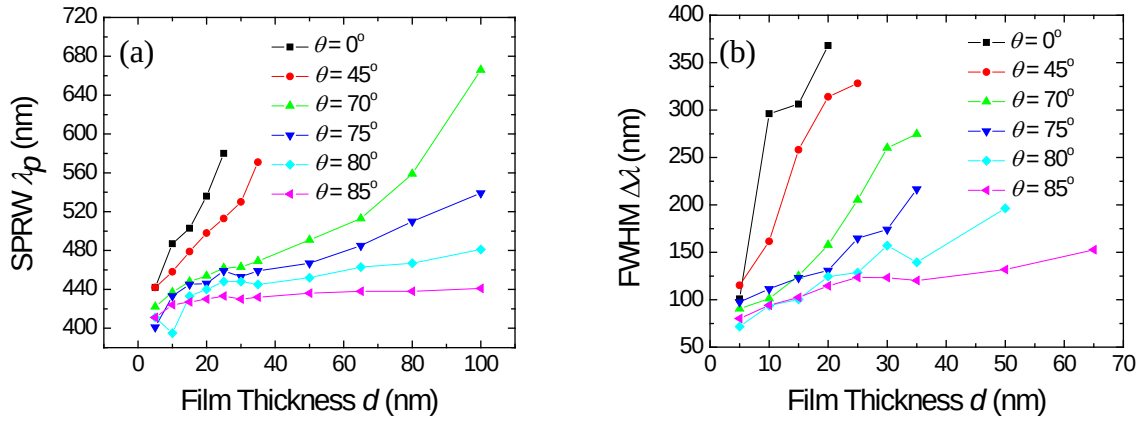

Figure 3.7 (a) The relationship between the SPRW λ_p and the film thickness d. (b) The relationship between the FWHM $\Delta\lambda$ and the film thickness d.

Figure 3.7(a) plots the relationship between the SPRW λ_p and the film thickness d. We observe the following characteristics: first, λ_p red shifts with the increasing thickness for a fixed θ and the $\lambda_p - d$ relationship is consistent with $D - d$ relationship shown in Figure 3.3(a), indicating a monotonic relationship between the size of the nanoparticle and the SPRW. One should note that since there is a large error bar for the particle size D when the thickness d increases to 50nm, this may be a reason for a relative small increment in SPRW λ_p in the corresponding range. It is well known that the optical properties of Ag particles within 20 nm to 200 nm diameters are strongly influenced by size effects. [135, 136] From the Mie theory, the SPRW λ_p red shifts with the increasing particle size. [58, 137] The average SPRW λ_p shift rate is decreasing with the increasing deposition angle as shown in Figure 3.7(a). At θ = 0°, the shift

rate is 6.5 nm red shift in wavelength per 1 nm increment in film thickness. At θ = 45°, the rate becomes 4.04, with a further increase of θ, the rate becomes 2.17, 1.18, 0.70 and 0.22 for θ = 70°, 75°, 80° and 85° respectively. These results indicate that the finer tunability can be achieved by using a large deposition angle. By estimation, the SPRW λ_p has an averaged red shift of 2-10 nm per 1 nm increment in particle size at $\theta \geq 70°$.

In addition to the peak shift, one also notes that the resonance absorbance band becomes narrower as θ increases for a fixed d. To characterize the width of the resonance absorbance band, a Lorentz function was used to fit each absorbance peak and the full width at half maximum (FWHM) $\Delta\lambda$ was obtained. Some of the spectra for the thicker Ag films are asymmetric (such as d = 50 nm, θ = 70° in Figure 3.6(b)), and are not able to be fitted by the Lorentz function. Therefore there are no FWHM data for those films. The relationship between the FWHM $\Delta\lambda$ and the film thickness d is plotted in Figure 3.7(b). It shows a similar trend as that between λ_p and d: the FWHM $\Delta\lambda$ increases with the increasing film thickness d for the fixed θ. Also, for a fixed d, $\Delta\lambda$ decreases with θ. The FWHM $\Delta\lambda$ is an indirect reflection of the particle size distribution. The more uniform the particle distributed, the narrower the $\Delta\lambda$. This $\Delta\lambda$ - d relationship is consistent with $\zeta - d$ relationship shown in Figure 3.5 for d > 15nm. As verified by the circular average power spectra, the particle size distribution is more uniform at the large deposition angle for a fixed d, or at the small d for a fixed θ. From the size effect, the SPRW is increasing with the increasing particle size, therefore a broad size distribution will result a broad FWHM. As we know, a narrow FWHM is advantageous for sensor application since the sharper the peak is, the easier the peak shift can be identified. The FWHM $\Delta\lambda$ of the Ag films at d = 5 nm or θ = 85° is between 75 nm to 125 nm, which are comparable to the LSPR sensor reported recently. [138, 139]

3.2.5 Polarized UV-Vis spectra of Ag nanoparticles film

When $\theta \geq 70°$, the growth is governed by a so-called geometric shadowing effect [123] which makes the vapor incident direction as the preferred growth direction of the particles. It is expected that most particles may have anisotropic shape and therefore the optical response of those particles is polarization dependent.

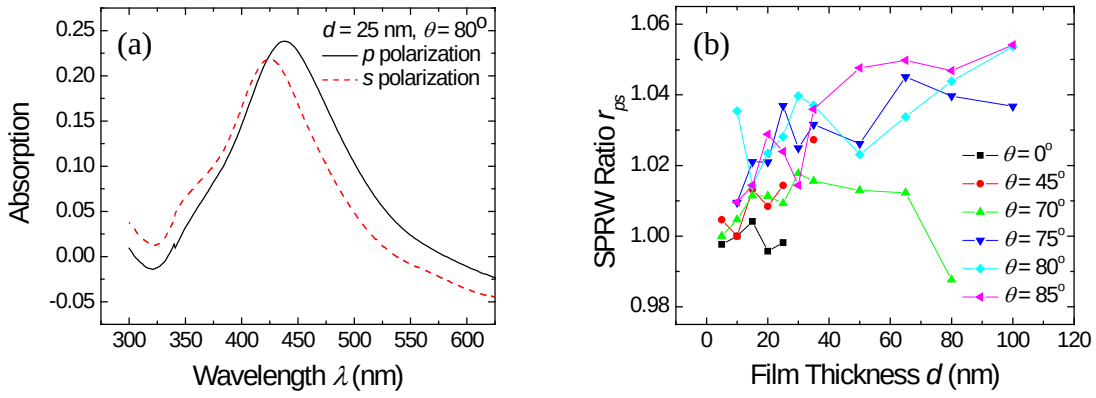

Figure 3.8 (a) Typical polarized UV-Vis absorption spectra of the Ag film (d = 25 nm, θ = 80°). (b) The relationship between the SPRW ratio r_{ps} and the film thickness d.

We carried out the polarized UV-Vis spectra measurements and found that the *p*-polarized SPRW red shifted compared with the *s*-polarized SPRW in most cases. One example is shown in Figure 3.8(a). At d = 25 nm and θ = 80°, the *s*-polarized SPRW located at 426 nm and the *p*-polarized SPRW red shifted to 438 nm. The ratio of the SPRWs for the *p*- and *s*-polarizations was defined as the SPRW anisotropic ratio r_{ps}. The relationships between r_{ps} and the film thickness d for different θ were plotted in Figure 3.8(b). The SPRW ratio fluctuates around 1 at $\theta \leq 70°$ and one cannot tell a defined trend. At $\theta \geq 75°$, the SPRW anisotropic ratio r_{ps} increases with the increasing film thickness. This is because the shadowing effect is more notable at $\theta \geq 75°$.

According to the power spectrum analysis, the particles have elongated shape and therefore can be treated as spheroid particles. In Gans theory, the absorption of spheroid particles is only dependent on the aspect ratio of the particles and not on the absolute dimensions. [58, 137] According to the oscillation direction of the incident electric field, the absorption band has two different modes: the high-energy band or the transverse mode (small SPRW) corresponds to the oscillation of the electrons perpendicular to the long axis of the particles (the direction of *s* polarization), and the low-energy band or the longitudinal mode (large SPRW) is caused by the oscillation of the electrons along the long axis of the particles (the direction of *p* polarization). The larger the aspect ratio is, the larger the energy separation between the resonance frequencies of these two plasmon modes, which means an increasing SPRW anisotropic ratio r_{ps}, as shown in Figure 3.8(b).

3.3 Ag nanoparticle based localized surface plasmon resonance biosensor for biotin-neutravidin interaction

3.3.1 Stability of Ag nanoparticle based LSPR biosensor

The Au or Ag nanoparticles have been used as chemical and biological sensors by measuring the shift in SPRW λ_p due to the adsorption of molecules on the particles' surfaces [92, 93, 138-142]. As a sensor material, the disadvantage of Ag is its ability of easy contamination from the environment. Therefore there is a need that the Ag nanoparticle film should provide a stable SPRW prior to the target analyte adsorption on the Ag surface.

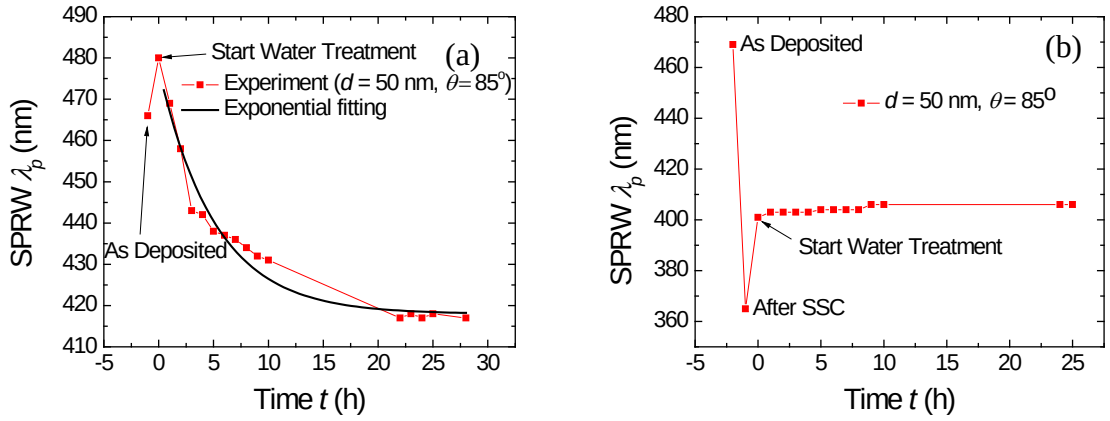

Figure 3.9 (a) Stability test for Ag nanoparticle film in DI water. (b) Stability test for SSC coated Ag nanoparticle film in DI water.

In most sensor applications, since the LSPR chip will be treated with the aqueous solutions, we first tested SPRW λ_p stability of the Ag nanoparticle film in the deionized water (DI water). To test the stability, we measured the UV-Vis absorption of three pieces of as-deposited Ag nanoparticle film (d = 10 nm and θ = 85°, d = 20 nm and θ = 85° and d = 50 nm and θ = 85°, respectively) before and after soaked them in DI water. For the samples d = 10 nm and θ = 85°, d = 20 nm and θ = 85°, since there is less Ag on the substrates, the intensity decreased significantly after the DI water treatment. Therefore we did not use them for further tests. The absorbance spectra of the sample d = 50 nm and θ = 85° were measured in real time for 28 hours during the water treatment, and the SPRW λ_p was extracted. Figure 3.9(a) shows how the λ_p changes by the water treatment: right after the Ag film was soaked in DI water, the SPRW λ_p red shifted from 466 nm to 480 nm, a change of $\Delta\lambda$ ~14 nm (t = 0h). This shift is due to the change of the dielectric environment; the refractive index of the water is larger than that of the air [143] and the sensitivity can be roughly estimated as 42 nm/refractive index unit (RIU). After one hour, the peak began to blue shift. The SPRW λ_p shifted faster in the first 5 hours and

then slowed down. After 28 hours of water treatment, the SPRW λ_p changed from λ_p = 480 nm (t = 0 h) to λ_p = 417 nm, a change of $\Delta\lambda$ ~ 63 nm. The SPRW at t = 28 h is even smaller than the λ_p of the as-deposited sample in air and could not be due to the dielectric environment effect. We believe that this is caused by the oxidation of Ag nanoparticle in the water. The Ag nanoparticles could be continuously oxidized in water and the Ag metal cores become increasingly smaller. The oxidation behavior of nanometallic particles has been studied both experimentally and theoretically [144-146], and the reduction of the metal core can be fitted by an exponential decay function. Since the initial particle size is a constant, the Ag metal core size, which is the difference between the initial particle size and the oxide thickness and is roughly proportional to the SPRW, shall also exponentially decay with time. An exponential decay fitting is shown in Figure 3.9(a).

To prevent this oxidation effect, a self assembled monolayer (SAM) can be used to protect the Ag surface. In the meantime, the SAM layer can also act as a linker between the Ag nanoparticle surface and the analyte. Based on this idea, we soaked a piece of as-deposited Ag film (d = 50 nm and θ = 85°) in 1X SSC buffer (150 mM Sodium Chloride, 15 mM Sodium Citrate) for 22 hours and performed the absorption measurement. The Ag nanoparticle film was then washed by DI water and immersed in DI water. The UV-Vis absorption spectra were measured and the change of SPRW λ_p as a function of water treatment time is plotted in Figure 3.9(b). The LSPR λ_p blue shifted from 469 nm to 365 nm after SSC incubation. This blue shift may be due to the etching of Ag nanoparticle in Cl^- solution. When the SSC coated Ag nanoparticle film was immersed in DI water, the λ_p red shifted from 365 nm to 401 nm due to the change of the dielectric environment. This shift corresponds to a sensitivity of ~108 nm/RIU. In the following 25 hours, the λ_p was stable and the SPRW shift is within 5nm during the whole

process. This result means that a SAM layer is an effective way to avoid the Ag nanoparticle oxidation in aqueous solutions.

3.3.2 Monitoring the specific binding of NeutrAvidin to Biotin

To study the selectivity of the LSPR based Ag nanoparticle film sensor, the system Biotin/NeutrAvidin was used for their high affinity. Figure 3.10 shows the process flow for monitoring the specific binding of NeutrAvidin to Biotin on the Ag nanoparticle surface. First, the Ag nanoparticles were fabricated on the glass substrate by OAD method. Second, to modify the Ag nanoparticle with biotin, a SAM of *N*-[6-(Biotinamido)hexyl]-3′-(2′-pyridyldithio) -propionamide (Biotin-HPDP) was immobilized on Ag surface. From the results discussed in Section 3.3.1, we believe that the Ag nanoparticles have been protected by Biotin monolayer. As a proof, the Biotin coated chip was put into DI water for stability test. After that, bovine serum albumin (BSA) was used to block the non-specific sites on Ag surface. Finally, different concentrations of NeutrAvidin were applied to Biotin modified Ag nanoparticle film, and the corresponding UV-Vis spectra were measured.

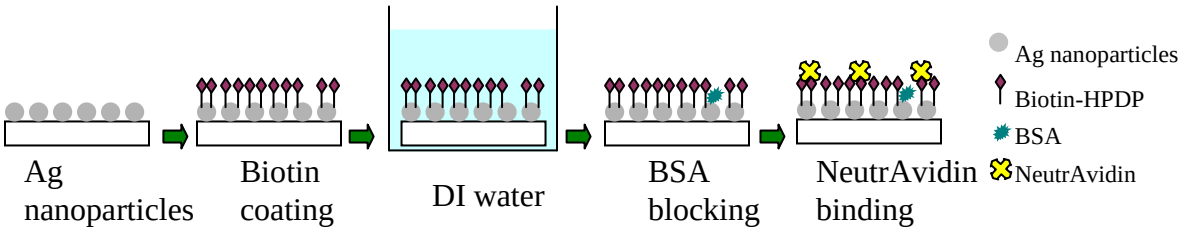

Figure 3.10 Process flow for monitoring the specific binding of NeutrAvidin to Biotin on the Ag nanoparticle film.

Biotin-HPDP was purchased from Thermo Scientific Pierce Protein Research Products (Rockford, IL) and NeutrAvidin was purchased from Pierce (Rockford, IL). Sodium chloride and

sodium citrate were all from J.T. Baker (Phillipsburg, NJ). All the chemicals were used as-received.

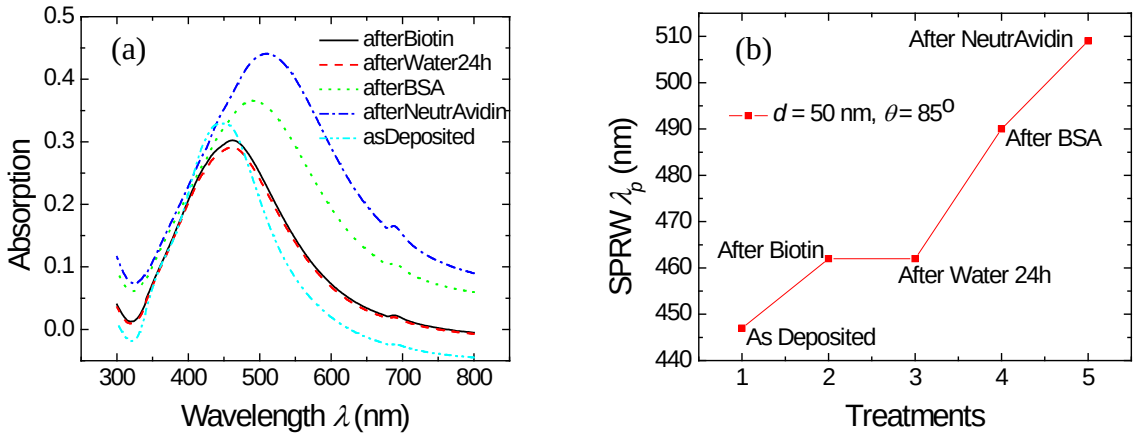

Figure 3.11 (a) Representative absorption spectra of Biotin/NeutrAvidin binding process. (b) The SPRW λ_p shift during Biotin/NeutrAvidin binding process.

The absorption spectra and the detailed λ_p shift are shown in Figures 3.11(a) and 3.11(b), respectively. Before any treatments, the absorbance spectrum of a fresh piece of Ag film (d = 50 nm and θ = 85°) was measured by UV-Vis spectrophotometer and λ_p was located at 447 nm. Then this Ag nanoparticle film was soaked in 10^{-4} M Biotin-HPDP solution and incubated under room temperature overnight. This Biotin coating made the SPRW λ_p red shift to 462 nm. To test the stability, the sample was immersed in DI water for 24 hours. As shown in Figures 3.11(a) and 3.11(b), the absorbance spectrum is stable after the DI water treatment, indicating no λ_p shift. Since there was a possibility of exposed bare Ag surface and the metal surface might be sticky for proteins, 5% BSA was used to block the non-specific sites for overnight. This treatment made the SPRW λ_p red shift 28 nm, which means the Biotin coating did not cover the entire Ag surface. And we believe the concentration of BSA is high enough and the incubation time is long enough to block the non-specific sites. Finally, the chip was exposed to 10^{-6} M NeutrAvidin at 4°C

overnight. The result indicated a further red shift of 19 nm due to the reaction between the Biotin and NeutrAvidin (Figure 3.11(b)). During the process, the Ag nanoparticle film was washed by DI water, dried in N_2 and measured by UV-Vis spectrophotometer after each step. These results are repeatable.

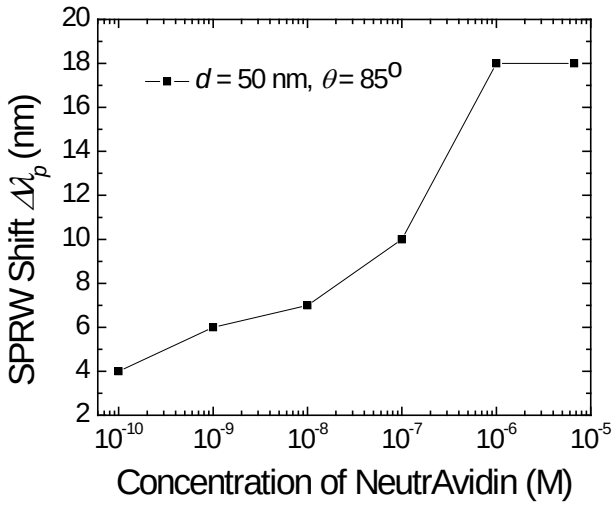

Figure 3.12 Concentration dependence of NeutrAvidin for SPRW shift $\Delta\lambda_p$.

To further monitor the specific binding between the Biotin and the NeutrAvidin, we varied the concentration of NeutrAvidin between 10^{-10} M and 10^{-5} M and measured the shift of λ_p after BSA blocking. Since the stability has been verified in the previous experiments, we skipped the water treatment step. As shown in Figure 3.12, a clear concentration dependence relationship further verified the specific binding between the Biotin and the NeutrAvidin. In detail, after treated by 10^{-6} M NeutrAvidin, a shift of 18 nm in SPRW λ_p was obtained and further increment of the NeutrAvidin concentration did not make the shift larger, which means the Ag surface coated with Biotin has a limited accommodation for NeutrAvidin molecules and the maximum detectable concentration is ~ 10^{-6} M for our current LSPR sensor. While 10^{-10} M

NeutrAvidin made SPRW λ_p shift 4 nm and still left some spaces for detection of even lower concentration. Since this λ_p shift falls into the error range in the stability test, we could say that the limit of detection (LOD) for this LSPR based Ag film sensor is 10^{-10} M for NeutrAvidin. There is still much room to improve the detection dynamic range. For example, the large λ_p shift after BSA blocking means the surface coverage of Biotin is not optimum. One can further optimize the Biotin coating so that the Ag surface can accommodate more NeutrAvidin molecules, therefore improving the LOD. On the other hand, we used the Ag films with 50nm thickness and 85° deposition angle in these experiments. Since we can easily tune the λ and change the band width of the absorption spectrum, we believe there is also space left for LOD optimization.

3.4 Au nanoparticle based localized surface plasmon resonance biosensor for *Salmonella* detection

In our previous work, we have demonstrated that Ag NPs film fabricated OAD technique is good LSPR substrate for the biotin-NeutrAvidin reaction.[147] However, the Ag NPs suffer from chemically unstable problem when directly exposed to the outer environment, especially in the aqueous solutions. In order to overcome this problem, we aim to build a LSPR sensor for *Salmonella* detection using Au NPs fabricated by OAD.

3.4.1 Au nanoparticles fabrication and their response to the surrounding medium

We believe that, regarding the morphologies and absorption spectra of the Au NPs and the Ag NPs, the trends should be similar except that their plasmon peak locations will be

different. In this section, we are going to discuss the fabrication of Au NPs and their LSPR response of Au NPs to the change of the surrounding medium.

3.4.1.1 Au NPs fabricated by OAD and GLAD

Au NPs were fabricated by OAD and GLAD method using the custom-designed electron-beam evaporation system (Torr International, Inc.). The morphologies of the Au NPs substrates were characterized by an AFM (VEECO Dimension 3100) with a tapping mode. The scan rate was 1-2 Hz and the scan size was 1μm×1μm. For all the depositions, the background pressure in the chamber was 1 × 10^{-6} Torr, and the deposition rate was approximately 0.1-0.3 Å/s. The absorbance spectrum of the substrate was measured by an UV-vis-NIR double beam spectrophotometer (JASCO V-570). The light source was unpolarized. Au (99.99%), Ti (99.995%) and Cr (99.998%) were from Kurt J. Lesker Company (Clairton, PA).

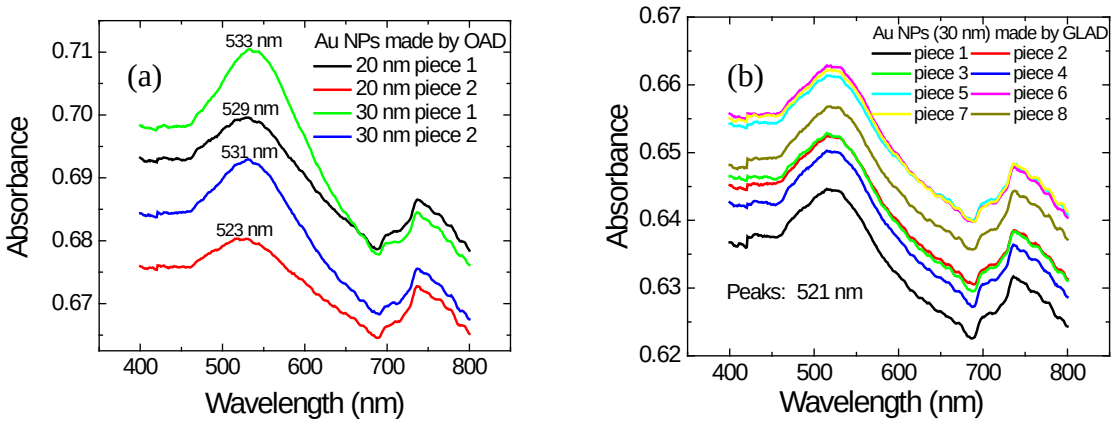

Figure 3.13 Absorbance spectra of Au NPs made by (a) OAD and (b) GLAD.

The absorbance spectra of Au NPs made by OAD and GLAD are shown in Figure 3.13. As we can see, the plasmon peak positions are different for OAD samples: for 20 nm thickness, the peaks are 523 nm and 529 nm; for 30 nm thickness, the peaks are 533 nm and 531 nm

(Figure 3.13 (a)). While for the GLAD samples, eight substrates were measured and found that their peaks are all at 521 nm (Figure 3.13(b)). In OAD configuration, the distance between different substrate to the material source is varied, which will influence the real thickness of Au NPs. Therefore, during the deposition, the rotation of the substrate can diminish the space difference and make the substrates more uniform than those made by OAD.

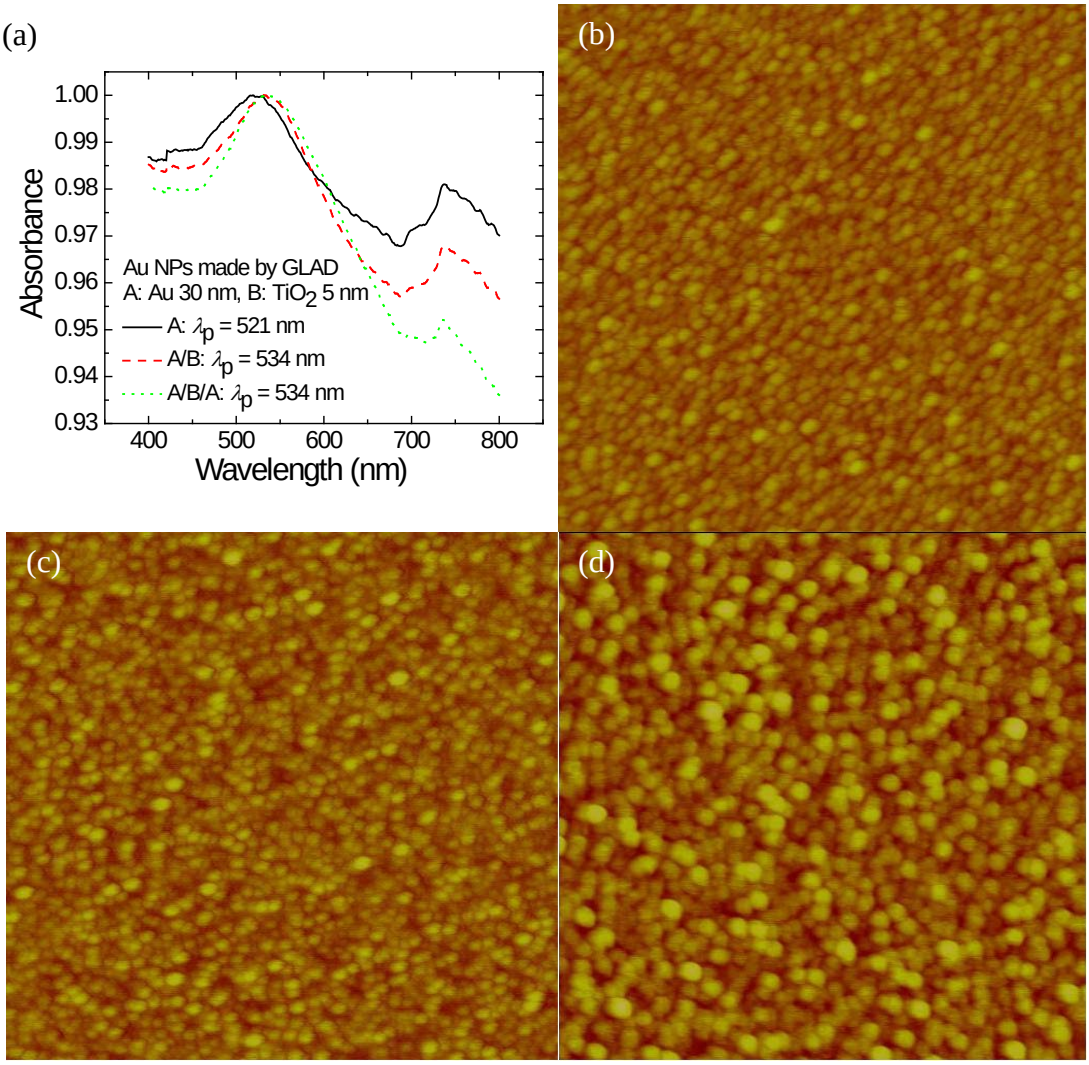

Figure 3.14 (a) Normalized absorbance spectra of substrates A, A/B and A/B/A. A: Au NPs made by GLAD (QCM reading 30 nm). B: TiO_2 deposition by GLAD (QCM reading 5 nm). AFM images of substrates (b) A, (c) A/B and (d) A/B/A.

Further, TiO_2 film with QCM reading 5 nm was deposited onto Au NPs (30 nm) made by GLAD. After that, 30 nm more Au was deposited onto TiO_2 by GLAD. Figure 3.14 (a) shows the normalized absorbance spectra of the above substrates. It can be seen that, after TiO_2 deposition, the plasmon peak shifts from 521 nm to 534 nm due to the changing dielectric around Au NPs. Interestingly, another 30 nm Au deposition does not make the plasmon peak further shift. According to the AFM images (Figure 3.14 (b) - (c)), TiO_2 deposition does not increase the size of the NPs, while after the second Au deposition, the size of the NPs increases greatly (Figure 3.14 (d)). Though it is not clear if the increasing Au NPs surface area is helpful for *Salmonella* detection, we believe that this kind of interesting structure has potential for LSPR sensor applications.

3.4.1.2 Au nanoparticles' LSPR response to the surrounding medium

Au NPs were fabricated by OAD method using a thermal evaporator (Thermionics Laboratory, Inc.). The experimental setup was the same with the Ag NPs fabrication: we used the same angled wedges with preset angles of θ = 75°, 80° and 85°, and mounted them onto the flat substrate holder. The QCM reading of Au NPs deposition would be fixed as 10 nm in the entire discussion.

In order to see how the local environment changes the LSPR property of Au NPs, Ti was deposited onto the Au NPs using the custom-designed electron-beam evaporation system (Torr International, Inc.) in three different ways: (1) at a fixed deposition angle θ_{Ti} = 0°, different thickness of Ti d_{Ti} = 2, 5, 8, 10, 15 and 20 nm was deposited onto Au NPs samples with different deposition angles of θ = 75°, 80° and 85°, respectively; (2) at a fixed thickness d_{Ti} = 2 nm, Ti was deposited at different deposition angles of θ_{Ti} = 0°, 45°, 65° and 85° onto Au NPs samples

with different deposition angles of θ = 75°, 80° and 85°, respectively; (3) at a fixed deposition angle θ_{Ti} = 85°, different thickness of Ti d_{Ti} = 2, 10, 30 and 50 nm was deposited onto Au NPs samples with different deposition angles of θ = 75°, 80° and 85°, respectively.

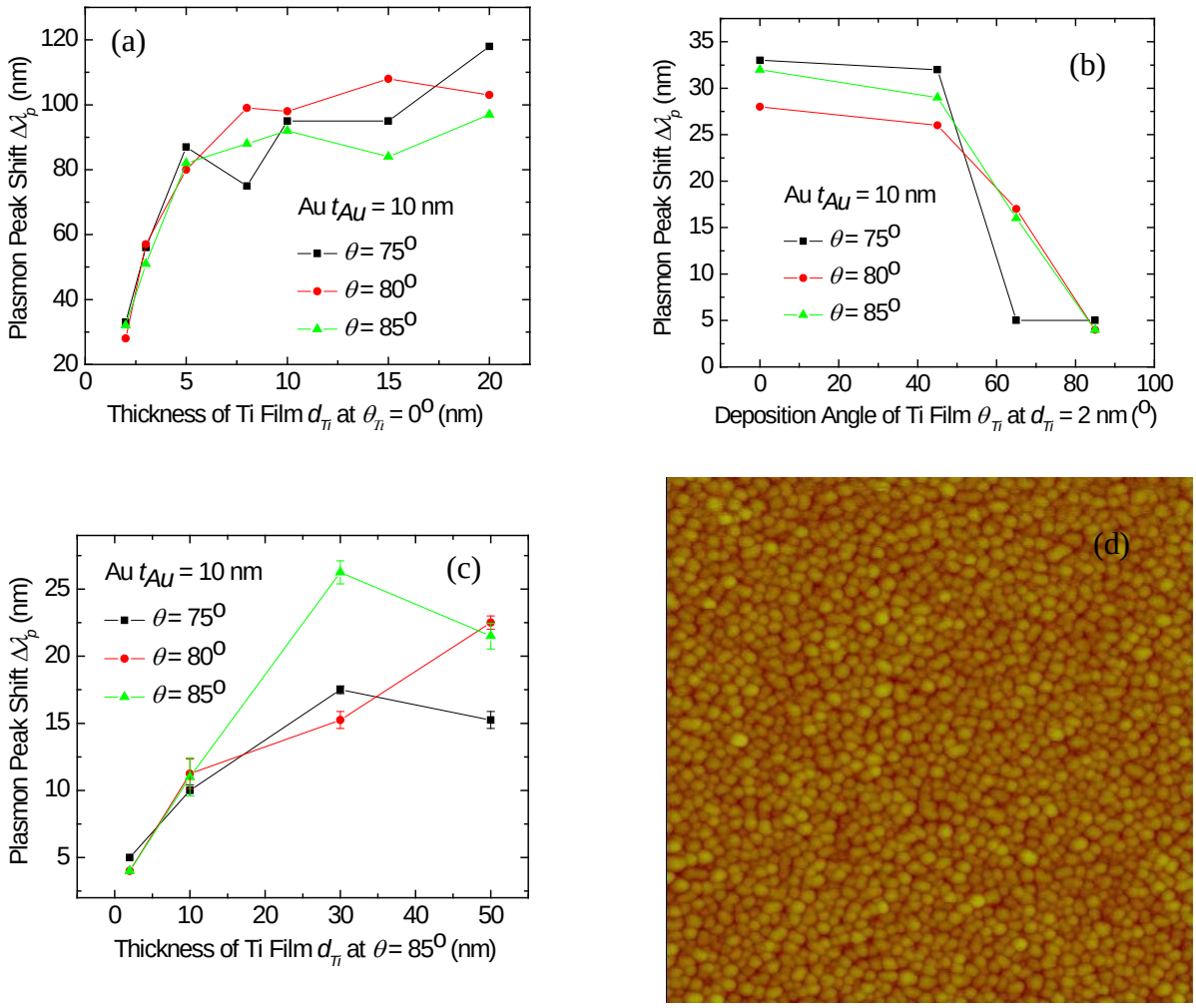

Figure 3.15 Relationship between the plasmon peak shift of Au NPs and (a) thickness of Ti d_{Ti} at θ_{Ti} = 0°; (b) deposition angles of Ti θ_{Ti} at d_{Ti} = 2 nm; (c) thickness of Ti d_{Ti} at θ_{Ti} = 85°. (d) A representative AFM image of Au nanoparticles (D = 30 nm).

First, as shown in Figure 3.15 (a), for all the Au NPs substrates, the plasmon peak shift $\Delta\lambda_p$ before and after Ti deposition increases with the increasing thickness of Ti d_{Ti} at θ_{Ti} = 0°. When $d_{Ti} \leq 5$ nm, the $\Delta\lambda_p$ for different deposition angles of Au NPs is close to each other. The

discrepancy becomes large when d_{Ti} > 5 nm, though there is no obvious trend for different Au NPs substrates. As a matter of fact, researchers have found that the plasmon peak shift is proportional to $(1-e^{\frac{-2z}{l_d}})$, where z is the distance from the metal NP and l_d is the characteristic decay length of the local electric field.[148, 149] Because of the exponential increase, the shift will saturate at a critical distance z_c, which depends on the size, shape distribution and composition of the metal NPs.[150, 151] Combining the results of the Au spherical NPs based LSPR sensors from literature [150, 152, 153] and the measured results, we estimate that the critical distance z_c for Au NPs in this study is 20 nm and the maximum $\Delta\lambda_p$ is around 100 nm.

As shown in Figure 3.15 (b), the plasmon peak shift $\Delta\lambda_p$ decreases with the increasing deposition angles of Ti θ_{Ti} at d_{Ti} = 2 nm. Due to the geometric effect, the area receiving the Ti atoms on the Au NPs is different for different deposition angles of Ti θ_{Ti}. Since the smaller coverage on the Au NPs can cause smaller change of the surrounding medium, the plasmon shift will be smaller. Also, the plasmon peak shift $\Delta\lambda_p$ increases slowly with the increasing thickness of Ti d_{Ti} at a smaller coverage (θ_{Ti} = 85°), as shown in Figure 3.15 (c). For example, at d_{Ti} = 10 nm, $\Delta\lambda_p$ is around 95 nm for θ_{Ti} = 0° but only 10 nm for θ_{Ti} = 85°.

3.4.2. *Salmonella* detection by Au NPs based LSPR sensor

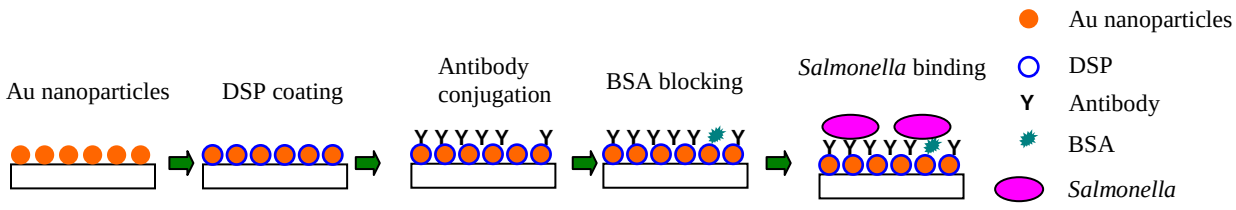

Figure 3.16 Flow chart of Salmonella detection by Au NP based LSPR sensor.

We choose the Au NPs substrate with a thickness of 10 nm at deposition angle θ = 85° for *Salmonella* detection. A typical atomic force microscope (AFM) image of the Au NPs substrate with a thickness of 10 nm at deposition angle θ = 85° is presented in Figure 3.15 (d). As we can see, the particles have a roughly spherical shape and the size distribution is uniform. By estimation, the average diameter *D* of the Au NPs is around 30 nm. Since the substrate will be treated by aqueous solutions, a thin adhesion layer of Cr film with a thickness of 2 nm is thermally deposited onto the glass prior to the Au deposition.

To detect the *Salmonella* bacteria, the Au NP substrate was treated step by step by following the flow chart shown in Figure 3.16. First, 100 μl of 5 mg/ml dithiobis(succinimidyl propionate) (DSP) which has been dissolved in dimethylsulfoxide (DMSO) was applied to the Au surface for a half hour under room temperature (RT). Since the *N*-hydroxysuccinimide (NHS) esters can easily react with the water, the Au NPs substrate was rinsed by DMSO and the deionized (DI) water to remove the unbound molecules, and immediately dried in nitrogen. Then 100 μl of 100 μg/ml anti-*Salmonella* in phosphate buffered saline (PBS) was added to the sample chip, which was then incubated for one hour under RT and transferred to 4°C overnight. After that, 100 μl of 5% bovine serium albumin (BSA) in PBS was used to block the non-specific sites on the sample surface and incubated under RT for two hours. The concentration of BSA can be determined by finding out the saturated plasmon shift when using different dilutions of BSA. The functionalized Au NP substrate was now ready for *Salmonella* detection, and it was incubated with 100 μl of *Salmonella* in PBS under RT for one hour and then transferred to 4°C overnight. After each step, the substrate was rinsed by DI water, dried by nitrogen, and the absorbance spectrum measured.

DSP was from Pierce Chemical (Rockford, IL). DMSO, BSA and PBS were all from Sigma-Aldrich (St Louis, MO). Unlabeled anti-*Salmonella*, anti-*Salmonella* labeled with fluorescein isothiocyanate (FITC) and killed *Salmonella* (*Salmonella typhimurium* strain) were obtained from Kirkegaard & Perry Laboratories, Inc. (KPL, Gaithersburg, MD). All the chemicals were used as received.

Figure 3.17 (a) shows the absorbance spectra measured during the *Salmonella* detection step by step. First, Au NPs with a diameter D = 30 nm is measured in air and the plasmon peak locates at 609 nm. Then DSP in DMSO is applied to the surface and the disulfide linkage rapidly chemisorbs to gold surface. The measured result shows that the plasmon peak only red-shifts by 2 nm. After being rinsed by DMSO and DI water in sequence, anti-*Salmonella* antibodies are added to the DSP-coated Au NP's surface and the active NHS esters on either end of DSP are reactive toward primary amine groups of antibodies. As we expected, the anti-*Salmonella* conjugation makes a significant plasmon peak shift from 611 nm to 638 nm. Since the antibody has a larger molecular weight than that of DSP, it should be able to change the surrounding dielectric constant more than DSP does. To block the non-specific sites on the surface, BSA in PBS is used as the blocking agent. Due to the high concentration of anti-*Salmonella* used for the sample, most of surface should have been covered by antibodies. Thus the BSA blocking only makes the plasmon peak shift by 5 nm. After finishing the above procedures, the functionalized Au NPs substrate is ready for *Salmonella* detection, which can be accomplished by the binding of *Salmonella* cells onto the anti-*Salmonella*. A high concentration of *Salmonella*, 10^8 cfu/ml, is used in this test.

However, we find that the plasmon peak blue-shifts from 643 nm to 640 nm. To further understand the detection result, we use five different concentrations of *Salmonella*, i.e., 10^4, 10^5,

10^6, 10^7, and 10^8 cfu/ml, to explore if there is a concentration-dependent relationship. The plasmon peaks λ_p after each step are plotted in Figure 3.17 (b). First, different Au NPs substrates in the same batch are not exactly uniform and their plasmon peaks range from 602 nm to 613 nm. After DSP coating, the plasmon peaks red-shift by 0~2 nm except for that of the 10^6 cfu/ml *Salmonella*. Consistently, the anti-*Salmonella* conjugation makes all the plamon peaks λ_p of different substrates shift by 25-27 nm. However, after BSA incubation, the plasmon peaks either red-shift or blue-shift in a small range, and *Salmonella* binding only makes a shift of 3, 0, 3, -2, -3 nm for 10^4, 10^5, 10^6, 10^7, and 10^8 cfu/ml, respectively. The minus sign indicates a blue shift. Obviously, there is no concentration dependence observed from the detection results.

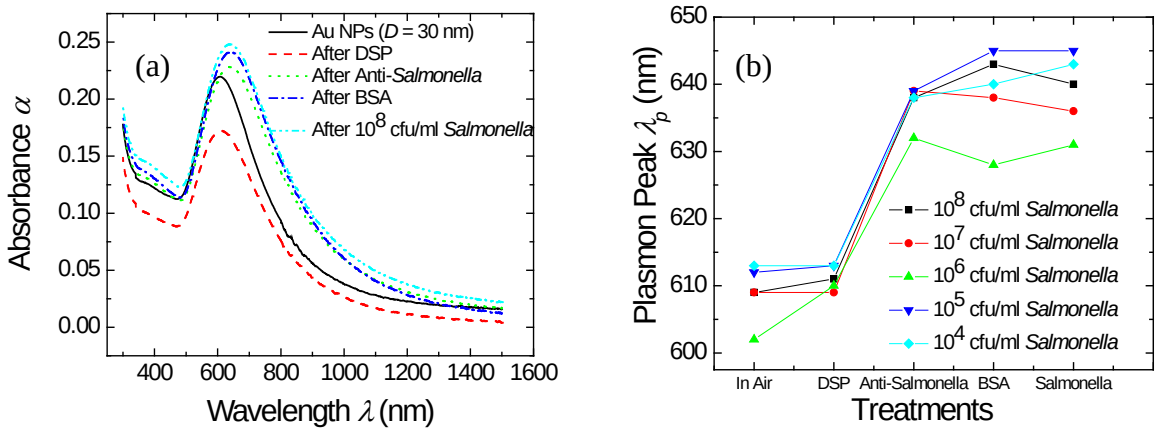

Figure 3.17 (a) Absorbance spectrum (b) Plasmon peaks of Salmonella detection by LSPR sensor.

There are two possible reasons for the detection results. One is that *Salmonella* is not been captured by the anti-*Salmonella* coated on the Au NPs surface. Another is that the detection ability of this LSPR sensor is limited. We first use the straight forward methods to inspect the binding between *Salmonella* and anti-*Salmonella*. Figure 3.18 (a) is the cross section scanning electron microscopy (SEM, LEO 982) image of the Au NPs substrate after 10^7 cfu/ml *Salmonella* incubation. Clearly, there are a lot of elongated black particles on the surface, which

we believe are *Salmonella* bacteria. Since they have different orientations, their length appears to be different. To further verify the binding between *Salmonella* and anti-*Salmonella*, 100 μl of 100 μg/ml FITC labeled anti-*Salmonella* is applied to the sample after 10^7 cfu/ml *Salmonella* treatment and incubated under RT for one hour and transferred to 4°C overnight. After rinsing with DI water the sample is imaged by the fluorescence microscope (Olympus BX60, 100× objective) and the image is shown in Figure 3.18 (b).

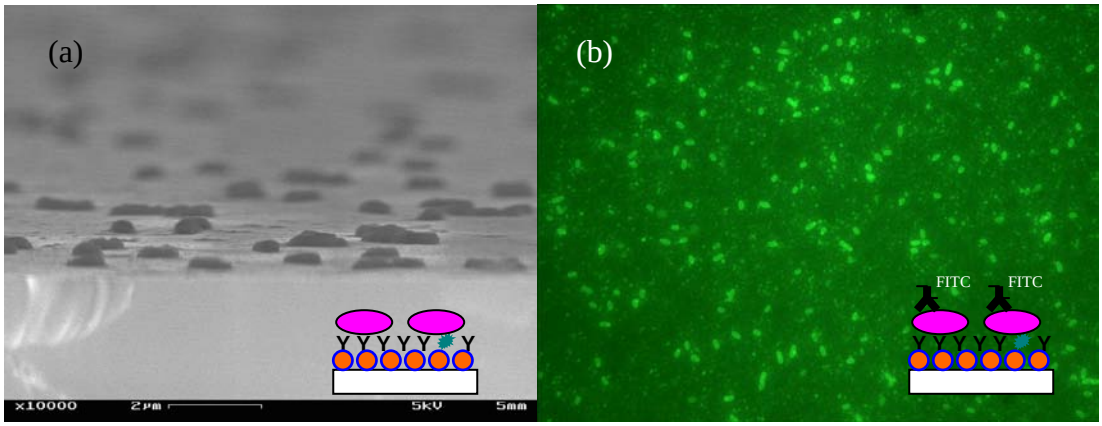

Figure 3.18 (a) SEM image (cross section) and (b) Fluorescence image of the Au nanoparticles substrate after 107 cfu/ml Salmonella detection.

As observed in the SEM image, there are a lot of particles on the surface. Since we use FITC labeled anti-*Salmonella* as the probe, it can be confirmed that these particles are *Salmonella* bacteria which have been captured by anti-*Salmonella* coated on the Au NPs surface. Therefore, the binding between *Salmonella* antigen and anti-*Salmonella* antibody is successful, but the LSPR sensor does not response to the concentration change.

3.4.3 Silica beads and polystyrene spheres detection by Au NPs based LSPR sensor

Compared to the Au NPs (D = 30 nm), the bacterium is much larger (~ 2 μm long). Thus, the contact area between Au NPs and bacteria could be too small, and there may not be enough

change for the surrounding environment of a single NP, and resulted in a definite plasmon peak shift. This prompts us to explore the limitation of the LSPR sensor and bring up an important assumption: the bacterium is a rigid body. If such an assumption is correct, any rigid body with a larger size than that of the Au NPs should not induce a significant plasmon peak shift. To verify this, we use silica beads (Bangs Laboratories, Inc.) with a radius R = 1 μm and polystyrene spheres (PS, Bangs Laboratories, Inc.) with a radius r = 25 nm as the analogs. To see if the rigid spheres can be detected by the LSPR sensor, 100 μl of 200 mg/ml silica beads or PS in DI water were dropped onto the Au NP-coated surface and air dried. As shown in Figure 3.19 (a), a silica bead coating makes the plasmon peak of Au NPs red-shift by 3 nm averagely and the absorbance intensity significantly increases due to the scattering by beads. Similarly, the averaged plasmon peak shift is about 6 nm in the case of PS coated Au NPs substrate (Figure 3.19 (b)). We note that the plasmon peak shifts due to the silica beads or PS are very close to those induced by *Salmonella* bacteria. From the point of view with the LSPR sensor principle, it becomes essential to know how the surrounding environment of the Au NPs is changed by the coated particles.

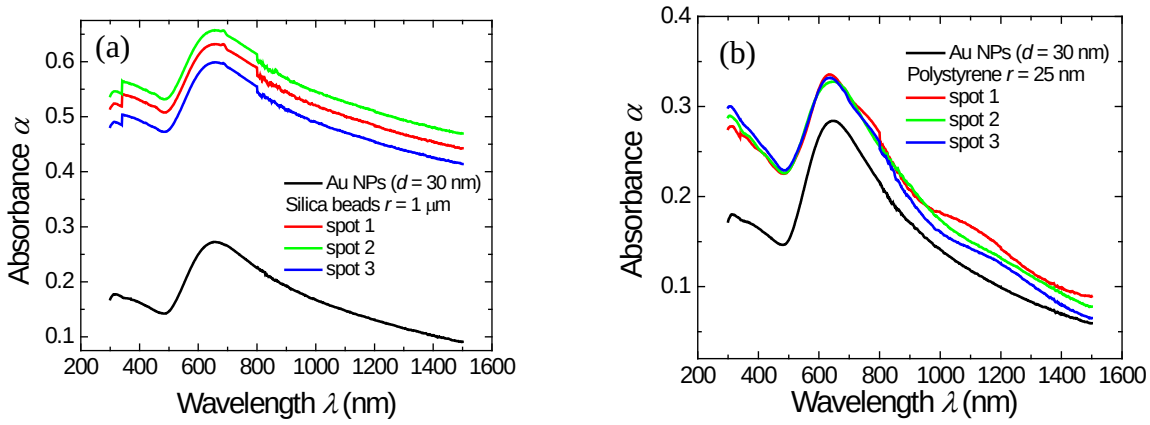

Figure 3.19 Absorbance spectra of (a) silica beads and (b) polystyrene coated Au nanoparticles substrates.

We take SEM (FEI Inspect F) images for silica beads coated on the substrate to obtain more information about the surrounding environment of the Au NPs. The SEM top view (Figure 3.20 (a)) shows that there are multilayers on the surface and the number of layers are different at different locations, which corresponds to the different absorbance intensities shown in Figure 3.19 (a). Figure 3.20 (b) is the SEM cross section image, which clearly shows that the silica beads have a point contact with the Au NPs surface, thus most of the local environment of the Au NPs is still air. We believe that the situation will be the same for the PS because they are all rigid spheres.

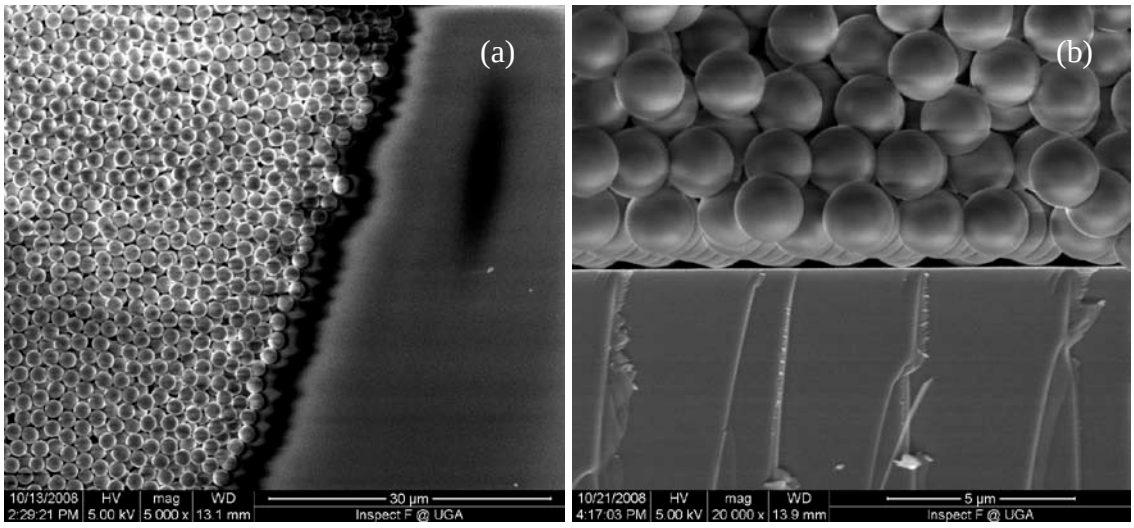

Figure 3.20 (a) SEM top view image and (b) SEM cross section image of silica beads coated on Au nanoparticles substrates.

3.4.4 Limitation of the LSPR sensor and the theoretical explanation

After introducing the effective medium theory, we continue to discuss the above detection results by the Au NPs based LSPR sensor. According to the SEM images shown in Figure 3.20 (b), the surrounding environment of Au NPs is still dominantly occupied by air after the particle coating. To understand how the plasmon peak of Au NPs will shift under the above

situation theoretically, we construct a simplified contact model for NP-rigid body system as shown in Figure 3.21 (a): a single Au NP with a diameter of *d* is point contacted with a spherical particle which has a radius of *r*; the shell between the Au NP and the dotted sphere with a diameter of (*d* + 2*t*) will be considered as the surrounding medium of the Au NP. It is well known that the change of the dielectric constant of the surrounding medium will cause the Au NP's plasmon peak to shift, which can be calculated by Mie theory:[154]

$$Q(\lambda) = \frac{3\pi N d^3 \varepsilon^{3/2}}{\lambda \ln(10)} [\frac{\varepsilon_i}{(\varepsilon_r + 2\varepsilon)^2 + \varepsilon_i^2}], \tag{3.15}$$

where *Q* is the extinction, *N* is the area density of Au NPs, *d* is the diameter of Au NP, ε is the dielectric constant of the surrounding medium, λ is the wavelength of the incident light, ε_i and ε_r are the imaginary portion and the real portion of the Au NP's dielectric function ε_{Au}, respectively, which is calculated by following Lucia B Scaffardi's work.[89] We should address two points here; 1) since the angular frequency ω is related to the wavelength λ, ε_{Au} is a function of the incident light wavelength λ; 2) in addition, for nanoparticles, the damping frequency γ has been modified to be a function of Au NP's diameter *D*, thus ε_{Au} also depends on the size of Au NPs.

If we treat the shell between the Au NP and the dotted sphere as an effective medium layer (EML) with a thickness of *t*, divide the part of the spherical particle (silica bead or PS) enclosed in the EML into many small spheres and uniformly embed them in the EML, the dielectric constant ε of the surrounding medium can be estimated by Maxwell-Garnett effective medium theory (Appendix B):[155]

$$\frac{\varepsilon - \varepsilon_p}{\varepsilon_p + L(\varepsilon - \varepsilon_p)} = (1 - f_p)[\frac{\varepsilon_a - \varepsilon_p}{\varepsilon_p + L(\varepsilon_a - \varepsilon_p)}], \tag{3.16}$$

where ε_p and ε_a are the dielectric constants of particles and air, respectively; L is the depolarization factor and is 1/3 for the sphere; f_p is the volume fraction of the particles:

$$f_p = \frac{2h_1^2(3r - h_1) + h_2^2[3(2t + d) - 2h_2]}{(2t + d)^3 - d^3}, \tag{3.17}$$

$$h_1 = \frac{t^2 + td}{2r + d}, \tag{3.18}$$

$$h_2 = t - h_1 \tag{3.19}$$

Combining the equations (3.15) – (3.19), we realize that the extinction Q is a function of the incident light wavelength λ and the EML thickness t. For a given t, there is an extinction spectrum curve E vs. λ, which can be calculated by using MatLab 6.1 (The MathWorks, Inc.), and two typical curves are shown in Figure 3.21 (b). With a zero thickness of t, the plasmon peak of Au NP (d = 30 nm) in air is 505 nm. When t = 15 nm (silica bead coating), the plasmon peak red-shifts to 508 nm.

It is clear that there is a one-to-one correspondence between the EML thickness t and the plasmon peak λ_p. Thus, the plasmon peak shift $\Delta\lambda$ after the PS or silica bead coating will also be a function of t, and this $\Delta\lambda$ - t relationship has been plotted in Figure 3.21 (c). As a whole, the plasmon peak shift $\Delta\lambda$ increases with the increasing thickness t. In detail, when $t \leq 2$ nm, the plasmon peak has no shift; when t increases to 5 nm, $\Delta\lambda$ is only 1 nm; when $t > 5$ nm and $t \leq 25$ nm, $\Delta\lambda$ increases from 1 nm to 4 nm for silica bead and from 1 nm to 2 nm for PS. By comparison, silica bead makes a larger and faster-increasing plasmon peak shift than PS.

This model can be extended to the case of *Salmonella* which has been assumed to be a rigid rod, and the configuration is shown in Figure 3.22 (a). To calculate the effective dielectric constant of the EML, we need to know the refractive index of *Salmonella*. According to the literature,[156, 157] researchers normally use n_1 = 1.45 as the refractive index of the protein

layer. Therefore we use it as the lower limit and use a higher one n_2 = 1.55 as the upper limit. Based on these assumptions, the relationship between plasmon peak shift $\Delta\lambda$ and the EML thickness t is shown in Figure 3.22 (b). As we can see, when $t \leq 2$ nm, the plasmon peak has no shift; when t increases to 5 nm, $\Delta\lambda$ is only 1 nm; when $t > 5$ nm and $t \leq 25$ nm, $\Delta\lambda$ increases from 1 nm to 4 nm for n_1 = 1.45 and from 1 nm to 5 nm for n_2 = 1.55. For a larger refractive index of *Salmonella*, the plasmon peak shift $\Delta\lambda$ is larger and increases faster with the increasing EML thickness t.

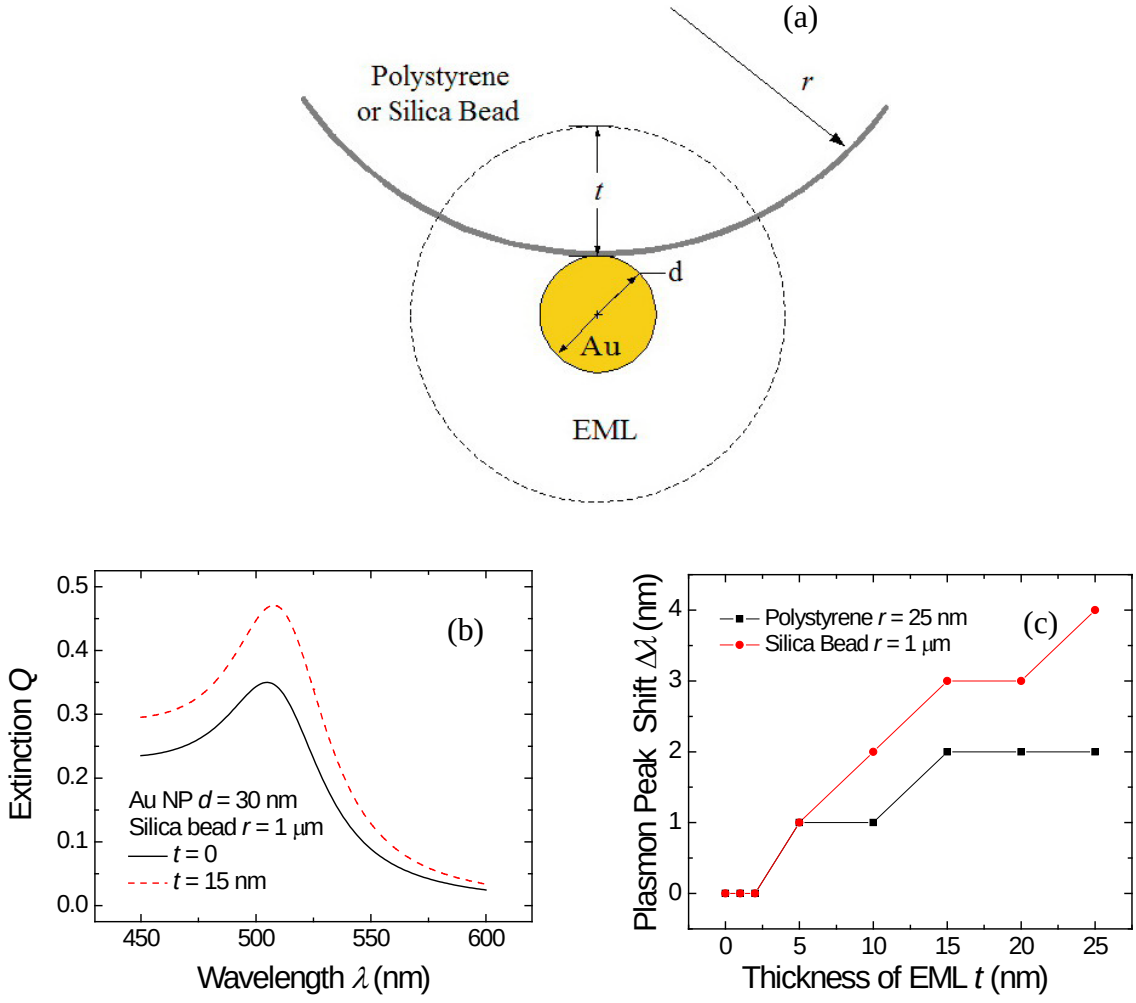

Figure 3.21 (a) Theoretical model of Polystyrene or silica bead detection by single Au NP. (b) The relationship between the plasmon peak shift $\Delta\lambda$ and the thickness of effective medium layer t.

The above results indicate that the farther the local electric field of the Au NP goes into the target particle, the more the plasmon peak of Au NP shifts. We have estimated that the critical distance z_c for Au NPs in this study is 20 nm. As a result, the plasmon peak shift caused by PS, silica bead, and *Salmonella* is 2, 3, 3 to 4 nm, respectively. This is very close to our experimental results.

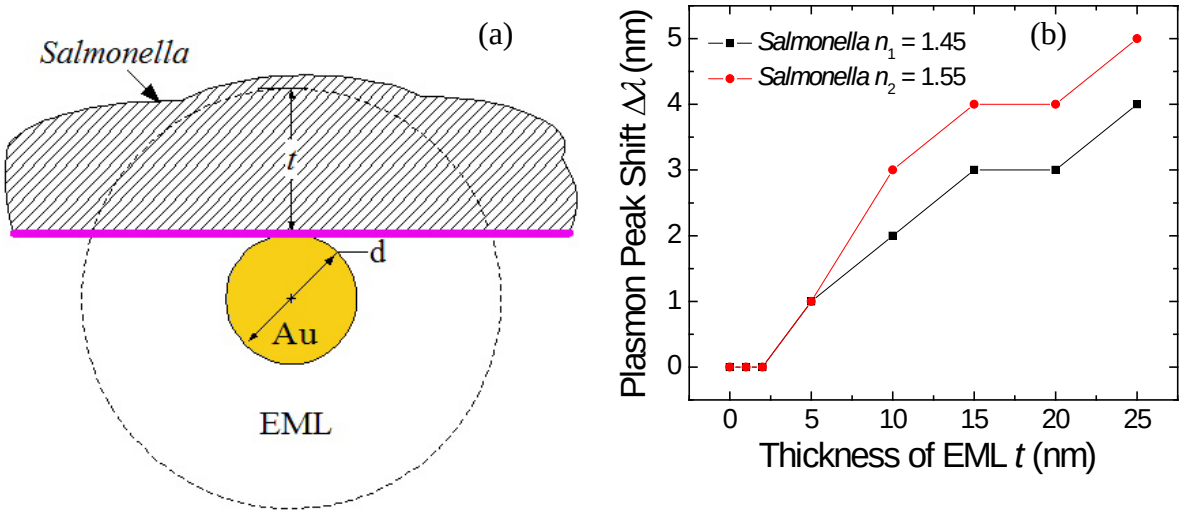

Figure 3.22 (a) Theoretical model of Salmonella detection by single Au NP. (b) The relationship between the plasmon peak shift $\Delta\lambda$ and the thickness of effective medium layer *t*.

Regarding the concentration dependence, our previous study shows a clear concentration-dependent relationship between biotin and NeutrAvidin, because the surface coverage on the Au NP increases with the increasing concentration of NeutrAvidin.[147] However, in the case of PS, silica bead, or *Salmonella* bacterium, a Au NP can at most contact with one sphere or bacterium cell, which only can induce a plasmon peak shift of 2-4 nm as theoretically verified above. Therefore, we conclude that the rigid bodies such as PS, silica beads, and *Salmonella* bacteria can be detected via the LSPR sensor with a small plasmon peak shift, but the concentration dependence can not be obtained. On the other hand, since the local electric field exponentially decays in the EML,[148, 149] we actually overestimated the dielectric constant of the EML by

uniformly distributing the small target analyte spheres into the EML, which means the theoretical plasmon peak shift might be even smaller. In addition, a simple test for the instrumental systematic error is performed by adding ten absorbance measurements of air to a typical absorbance spectrum of Au NP, and the calculated standard deviation is 2.14 nm. We think the overestimation and the systematic error should be responsible for the discrepancy between theoretical and experimental results, and the blue shifts observed in the experimental results.

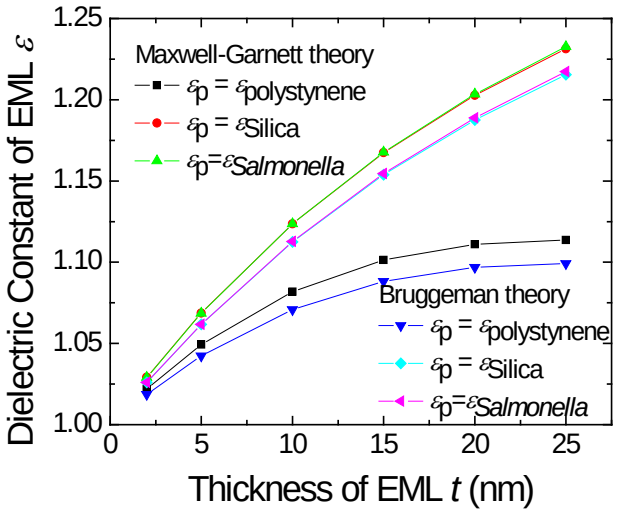

Figure 3.23 Dielectric constant of EML ε calculated from Maxwell-Garnett theory and Bruggeman theory.

One issue we should point out is that the effective medium theory used in this study. Maxwell Garnett theory has the limitation for the large volume ratio f_m.[158] Note that f_m increases with the increasing thickness of EML t, while f_m for polystyrene, Silica bead, *Salmonella* at t = 25 nm are only 0.0987, 0.2391, 0.2448, respectively. One can also use another popular effective medium (EM) theory, the Bruggeman theory, to estimate the effective dielectric constant ε:[28]

$$\varepsilon = \frac{1}{4}(\beta + \sqrt{\beta^2 + 8\varepsilon_p \varepsilon_a}), \quad (6)$$

$$\beta = (3f_p - 1)\varepsilon_p + [3(1 - f_p) - 1]\varepsilon_a . \quad (7)$$

Figure 3.23 shows the comparison of the dielectric constant ε as a function of t calculated by both EM theories. The ε calculated from Maxwell-Garnett theory is ~ 0.015 larger than that calculated from Bruggeman theory, which means the Maxwell-Garnett theory could overestimate the change of the dielectric constant. For the concerns we investigate here, this overestimated ε will guarantee the conclusion we have drawn above.

3.5 Conclusion

In conclusion, oblique angle deposition (OAD) was used to fabricate Ag and Au NPs films and the tunable localized surface plasmon resonances were achieved by simply changing the film thickness and the deposition angle.

We experimentally demonstrated that SPRW red shifted with the increasing particle size and the FWHM of the LSPR peak increased with the decreasing of θ at a fixed thickness d. At large deposition angle θ, both λ_p and $\Delta\lambda$ shift much slower with d and $\Delta\lambda$ is much narrower than those at small deposition angle. Compared with the normal deposited Ag island films, the Ag films fabricated by OAD at a large deposition angle have the advantage that the surface plasmon resonance wavelength (SPRW) will be finely tuned in the visible range. For example, the average SPRW λ_p increment is less than 3nm per 5 nm in film thickness at θ = 85°. The observed LSPR behaviors are consistent with the surface morphology and particle distribution of the Ag nanoparticle films. This deposition configuration provides an efficient way to fine tune the LSPR of Ag nanoparticle films.

While the size and roughness are very important to the optical properties of the Ag films, shape effects seem to be even more pronounced in the polarized optical absorption spectrum. Shadowing effect produced the elongated particles at $\theta \geq 75°$, which was verified by the polarized UV-Vis measurement. The polarized optical absorption presents a shift between the *p* polarized SPRW and the *s* polarized SPRW and the SPRW ratio increases with the increasing film thickness.

The response of the localized plasmon peak to the outer environment was also investigated by depositing Ti with different thickness or deposition angle onto Au NPs. At normal deposition ($\theta_{Ti} = 0°$), we estimated that the critical distance z_c for Au NPs in this study is 20 nm and the maximum plasmon peak shift $\Delta\lambda_p$ is around 100 nm. By fixing the thickness of Ti, we also found that the plasmon peak shifts less with a larger deposition angle θ_{Ti}, because the smaller coverage of Ti on Au NPs can only change a smaller part of the surrounding medium.

The sensor application of those Ag nanoparticle films has been explored using the Biotin/NeutrAvidin system. Though we found the Ag film could be oxidized in the aqueous solution with a blue shift of λ_p, a self assembled monolayer such as SSC or Biotin could be used to protect the Ag surface and a stable λ_p can be achieved. To our knowledge, this is the first report for the Ag nanoparticle oxidation in DI water in real-time study. We also showed that the Ag nanoparticle films based LSPR sensor can monitor the binding between Biotin and NeutrAvidin, and the limit of detection (LOD) is 10^{-10} M. The LOD of this LSPR sensor produced by the simple OAD method is comparable to the current LOD level reported in the literature[140, 159] and there is space left for further development. Although the results presented in this work are not optimized, the advantages of tunable LSPR-based sensors by OAD

method will open the possibilities of further developments in a wide range of chemical and biological applications.

Since Au is more stable than Ag in aqueous solutions, we fabricated Au NPs based LSPR sensor for *Salmonella* detection. In this sensor application, *Salmonella* bacteria, polystyrene spheres, and silica beads were coated onto the Au NP substrates, and the absorbance spectra before and after the coating were measured. According to the results, the plasmon peaks randomly blue- or red-shift and the peak shifts were less than 6 nm. By utilizing the Mie theory and effective medium theory, we constructed a simplified theoretical model and found that the plasmon peaks would theoretically shift 2-4 nm for the above samples, which was very close to the experimental results. Combining the considerations of the systematic error and the overestimated theoretical results, we believe that the detection ability of the LSPR sensor has a limitation for whole bacteria cells if using a conventional UV-Vis spectrometer.

CHAPTER 4

AG NANOROD MEDIATED SURFACE PLASMON RESONANCE SENSOR FOR *SALMONELLA* DETECTION

4.1 Introduction

As we know, the decay length (~ 200 nm) of the local electric field of SPR is longer than that (~ 20 nm) of LSPR [148], and the conventional SPR sensor has been applied for bacteria detection. However, by incorporating the nanostructure into the metal/environment interface, it could potentially increase the surface area which may enhance detection sensitivity. On the other hand, it also could alter the SPR curves and the SPR properties. So far, no one has performed such a study yet. In this chapter, a nanorod mediated SPR sensor was proposed and the influence of different structural parameters on its performance was firstly explored theoretically. We believed that the nanorods surface would provide more surface area for analyte adsorption thus increase the dynamic range; more importantly, the LSPs would be generated inside the nanorods under certain structural conditions therefore the SPR properties can be enhanced due to the interaction between LSPs and SPs. Experimental investigation was then performed by comparing Ag film and Ag nanorods/film structures, and the connections between theoretical and experimental results were discussed.

4.2 Effective medium theory based Ag nanorod mediated SPR sensor

4.2.1 Theoretical model and derivation

4.2.1.1 Ag nanorod mediated SPR sensor model

Figure 4.1(a) illustrates our model as a SPR sensory system with a Kretschmann attenuated total reflection configuration. Since we have incorporated an anisotropic nanorod layer into our sensing system, we consider a modified four-layer model with the structure of prism - metal film - nanorods - sensing layer: a glass prism (layer 1), a metal thin film with a thickness of d_f (layer 2), a layer of aligned nanorod array which has the same orientation with respect to the surface normal (layer 3), and a sensing layer which can be air or the target analyte (layer 4).

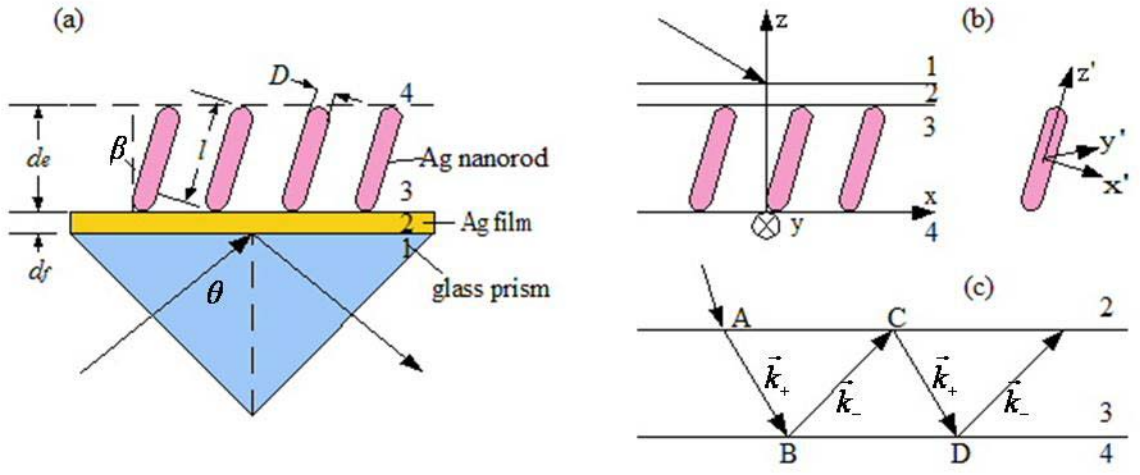

Figure 4.1 (a) A schematic of prism-metal film-nanorods-sensing layer model. (b) Incident plane and the plane defined by nanorods and normal direction of interface are all in the *xz* plane. The *x'*,*y'*,*z'* system has each axis parallel to one of the optical axes defined by the nanorod. (c) Multireflected ray in anisotropic nanorod layer.

We define that the effective medium layer with a thickness of d_e is composed of the nanorods and the voids between, and the voids have the same material as the sensing layer. The tilting angle, length of nanorod, and diameter of nanorod are β, l and D, respectively. A

monochromatic light beam containing wave vector $\vec{k}$ incidents on the interface between metal thin film and glass prism, and the reflectance *R* will be measured as a function of incident angle *θ*.

4.2.1.2 Fresnel equations

In typical SPR sensors, the reflectance versus incident angle of the monochromatic light are the fundamental data for analyzing signals caused by the refractive index changes. Kretschmann is the first to provide a theoretical equation of the SPR curve for prism - metal film - sensing layer structure by using three-layer Fresnel equations [160]. With the four-layer model in Figure 4.1(a), using three-layer Fresnel equations, we can obtain the general four-layer Fresnel equations and the reflectance *R* of the light relating to *p*-polarization can be derived as follows:

$$R = \left| r_{1234} \right|^2, \tag{4.1}$$

with

$$r_{1234} = \frac{r_{12} + r_{234} \exp(2ik_{2z}d_f)}{1 + r_{12}r_{234} \exp(2ik_{2z}d_f)}, \tag{4.2}$$

$$r_{234} = \frac{r_{23} + r_{34} \exp(2ik_{3z}d_e)}{1 + r_{23}r_{34} \exp(2ik_{3z}d_e)}, \tag{4.3}$$

$$r_{12} = \frac{k_{1z}\varepsilon_2 - k_{2z}\varepsilon_1}{k_{1z}\varepsilon_2 + k_{2z}\varepsilon_1}, \tag{4.4}$$

$$r_{23} = \frac{k_{2z}\varepsilon_3 - k_{3z}\varepsilon_2}{k_{2z}\varepsilon_3 + k_{3z}\varepsilon_2}, \tag{4.5}$$

$$r_{34} = \frac{k_{3z}\varepsilon_4 - k_{4z}\varepsilon_3}{k_{3z}\varepsilon_4 + k_{4z}\varepsilon_3}, \tag{4.6}$$

and

$$k_{jz} = \sqrt{\varepsilon_j \frac{\omega^2}{c^2} - k_x^2} \quad \text{for } j = 1, 2, 3, 4, \tag{4.7}$$

$$k_x = \sqrt{\varepsilon_1} \frac{\omega}{c} \sin\theta \ , \tag{4.8}$$

$$\omega = \frac{2\pi c}{\lambda} \ , \tag{4.9}$$

where r_{12}, r_{23} and r_{34} are the reflectance amplitude given by the Fresnel formula relating to *p*-polarization for adjacent layer interfaces; ε_j and k_{jz} are the dielectric constant and the wave vector component perpendicular to the interface in layer j (j = 1, 2, 3, 4); k_x is the component of the incident wave vector parallel to the interface and remains constant in each interface; ω and λ are the angular frequency and the wavelength of the incident light; c is the speed of light in vacuum.

Since we have introduced an anisotropic layer (layer 3) into this four-layer model, the dielectric constant ε_3 is a tensor, which makes the calculation of r_{23} and r_{34} complicated. Thus, we need to investigate the wave propagation in this anisotropic layer, determine the effective dielectric constant, and modify the four-layer Fresnel equations accordingly.

4.2.1.3 Wave propagation in anisotropic nanorod layer

Figure 4.1(b) shows a *p*-polarized light beam with wave vector $\vec{k}$ incidents onto the interface between glass prism (layer 1) and metal thin film (layer 2). The plane of incidence defined by the incident beam and surface normal of the interface is taken to be parallel to the plane defined by the direction of the tilted nanorods and surface normal of the interface, and is defined as *xz* plane, shown in Figure 4.1(b). Consequently, the components of the dielectric tensor ε_3 in the coordinate system *xyz* are all non-zero.

To simplify the representation of the tensor ε_3, we rotate the system *xyz* an angle of β around *y* axis and make each axis of the new system *x'y'z'* parallel to one of the principal axes defined by the nanorod, as shown in Figure 4.1(b). The dielectric constants in three principal axes, $\varepsilon_{x'}$, $\varepsilon_{y'}$, and $\varepsilon_{z'}$, only depend on the material and the shape of nanorods. For a cylindrical and spheroid shaped nanorod, the dielectric constant tensor

$$\varepsilon_3^{'} = \begin{pmatrix} \varepsilon_{x'} & 0 & 0 \\ 0 & \varepsilon_{y'} & 0 \\ 0 & 0 & \varepsilon_{z'} \end{pmatrix}, \tag{4.10}$$

and $\varepsilon_{x'} = \varepsilon_{y'}$. Thus, the dielectric constant tensor ε_3 in *xyz* coordinates can be written as:

$$\varepsilon_3 = \begin{pmatrix} \varepsilon_{xx} & \varepsilon_{xy} & \varepsilon_{xz} \\ \varepsilon_{yx} & \varepsilon_{yy} & \varepsilon_{yz} \\ \varepsilon_{zx} & \varepsilon_{zy} & \varepsilon_{zz} \end{pmatrix} = \begin{pmatrix} \varepsilon_{x'}\cos^2\beta + \varepsilon_{z'}\sin^2\beta & 0 & -\varepsilon_{x'}\sin\beta\cos\beta + \varepsilon_{z'}\sin\beta\cos\beta \\ 0 & \varepsilon_{y'} & 0 \\ -\varepsilon_{x'}\sin\beta\cos\beta + \varepsilon_{z'}\sin\beta\cos\beta & 0 & \varepsilon_{x'}\sin^2\beta + \varepsilon_{z'}\cos^2\beta \end{pmatrix} \tag{4.11}$$

Using Maxwell's equations, the wave vector k_{3z} propagating in the anisotropic layer and the effective dielectric constant of this layer in terms of k_{3z} can be derived and the equations are: [161-163]

$$k_{3z\pm} = \frac{-k_x\varepsilon_{xz} \pm \sqrt{\varepsilon_{x'}\varepsilon_{z'}}\sqrt{(\omega^2/c^2)\varepsilon_{zz} - k_x^2}}{\varepsilon_{zz}}, \tag{4.12}$$

$$\varepsilon_{3\pm} = \varepsilon_1\sin^2\theta + \left[\frac{-\sqrt{\varepsilon_1}\sin\theta\,\varepsilon_{xz} \pm \sqrt{\varepsilon_{x'}\varepsilon_{z'}}\sqrt{\varepsilon_{zz} - \varepsilon_1\sin^2\theta}}{\varepsilon_{zz}}\right]^2. \tag{4.13}$$

We note that the wave vector k_{3z} has two solutions, which reveals that the phenomenon of nonsymmetrical reflection occurs when the wave propagates from an anisotropic to an isotropic medium. This behavior has been reported by Jen and Lee. [164] The solution k_{3z+} corresponds to the reflected ray in an backward direction, $\bar{k}_+ = k_x\hat{x} + k_{3z+}\hat{z}$, whereas the solution k_{3z-}

corresponds to the reflected ray in a forward direction, $\bar{k}_{-} = k_x\hat{x} + k_{3z-}\hat{z}$, as illustrated in Figure 4.1 (c). [164]

Considering the nonsymmetrical reflection, we re-derive the reflectivity and transmittance coefficients for the interfaces between the anisotropic layer and the isotropic layer, and finally obtain the modified Fresnel equations as follows:

$$r_{234} = r_{23A} + \frac{t_{23A} r_{34B} t_{32C} \exp[i(k_{3z+} - k_{3z-})d_e]}{1 - r_{32C} r_{34B} \exp[i(k_{3z+} - k_{3z-})d_e]}, \tag{4.14}$$

with

$$r_{23A} = \frac{k_{2z}\varepsilon_{3+} - k_{3z+}\varepsilon_2}{k_{2z}\varepsilon_{3+} + k_{3z+}\varepsilon_2}, \tag{4.15}$$

$$t_{23A} = \frac{\sqrt{\varepsilon_{3+}}}{\sqrt{\varepsilon_2}} \frac{2k_{2z}\varepsilon_2}{k_{2z}\varepsilon_{3+} + k_{3z+}\varepsilon_2}, \tag{4.16}$$

$$r_{34B} = \frac{\sqrt{\varepsilon_{3-}}}{\sqrt{\varepsilon_{3+}}} \frac{k_{3z+}\varepsilon_4 - k_{4z}\varepsilon_{3+}}{k_{3z-}\varepsilon_4 + k_{4z}\varepsilon_{3-}}, \tag{4.17}$$

$$r_{32C} = \frac{\sqrt{\varepsilon_{3+}}}{\sqrt{\varepsilon_{3-}}} \frac{k_{3z-}\varepsilon_2 - k_{2z}\varepsilon_{3-}}{k_{3z+}\varepsilon_2 + k_{2z}\varepsilon_{3+}}, \tag{4.18}$$

$$t_{32C} = \frac{\sqrt{\varepsilon_2}}{\sqrt{\varepsilon_{3-}}} \frac{k_{3z-}\varepsilon_{3+} + k_{3z+}\varepsilon_{3-}}{k_{3z+}\varepsilon_2 + k_{2z}\varepsilon_{3+}}. \tag{4.19}$$

The detailed derivation of equations (4.12) - (4.14) has been listed in Appendix C.

4.2.1.4 Effective Medium Theory

Now the problem is reduced to the calculation of effective dielectric constants along three principal axes $\varepsilon_{x'}$, $\varepsilon_{y'}$, and $\varepsilon_{z'}$. This can be accomplished by means of effective medium theory

(Appendix B). In this study, we take the metal as the host thus the MG theory is used, which yields [162, 165]

$$\frac{\varepsilon_i - \varepsilon_m}{\varepsilon_m + L_i(\varepsilon_i - \varepsilon_m)} = (1 - f_m)[\frac{\varepsilon_s - \varepsilon_m}{\varepsilon_m + L_i(\varepsilon_s - \varepsilon_m)}] \text{ for } i = x', y', z', \tag{4.20}$$

where ε_m and ε_s are the dielectric constants of metal and sensing material, respectively; f_m is the volume fraction of metal; L_i are the depolarization factor. In this paper, we consider three kinds of shape of the nanorod: prolate spheroid, oblate spheroid and sphere. The corresponding depolarization factor L_i can be calculated as follows: [58]

$$L_{z'} = \frac{1-e^2}{e^2}[\frac{1}{2e}\ln(\frac{1+e}{1-e}) - 1], \tag{4.21}$$

$$e = \sqrt{1-r^2} \text{ (prolate spheroid)}, \tag{4.22}$$

$$L_{z'} = \frac{g}{2e^2}(\frac{\pi}{2} - \tan^{-1} g) - \frac{g^2}{2}, \tag{4.23}$$

$$g = \sqrt{\frac{1-e^2}{e^2}} \text{ (oblate spheroid)}, \tag{4.24}$$

$$L_{z'} = \frac{1}{3} \text{ (sphere)}, \tag{4.25}$$

$$L_{x'} = L_{y'} = \frac{1}{2}(1 - L_{z'}), \tag{4.26}$$

where r is the aspect ratio of the nanorod.

4.2.1.5 Parameters for Numerical Calculation

To determine the dielectric constant of the Ag layer ε_2, as well as the effective dielectric constant ε_3, Drude model is used as [160]

$$\varepsilon_2 = \varepsilon_2^{\infty} - \frac{\omega_p^2}{\omega(\omega + i\omega_\tau)}, \tag{4.27}$$

where ω_p and ω_τ are the plasma frequency and the damping frequency, respectively; ε_2^{∞} is the background frequency of the metal at a frequency of infinity. Those parameters are: $\varepsilon_2^{\infty} = 2.48$, $\omega_p = 1.35 \times 10^{16}$ rad/s and $\omega_\tau = 7.62 \times 10^{13}$ rad/s for Ag. [166] In our calculation, other constants are determined as follows: the refractive indices of air and glass prism are 1 and 1.51, respectively; the wavelength of the incident light λ = 632.8 nm; the speed of light $c = 3\times10^8$ m/s.

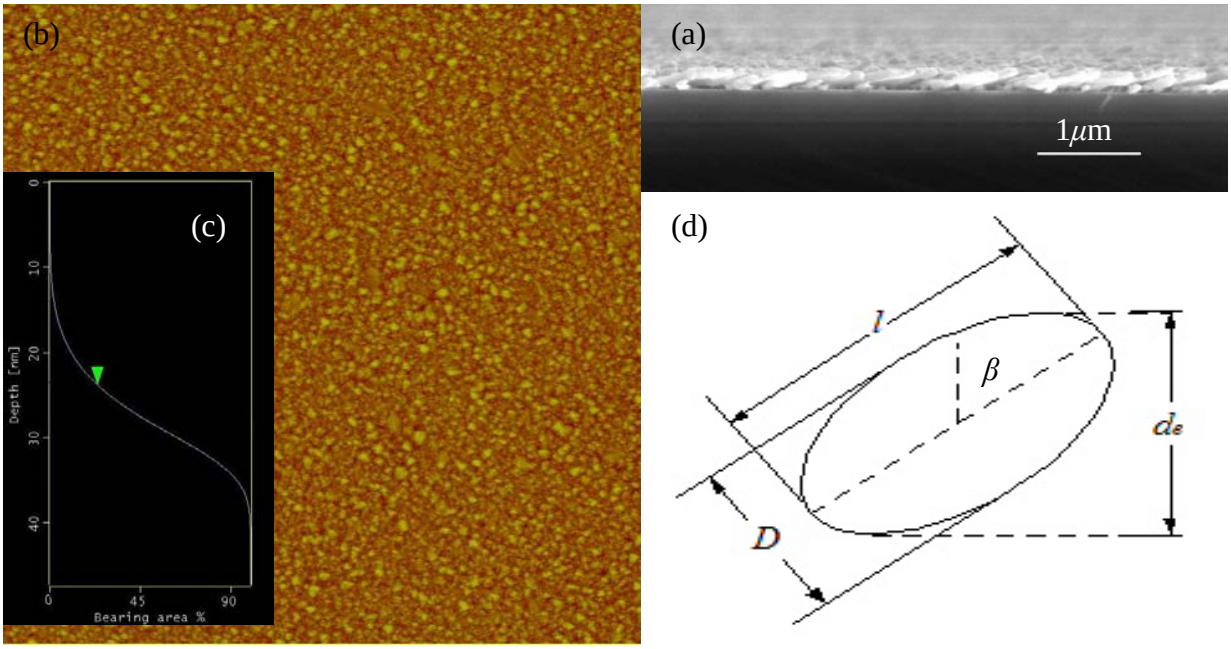

Figure 4.2 (a) Representative SEM image of the cross section of Ag nanorods fabricated by OAD. (b) Representative AFM image of the Ag nanorods fabricated by OAD. (c) Bearing curve of the AFM image. (d) Geometry relationship between effective layer thickness d_e and tilting angle β, length of nanorod l, diameter of nanorod D.

As we can see, to calculate the reflectance R, we need six structural parameters: tilting angle β, volume fraction of metal f_m, thickness of the effective medium layer d_e, thickness of the film d_f, diameter of nanorod D and length of nanorod l. First, from previous SPR experiment results (not shown), we have known that the thickness of the film d_f plays a significant role in

SPR properties. Second, during OAD deposition, by changing the vapor incident angle, deposition rate and film thickness, we can control the tilting angle β, volume fraction of metal f_m, diameter of nanorod D and length of nanorod l.

For most of our experiments reported thus far, we fix the vapor incident angle as 86°, thus the tilting angle β and volume fraction of metal f_m are fixed. Figure 4.2(a) is a representative scanning electron microscopy (SEM) (FEI Inspect F) image of the cross section of Ag nanorods fabricated by OAD. The tilting angle can be measured by ImageTool and the statistically averaged β is 73°. [167] Figure 4.2(b) shows atomic force microscopy (AFM) (Veeco Dimension 3100) image of the Ag nanorods and the scan size is 1 μm × 1 μm. The bearing analysis can reveal how much of a surface lies above or below a given height by giving the depth, which is the difference between the tallest point and the measured point in Figure 4.2(c). The ratio between area under the bearing curve and whole area will be f_m, which has been calculated as 0.4. Therefore, we will fix β = 73° and f_m = 0.4 in our calculation. Since we have assumed that the nanorod has a shape of spheroid, the thickness of the effective medium layer d_e is determined by tilting angle β, diameter D and length l of nanorod as shown in Figure 4.2(d). A simple geometry calculation can be accomplished as follows:

$$d_e = \frac{2}{B}(Ax + \frac{Dl}{4}\sqrt{B - x^2}), \tag{4.28}$$

where

$$A = \frac{1}{4}(l^2 - D^2)\sin\beta\cos\beta, \tag{4.29}$$

$$B = \frac{1}{4}(D^2\cos^2\beta + l^2\sin^2\beta), \tag{4.30}$$

$$x = A\sqrt{\frac{B}{A^2 + \frac{D^2 l^2}{16}}}. \tag{4.31}$$

To investigate how the other structural parameters such as thickness of the film d_f, diameter of nanorod D, and length of nanorod l, influence the SPR properties, we carry out the calculation by varying these parameters in the following range: d_f = 30, 40, 50 nm; D = 5, 10, 30, 50, 70, 100 nm; l = 10, 20, 40, 60, 80, 100, 150, 200 nm. All the calculations are performed by Matlab 6.1.

4.2.2 Optical properties of Ag nanorod mediated SPR sensor

A set of typical SPR curves (d_f = 40 nm, D = 30 nm) for different length of nanorods calculated by this effective medium theory based four-layer model are shown in Figure 4.3. In general, the SPR curve can be characterized by three parameters: reflectance minimum at resonance R_m, SPR resonance angle θ_r, which is defined as the angle associated with the reflectance minimum, and width w at the half of the dip height. Figure 4.3(a) shows that the SPR curves corresponding to the refractive index of sensing layer n = 1.00. As we can see, when length of nanorod increases from l = 10 nm to l = 20 nm, the reflectance minimum R_m and width w decrease while the SPR resonance angle θ_r red shifts. With further increase of length l, the reflectance minimum R_m and the width w increase while the SPR resonance angle θ_r blue shifts. When l = 200 nm, the SPR dip becomes inconspicuous. Figure 4.3(b) shows the SPR curves generated with the same structure but the surrounding refractive index changes from n = 1.00 to n = 1.33 (water). Obviously, all SPR angles red shift with an increasing reflectance minimum and a broadened width.

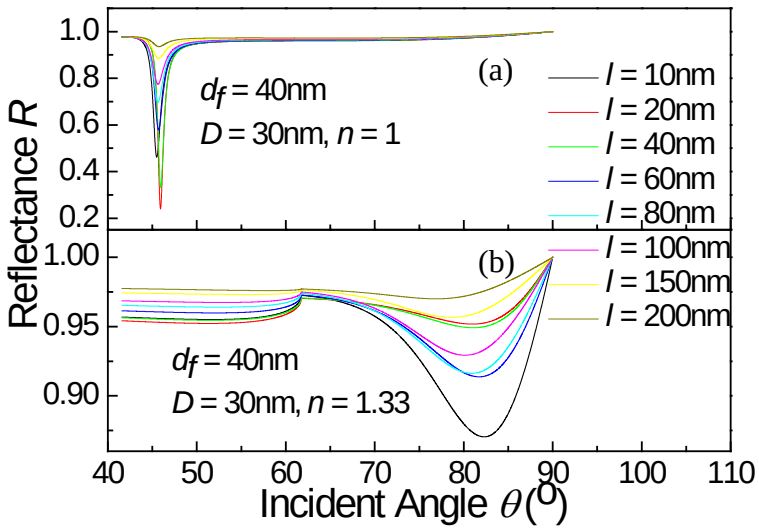

Figure 4.3 (a) Typical nanorod mediated SPR curves with d_f = 40 nm, D = 30 nm at (a) n = 1.00 and (b) n = 1.33.

For a detailed comparison of SPR curves in air (n = 1.00) and in water (n = 1.33), we summarize the reflectance minimum R_m, SPR resonance angle θ_r and width w of the nanorod mediated SPR curves with film thickness d_f = 40 nm as a function of length of nanorod l in Figure 4.4. In air (Figure 4.4(a)), reflectance minimum R_m increases with increasing diameter of nanorod D at fixed length of nanorod l as shown in Figure 4.4(a). For different diameter of nanorod D, R_m first decreases until the aspect ratio r approaches 1 and then begins to increase. Figure 4.4(b) shows that SPR angle θ_r behaviors differently at different diameter of nanorod D and varies in the range between 43.5° and 48.5°. At D = 5 nm, θ_r increases with increasing l; at D = 10 nm, θ_r decreases first and then increases with increasing l; at D > 10 nm, θ_r reaches maximum as the aspect ratio r approaches 1 and at which point it begins to decrease. The SPR width w almost overlaps at D = 5 and 10 nm, and it increases with increasing l as shown in Figure 4.4(c). The trend becomes different at D > 10 nm, and the w - l behavior has almost the opposite trend compared to the θ_r - l relation: w decreases first until aspect ratio is close to 1 and

then increases with increasing l. The minimum width w for different D is ranging from 0.5° to 0.75°.

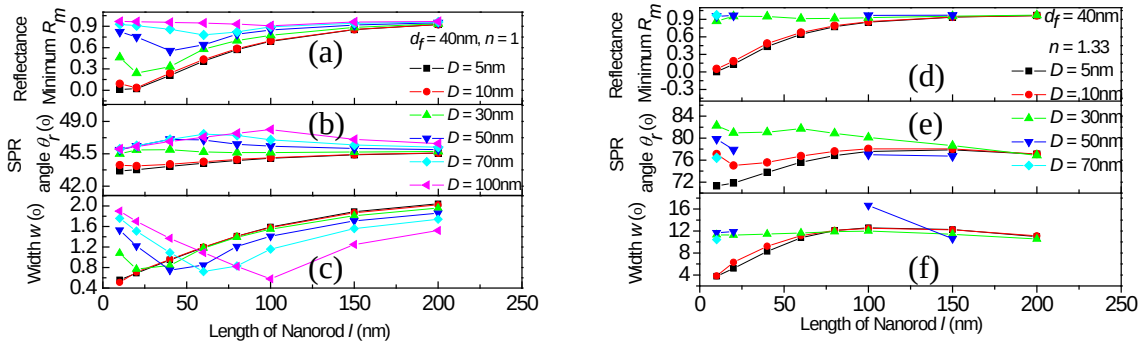

Figure 4.4 (a) Reflectance minimum R_m, (b) SPR angle θ_r and (c) SPR curve width w as a function of length of nanorod l at n = 1.00. (d) Reflectance minimum R_m, (e) SPR angle θ_r and (f) SPR curve width w as a function of length of nanorod l at n = 1.33.

In water, SPR signal can not be obtained under the following conditions: D = 50 nm and l = 40, 60, 80, 120 nm; D = 70 nm and l > 10 nm; D = 100 nm. Figure 4.4(d) shows reflectance minimum R_m obtained under specific conditions for water. It increases with increasing length of nanorod l at D = 5 and 10 nm and is close to 1 at D > 10 nm. The SPR angle θ_r shifts to a larger angle ranging from 71° to 82.5° when the surrounding dielectric constant increases to n = 1.33 (Figure 4.4(e)). At D = 5 and 10 nm, θ_r remains the same trend as that in air except that θ decreases slightly at l > 150 nm. At D = 30 nm, θ_r locates its maximum at smallest length of nanorod (l = 10 nm) and then decreases with increasing length of nanorod l except for a peak at l = 60 nm. There is an overall trend that θ_r converges for different diameter of nanorod D at a large length of nanorod l (l = 200 nm). Figure 4.4(f) shows that width w becomes apparently broad in water as we observe in Figure 4.3(b). At D = 5 and 10nm, w has a minimum about 4° at l = 10 nm and then quickly increases to 12° at l = 100 nm. After that, it decreases slightly with l. At D = 30 nm, w is around 11° and has a slightly higher value at l = 100 nm. At D > 30 nm, w is

randomly distributed and larger than 10°. From the above discussion, we find that most configurations of the nanorods mediated SPR structure at D > 30 nm will lose the SPR signal in water. Therefore, the discussion will be focused on D = 5, 10, 30 nm in the following parts, since for the real applications, most sensing processes will be performed in the aqueous solutions.

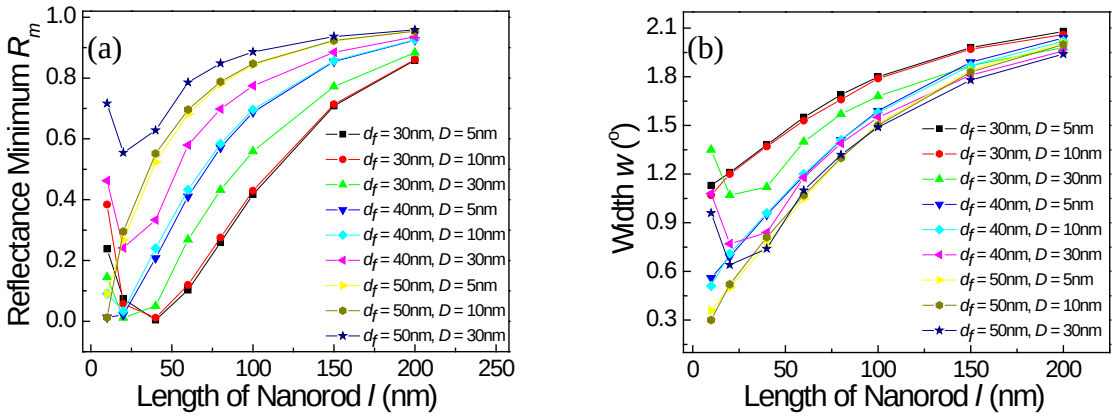

Figure 4.5 (a) Reflectance minimum R_m, (b) SPR curve width w as a function of length of nanorod l at different film thickness d_f = 30, 40, 50 nm and diameter of nanorod D = 5, 10, 30 nm.

Practically, small reflectance minimum R_m and narrow width w are desirable for sensing applications while the thickness of the thin metal film d_f plays a vital role in determining these two parameters. To find out how reflectance minimum R_m and width w change with film thickness d_f, we plot them as a function of length of nanorod l for d_f = 30, 40, 50 nm at n = 1.00 in Figure 4.5. According to Figure 4.5(a), at D = 5 and 10nm, when d_f = 30 nm, R_m reaches a minimum at l = 40 nm; when d_f = 40 nm, R_m has a minimum at l = 20 nm; when d_f = 50 nm, R_m does not have a minimum, and increases with increasing l monotonically. The general trend is that smaller d_f has its minimum R_m at larger l. At D = 30 nm, R_m has the minimum located at l = 20 nm for all film thickness d_f. Figure 4.5(b) shows that the trends of width w stay the same when the film thickness d_f changes to d_f = 30 and 50 nm, as described in Figure 4.4(e). One

should note that the width w decreases with increasing d_f for fixed diameter D and length l of the nanorod. In other words, by changing the film thickness d_f, we find that reflectance minimum R_m and width w have a trade-off relationship; i.e., a small reflectance minimum R_m can be obtained at the expense of a large width w.

4.2.3 Dynamic range and sensitivity enhancement of Ag nanorod mediated SPR sensor

We have thus far discussed the effect of nanorod length, nanorod diameter and film thickness on SPR curves by inspecting its reflectance minimum R_m and width w at a specific refractive index n = 1.00. For chemical or biological sensors, we are more interested in how the SPR signal, i.e. the position of SPR angle θ_r, shifts with the change of refractive index n. There are two important parameters associated with sensing: the dynamic range and the sensitivity. First we calculate the dynamic range, which is defined as the detectable refractive index change, by plotting the SPR angle θ_r as a function of refractive index n, for d_f = 30, 40, 50 nm from n = 1.00 to n = 1.34. Since their dynamic ranges have the same trends, the discussion will focus on the structure with d_f = 40 nm. Figures 4.6(a)-6(c) compare the dynamic ranges for different lengths of nanorod l at D = 5, 10, 30 nm, respectively. As shown in Figure 4.6(a), SPR angle θ_r red shifts with increasing length of nanorod l at the fixed refractive index n. More interestingly, at a fixed l, SPR angle θ not only red shifts, but also has an increasing slope, which is defined as the local sensitivity s of the SPR sensor $s = \frac{d\theta_r}{dn}$, with increasing n. This means that this nanorod mediated SRP structure has an increasing sensitivity s when the refractive index n increases. Figure 4.6(b) shows a similar trend except in the case of D = 10 nm, l = 10 nm, which corresponds to the spheres with a diameter of 10 nm. In this case, SPR angle θ_r is overlapped with that of the structure D = 10nm, l = 40nm at n < 1.25. With further increasing of refractive

index n, the sensitivity increases rapidly. At D = 30 nm (Figure 4.6(c)), the phenomenon becomes more interesting. First, at l = 20 and 40 nm, i.e. as the aspect ratio $r \rightarrow 1$, the SPR angle θ_r red shifts and the slope increases with increasing refractive index n when $n \leq 1.30$. From n = 1.30 to n = 1.34, SPR angle θ_r blue shifts with n, thus the slope suddenly becomes negative. In other cases, for l = 10, 60, 80 nm, SPR angle θ_r red shifts and the slope increases with refractive index n when $n \leq 1.32$. With further increasing of the refractive index n, θ_r slightly red shifts or blue shifts, which means it becomes more difficult to differentiate SPR angle shift due to the change of refractive index n. Figure 4.6(d) shows a typical comparison for different diameter of nanorod D at a fixed length of nanorod l = 20 nm. As we can see, SPR angle θ_r and the sensitivity s increases with increasing D at a fixed refractive index n except that θ begins to blue shift when $n \geq 1.30$ at D = 30 nm.

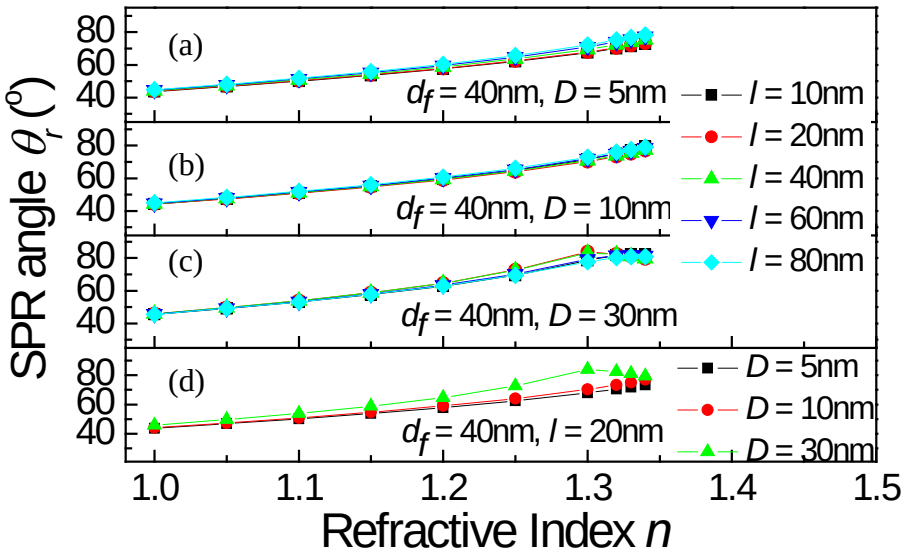

Figure 4.6 Dynamic range of nanorod mediated SPR sensor with d_f = 40nm at fixed diameter of nanorod (a) D = 5 nm, (b) D = 10 nm, (c) D = 30 nm. (d) Typical dynamic range at a fixed length of nanorod l = 20 nm.

In real SPR sensor applications, we are more concerned about the local sensitivity *s* around some certain refractive index *n*. In other words, how much is the smallest amount of analyte we can measure when the refractive index *n* is only changed in a very small range. We still take the structure with d_f = 40 nm as an example and consider the sensitivity *s* when the refractive index *n* changes from *n* = 1.00 to *n* = 1.05 (in air) and from *n* = 1.30 to *n* = 1.34 (in water), as shown in Figures 4.7(a) and 4.7(b), respectively. From *n* = 1.00 to *n* = 1.05, the sensitivity *s* increases with increasing diameter of nanorod *D* at fixed length of nanorod *l* but it changes differently with *l* when D is fixed (Figure 4.7(a)): at *D* = 5 nm, *s* increases with increasing length of nanorod *l* monotonically; at *D* = 10 nm, *s* first decreases to its minimum at *l* = 20 nm and then increases with *l*; at *D* = 30 nm, *s* is much larger than that at *D* = 5 and 10 nm and it reaches its maximum around $r \rightarrow 1$ before it decreases with *l*. From *n* = 1.30 to *n* = 1.34 (Figure 4.7(b)), at *D* = 5 and 10 nm, *s* shows the similar trends as from *n* = 1.00 to *n* = 1.05 and is higher than that at *D* = 30 nm. Corresponding to the negative slope described in Figure 4.6(c), at *D* = 30 nm, the sensitivity *s* becomes negative around $r \rightarrow 1$ though the absolute value is larger than those when $r > 1$ or $r < 1$.

(a)

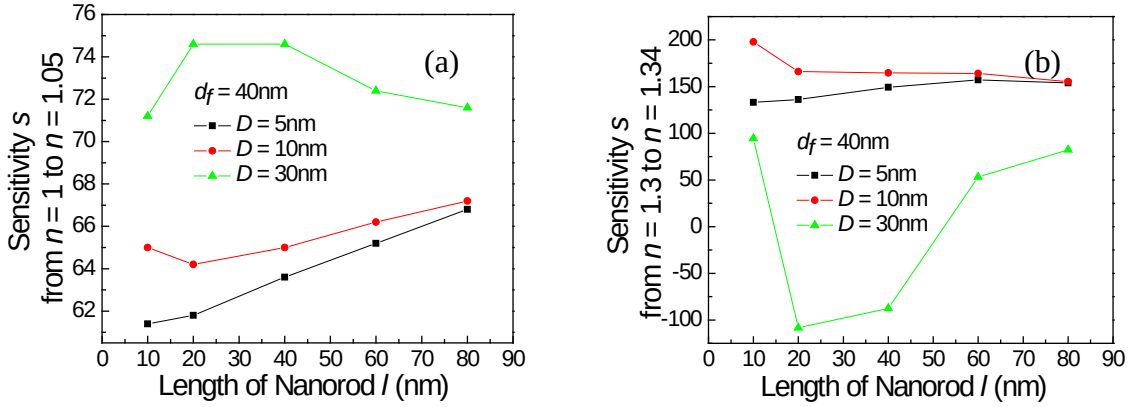

Figure 4.7 Sensitivity *s* of nanorod mediated SPR sensor with d_f = 40 nm and *D* = 5, 10, 30 nm (a) from *n* = 1.00 to *n* = 1.05 and (b) from *n* = 1.30 to *n* = 1.34.

When we are dealing with the SPR curves generated by the theoretical model, we have no difficulties recognizing the SPR signal even if the reflectance minimum is close to 1. However, in the real measurements, we need to consider the signal-to-noise ratio and the significance of the SPR dip, thus we set a reasonable threshold for R_m and require $R_m < 0.6$ as a valid SPR signal for the following sensitivity comparison.

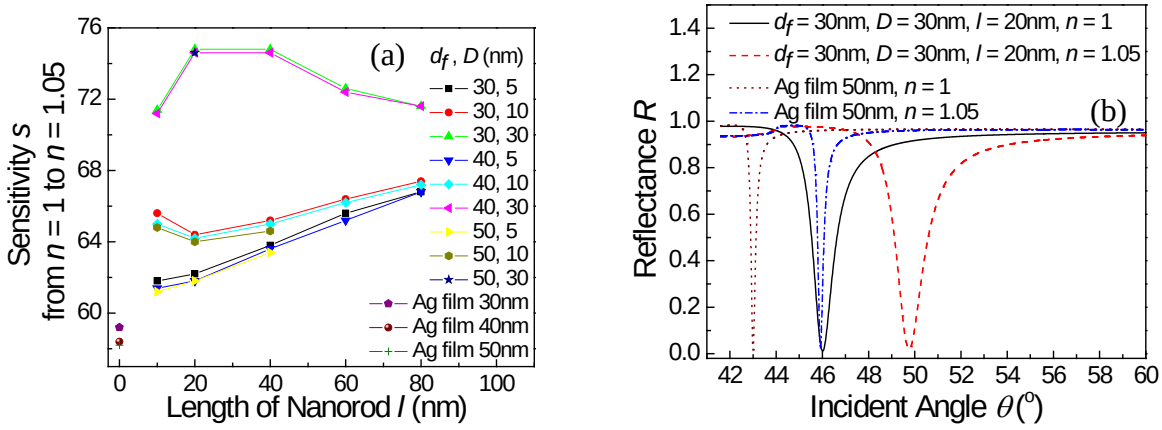

Figure 4.8 (a) Sensitivity comparison between nanorod mediated SPR sensor and conventional SPR sensor, and (b) the corresponding SPR curves from n = 1.00 to n = 1.05.

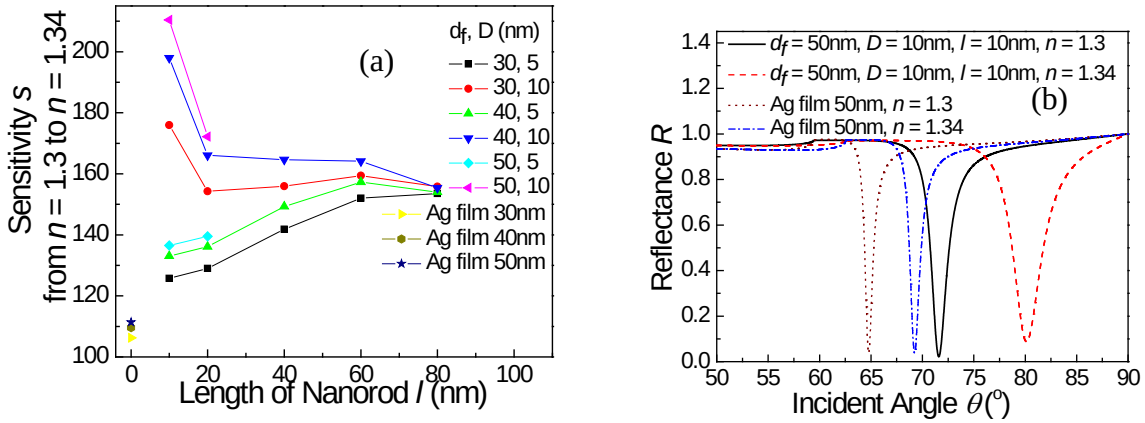

Figure 4.9 (a) Sensitivity comparison between nanorod mediated SPR sensor and conventional SPR sensor, and (b) the corresponding SPR curves from n = 1.30 to n = 1.34.

To see the enhancement by incorporating the nanorod structure into SPR configuration, we compare the sensitivity *s* between the nanorod mediated SPR configurations with d_f = 30, 40, 50 nm, D = 5, 10, 30 nm and the conventional SPR configurations composed of Ag film with thickness of 30, 40, 50 nm as shown in Figures 4.8-4.9. The sensitivity *s* calculated when the refractive index *n* changes from n = 1 to n = 1.05 is plotted in Figure 4.8(a). First, sensitivity behaviors are similar as film thickness changes from d_f = 40 nm to d_f = 30, 50 nm. Second, sensitivity *s* of the nanorod mediated SPR configurations is higher than that of the conventional Ag film SPR configuration. In this case, the best configuration is the nanostructure with d_f = 30 nm, D = 30 nm and l = 20 nm. Since the sensitivities for all the conventional SPR configurations are very close, we take the most commercially used film structure with 50nm thickness as a comparison with the best nanostructure, and their SPR curves are plotted in Figure 4.8(b). From n = 1 to n = 1.05, SPR angle θ_r shifts 2.91° for film structure while 3.74° for nanostructure, though the width increases in the case of nanostructure. It has been reported that the broadening in SPR curve is caused by the excited LSPs, which involve a large number of damping modes and the decreased effective mean free path of conduction electrons. [58, 77] From n = 1.3 to n = 1.34, the negative values of the sensitivity are filtered out due to the large R_m and the data is plotted in Figure 4.9(a). The configuration with the highest *s* is the nanostructure with d_f = 50 nm, D = 10 nm and l = 10 nm, which corresponds to the spheres with diameter of 10 nm. It is compared with 50 nm film structure in Figure 4.9(b) and the SPR dips indicate a shift of 4.47° for film structure while 8.54° for nanostructure. The enhancement is almost two-fold at the expense of broadened width. In a word, the optimal nanorod mediated SPR configuration depends on the changing range of refractive index, and the large enhancement of sensitivity will be obtained when the targeting analyte is associated with a large refractive index.

4.3 Experimental investigation of Ag nanorod mediated SPR sensor

In order to validate the theory, we have performed some prelimilary SPR experiments on Ag nanorods/Ag film substrates.

4.3.1 SPR setup

In the experiments, we fix the incident light wavelength at 632.8 nm, scan the incident angle onto the sample and collect the reflected light by a line camera. The optical path is shown in Figure 4.10.

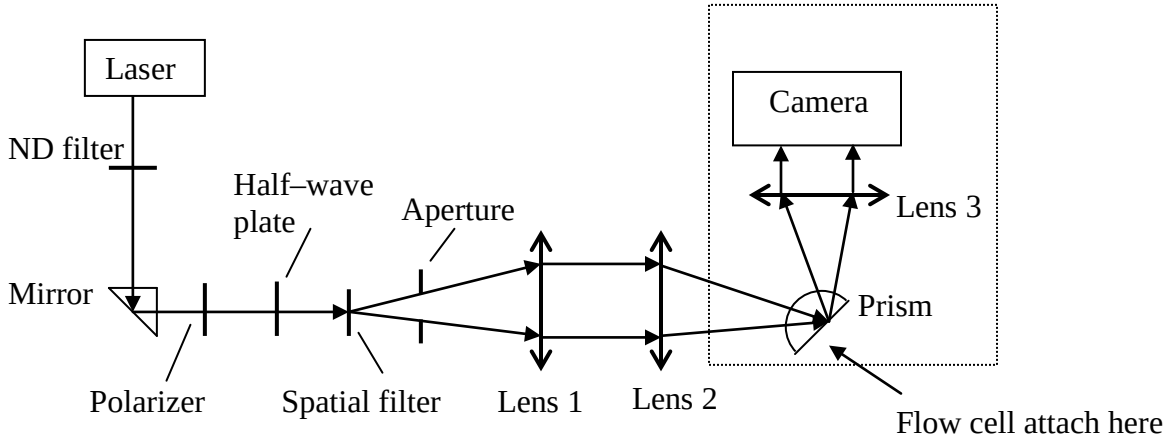

Figure 4.10 Optical path of SPR sensor.

The incident light beam first goes through a neutral density (ND) filter, then is reflected from a mirror and goes into a polarizer. We have mentioned in section 1.2.2.2 that only *p*-polarized light will interact with the interface between the prism and the metal, therefore the polarizer will turn the incident light into *p*-polarized light. Since *s*-polarized light is treated as the background, a ½ λ waveplate is placed behind the polarizer so that the *p*-polarization state and *s*-polarization state can be easily switched. To filter out the spatially varying "noise" intensity of the input Gaussian beam, a space filter is used, which contains an aspheric lens and a 10 μm

pinhole. When the input beam is focused by the aspheric lens, it is transformed into a uniform Gaussian spot (on the optical axis) with side fringes that represent the unwanted noise. By centering a pinhole on the central Gaussian spot, the clean portion of the beam can pass while the noise fringes are blocked. And then the beam goes through the aperture, lens 1 and lens 2, and incidents onto a semi-cylindrical prism. Though the incident beam has a shape of cone, which contains a small range of incident angles onto the backside of the prism, the subtle bending at the curve surface of the prism will be ignored. The sample is attached on the backside of the prism, and the reflected beam goes through lens 3 and enters a line camera.

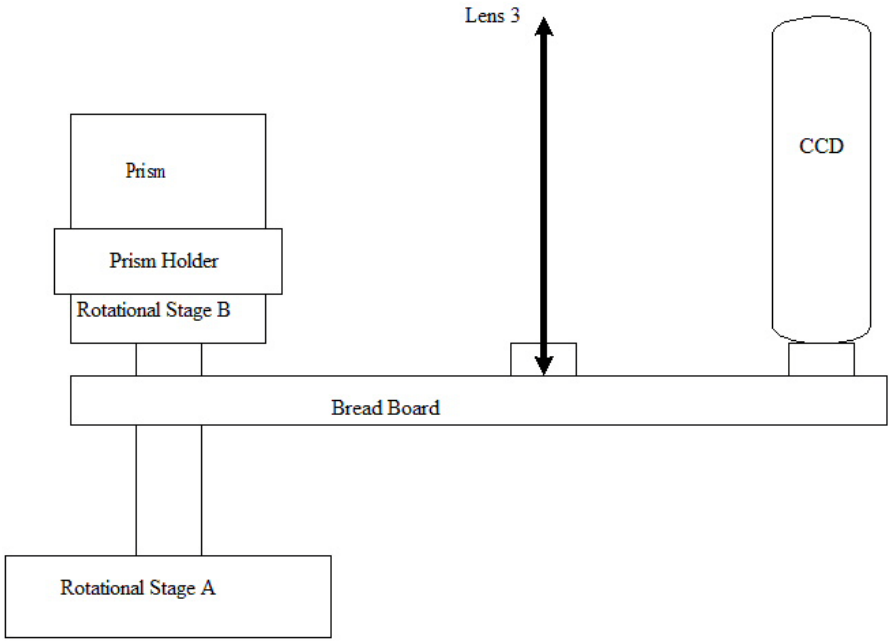

Figure 4.11 Side view of the dashed part in Figure 4.10.

As described above, the incident beam cone only contains a small range of the incident angles, which means we need rotate the sample and the line camera to look for the SPR resonance angle when necessary. Figure 4.11 is the side view of the dashed part in Figure 4.10. The connections between these optical components are: the prism holder is fixed on the rotational stage B; the rotational stage B, lens 3 and line camera (CCD) are fixed on a small

bread board; the bread board is fixed on the rotational stage A. Therefore, if rotate the stage A, the prism, lens 3 and CCD will rotate simultaneously; if rotate the stage B, only the prism will rotate.

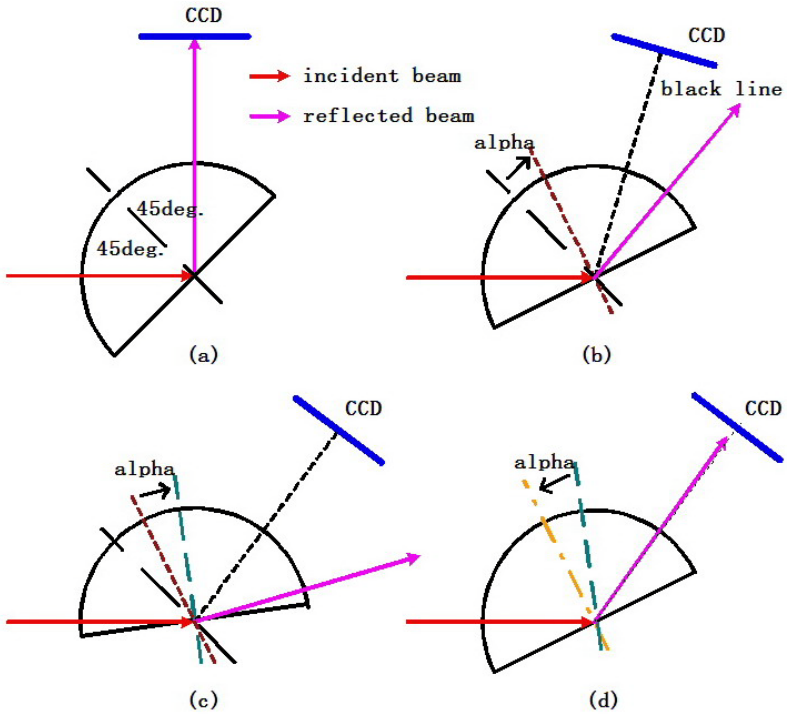

Figure 4.12 Illustration of measurement method.

In the beginning of the measurement, the central beam has an incident angle of θ = 45°, and the central reflected beam is perpendicular to the surface of the CCD, as shown in Figure 4.12(a). When SPR occurs, the energy of the incident beam will be absorbed by the oscillating electrons in the metal, which corresponds to a black line in the reflected beam spot. To find the black line, rotate the stage A and hold a piece of white paper to follow the reflected beam until the black line is in the center of the reflected beam spot. If the stage A rotates an angle of α, the incident angle will change α while the reflected angle will change 2α. Thus, the central beam has an incident angle of $\theta = 45° + \alpha$ (Figure 4.12(b)), the normal line of CCD surface rotates an angle of α, and the reflected beam deviates the normal line of CCD surface an angle of α. The

next steps are to move the black line to the center of CCD. To do so, first continue to rotate the stage A an angle of α, which makes the reflected beam deviates the normal line of CCD surface an angle of 2α (Figure 4.12(c)); then rotate the stage B an angle of $-\alpha$, which will bring the prism back to the position in Figure 4.12(b) and the reflected beam back to the normal direction of CCD surface (Figure 4.12(d)).

4.3.2 Ag nanorods/Ag film fabrication

Ag film or Ag nanorods were fabricated by OAD at a deposition angle $\theta = 0°$ or 86° using the custom-designed electron-beam evaporation system (Torr International, Inc.). The background pressure in the chamber was 1×10^{-6} Torr, and the deposition rate was approximately 0.8-1.0 Å/s.

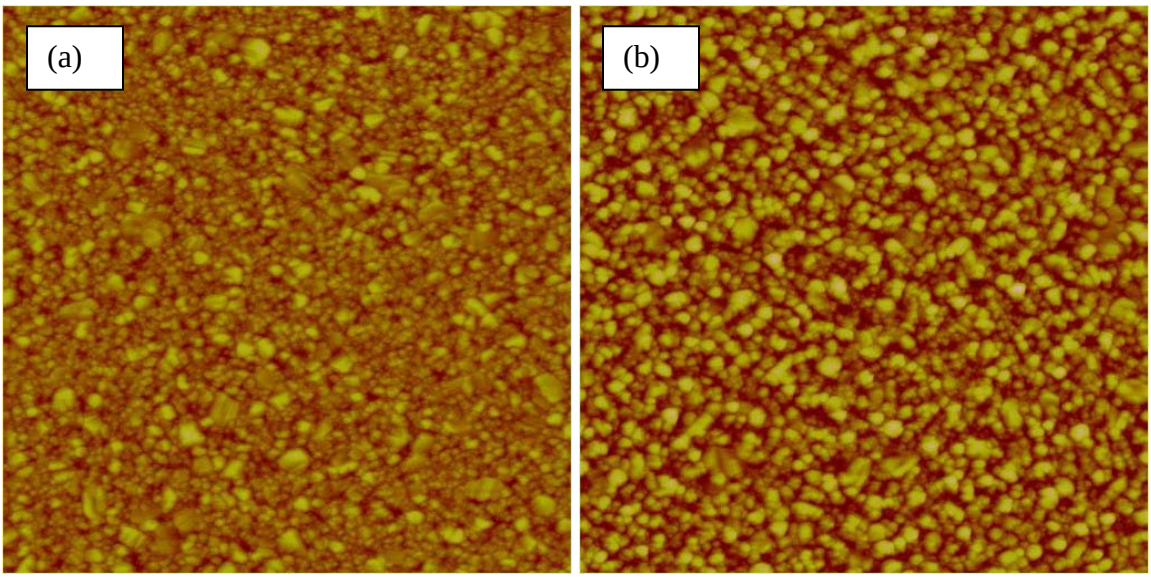

Figure 4.13 AFM images of (a) Ag film 40 nm and (b) Ag nanorods 200 nm on Ag film 40 nm. The thickness is the QCM reading and the scan size is 5 μm ×5 μm.

The morphologies of Ag film 40 nm and Ag nanorods 200 nm on Ag film 40 nm were examined by AFM, as shown in Figure 4.13. As we know, the actual thin film does not have a

perfectly smooth surface. Instead, the thin film surface has a roughness around 3 nm (Figure 4.13(a)). For the Ag nanorods/film sample, since the AFM tip can not go into the gap between the tilted nanorods, we only can see many islands with a mean diameter of 100 nm on the surface and the roughness increases to 7-8 nm (Figure 4.13(b)).

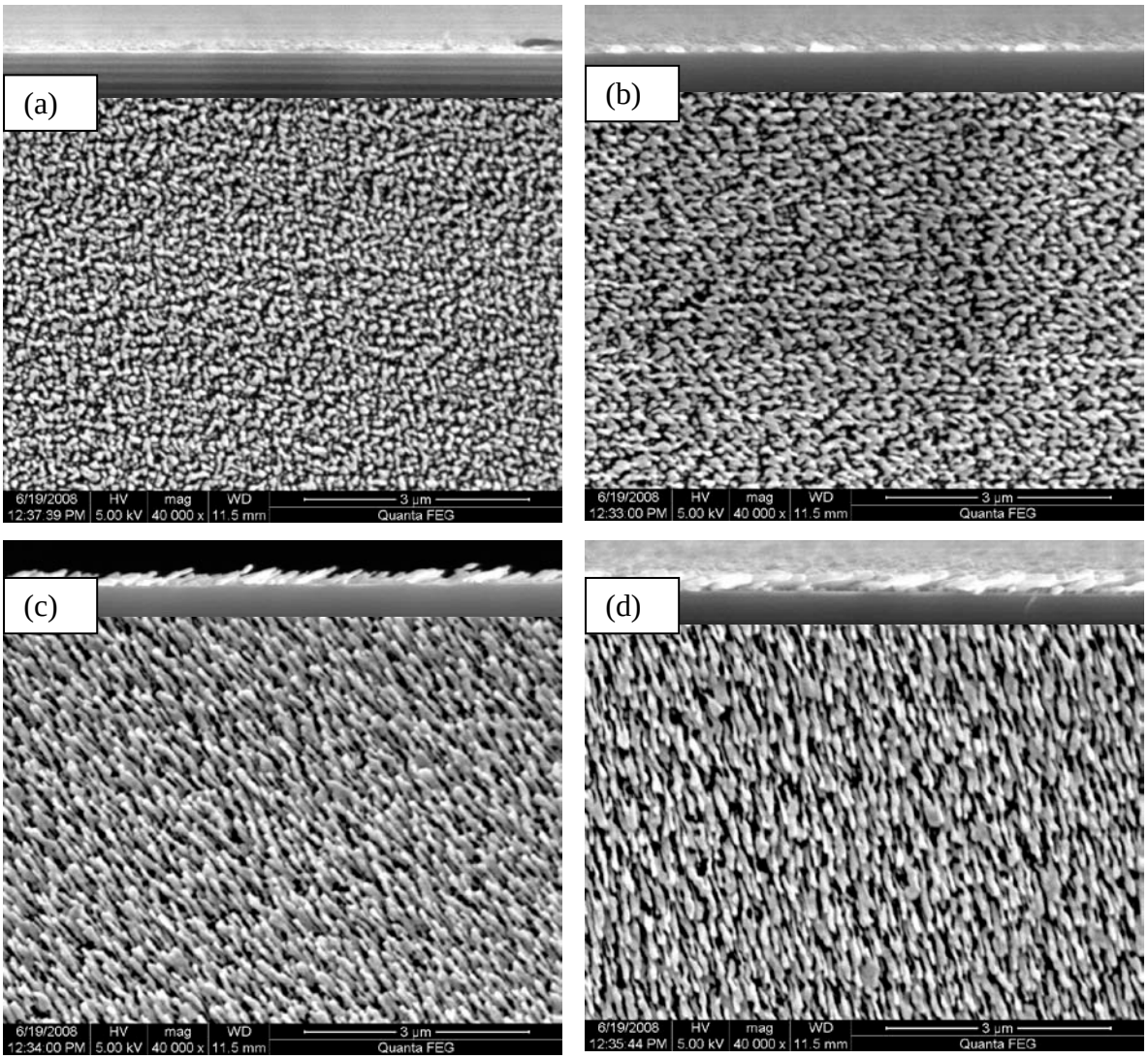

Figure 4.14 SEM top views of Ag nanorods with a nominal thickness of (a) 200 nm; (b) 300 nm; (c) 600nm and (d) 800nm. The cross sections have been inserted on top of each image and have the same scale bar.

To visualize more Ag nanorods samples systematically, Ag nanorods with the nominal thickness of 200, 300, 600 and 800 nm were grown on the Si substrate at the deposition angle θ =

86° using the e-beam evaporator. Cross section and top view of these samples were observed by SEM and are shown in Figure 4.14. For the Ag nanorods 200 nm, there are islands with random shapes on the surface and the anisotropism subtly can be seen from the cross section (Figure 4.14 (a)). When the nominal thickness increases to 300 nm, the size of those islands increases and the nanorods start to grow (Figure 4.14(b)). As the growth proceeds, the nanorods can be clearly seen for the nominal thickness 600 and 800 nm, as shown in Figures 4.14(c) and 4.14(d). By rough estimation, the diameter of the Ag nanorods with a nominal thickness 200, 300, 600 and 800 nm are 93, 93, 70 and 70 nm, respectively; the length are 70, 209, 535 and 744 nm, respectively.

4.3.3 Experiment results

4.3.3.1 SPR measurements of Ag film and Ag nanorods/Ag film

SPR measurements of Ag film and Ag nanorods/Ag film were first performed in air. The SPR reflectance is defined as the ratio between the reflectance from *p*-polarized incident light and that from *s*-polarized incident light.

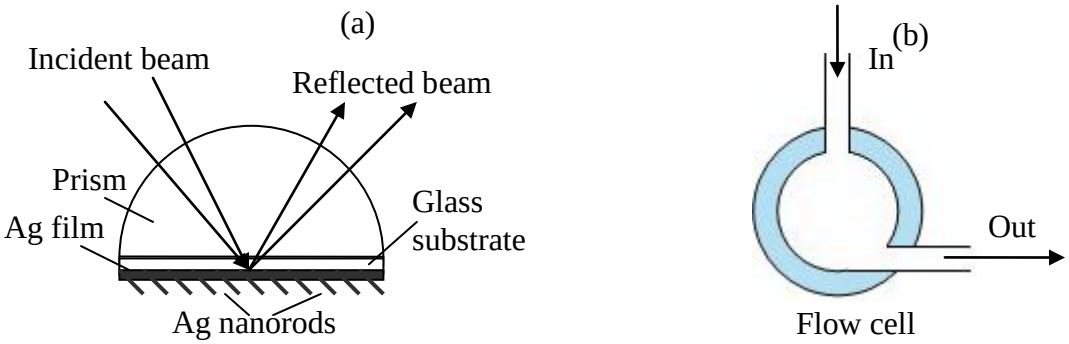

Figure 4.15 (a) Top view of the prism and the sample (without the flow cell). (b) Side view of flow cell.

Figure 4.15(a) is the top view of the prism and the Ag nanorods/film sample (without the flow cell). Ag nanorods and Ag film are deposited on the glass substrate and the other side of the glass slide is attached to the backside of the semi-cylindrical prism by using the index matching fluid (Cargille Laboratories Inc., Cedar Grove, NJ). The incident beam focuses on the interface between Ag film and the glass substrate, and interacts with Ag nanorods/film structure. Then the reflected beam is recorded as a function of the incident angle. When the measurement is performed in the aqueous solution, a flow cell made of teflon is attached onto the Ag surface and fixed by two screws. The side view of the flow cell is illustrated in Figure 4.15(b): the solution goes into the flow cell from the top and drains out from the bottom, and an O-ring is used to seal the cell (not shown).

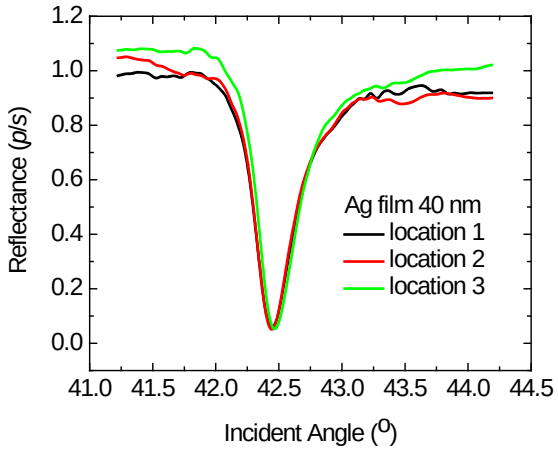

Figure 4.16 SPR reflectance curves of Ag film 40 nm.

Ag film with a thickness of 40 nm was measured at different locations and is shown in Figure 4.16. The surface looks uniform and has a SPR resonance angle located at 42.4°, which is a little different from the theoretical value 43.08°. The possible reasons are the error in film thickness (the effect on SPR angle by film thickness can refer to Figure 4.21), the error in the

SPR system. And in the theory, the film is supposed as perfectly smooth surface while the actual film has roughness.

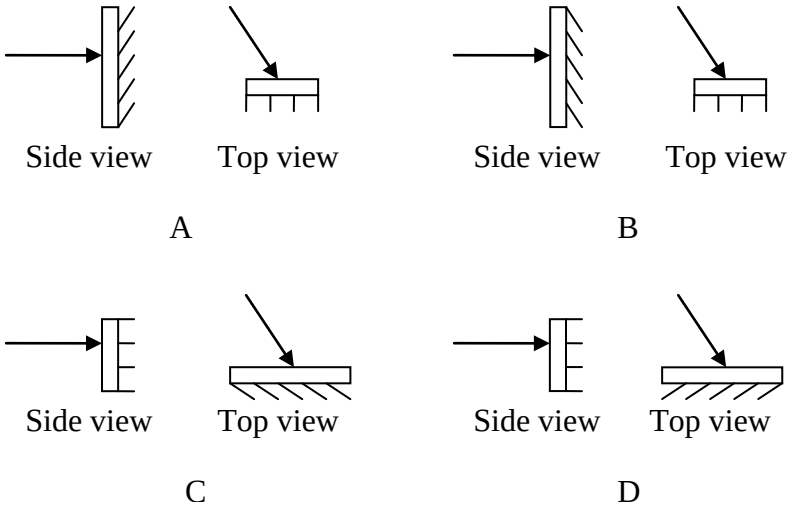

Figure 4.17 Measurement orientations of the Ag nanorods/Ag film sample.

Ag nanorods with a nominal thickness of 200 nm on Ag film with a thickness of 40 nm were measured by SPR system. Since the tilted Ag nanorods are anisotropic, four different orientations are chosen for the measurement (Figure 4.17). One should notice that the top view plane is parallel to the incident plane. For orientations A and B, the tilted nanorods are within a plane which is perpendicular to the incident plane. While for orientations C and D, the tilted nanorods are within the incident plane. The reflectance curves measured for different orientations are shown in Figure 4.18(a). There is a large SPR resonance angle for orientation A (solid line) and a small one for orientation B (dashed line). While the curves for orientations C (dotted line) and D (dot-dashed line) are almost overlapped with each other. Also, different locations were measured for each orientation and the SPR angle vs. locations is plotted in Figure 4.18(b). Similarly, it can be found that the measurement in orientation A has the largest SPR angle, the measurement in orientation B has the smallest SPR angle, the measurements in

orientations C and D only have the averaged 0.02° difference in SPR angle. For the Ag nanorods with a nominal thickness of 500 nm on Ag film 40 nm, we did not observe any SPR signal.

Smith has examined the transmittance and reflectance of an anisotropic nanorods layer in his paper and found that the reflectance is independent on the sign of the incident angle if the nanorods are lying in the incident plane. [163] This conclusion is consistent with the above measurements in orientations C and D. Though there is no complete theory regarding the orientations A and B, the results show that, when the tilted nanorods are in a plane perpendicular to the incident plane, different orientation would cause different SPR resonance angle.

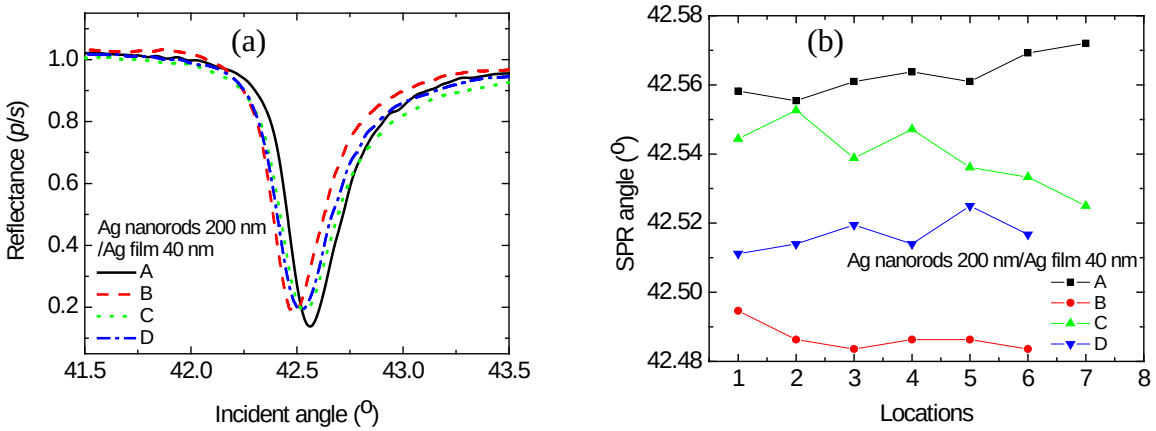

Figure 4.18 (a) SPR measurements in different orientations for Ag nanorods 200 nm/Ag film 40 nm sample. (b) SPR resonance angle vs. different locations for each orientation.

We define the Q-factor as

$$Q = \frac{\theta_{SPR}}{w}, \tag{4.32}$$

where θ_{SPR} is the SPR resonance angle and w is the width (FWHM) of the SPR curve. By normalizing the SPR curve, the width w is calculated as half of (1 – reflectance minimum). The comparison of the Q-factor between Ag film 40 nm and Ag nanorods 200 nm/Ag film 40 nm is

shown in table 4.1: the Ag nanorods/film shows a larger SPR resonance angle and a narrow width than Ag film, therefore has a higher Q-factor.

Table 4.1 Comparison of the Q-factor between Ag film and Ag nanorods / film.

	Ag film 40 nm	Ag nanorods 200 nm / film 40 nm (A)	Ag nanorods 200 nm / film 40 nm (B)	Ag nanorods 200 nm / film 40 nm (C)	Ag nanorods 200 nm / film 40 nm (D)
w (°)	0.33493	0.23063	0.19905	0.21436	0.20797
θ_{SPR} (°)	42.45178	42.56293	42.48679	42.53963	42.51673
Q-factor	126.7482	184.5507	213.4478	198.4495	204.4368

Efforts have also been put on the SPR measurements of Ag film and Ag nanorods/Ag film in DI water. Ag film with a thickness of 50 nm was fabricated and a thin layer of Ti film (1 nm) was deposited prior to the Ag deposition to enhance the adhesion in water.

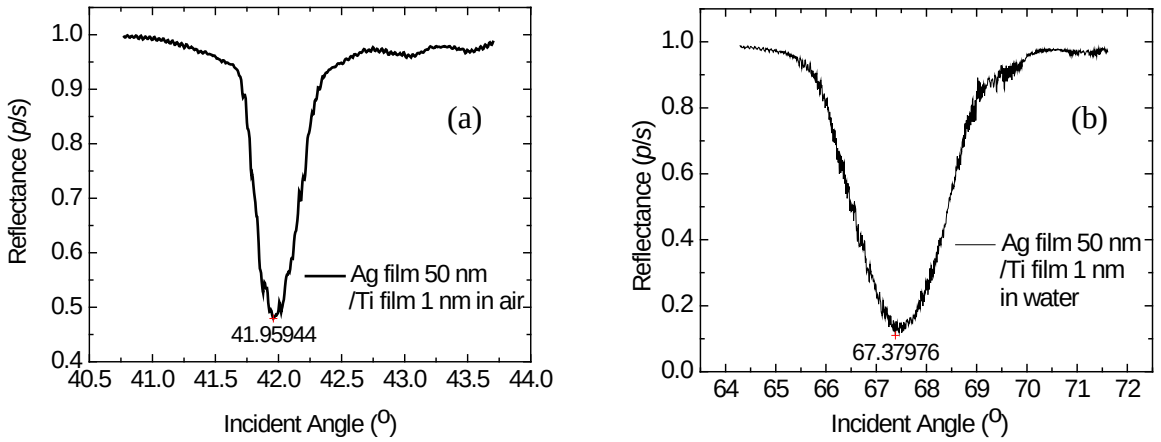

Figure 4.19 SPR reflectance curve of Ag film 50 nm/Ti film 1 nm (a) in air and (b) in water.

Figure 4.19(a) shows the reflectance of Ag film 50 nm in air and the SPR angle is 41.96°. When measurement was performed in DI water, the flow cell was attached on the Ag film surface and the water was pumped in. After a few minutes, the pump was stopped and the data was collected. Figure 4.19(b) shows the reflectance of Ag film 50 nm in water and the SPR angle shifts from 41. 96° to 67.38°. Though the absolute SPR angles are a little different from the

theory, the experimental shift 25.38° is very close to the theoretical value 25.04°. Obviously, the width becomes broad when the Ag surface is contacted by water, as the theory predicts. The curve looks a little noisy and we believe that this is caused by the line camera.

Ag nanorods with a nominal thickness of 200 nm was deposited onto Ag film 50 nm / Ti film 1 nm and measured in air. As shown in Figure 4.20, the SPR angle is 42.16°. However, we could not find any SPR signal when the Ag nanorods were contacted with DI water.

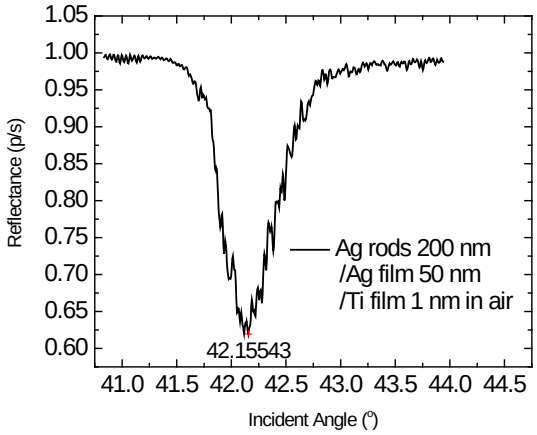

Figure 4.20 SPR reflectance curve of Ag nanorods 200 nm/Ag film 50 nm/Ti film 1 nm in air.

4.3.3.2 Comparison and discussion between Ag nanorods mediated SPR theory and experimental results

From the theory developed previously, in the case of Ag nanorods 200 nm/Ag film 40 nm (D = 93 nm, l = 70 nm), the minimum reflectance, SPR resonance angle and width in air are 0.9, 47.2° and 0.8°, respectively. However, the experimental results show that the minimum reflectance, SPR resonance angle and width in air are 0.2, 42.5° and 0.2°, respectively. We believe that the inconsistency is caused by the difference between the theoretical model and the actual morphology of the Ag nanorods 200 nm/Ag film 40 nm. As a matter of fact, it is hard to

treat the islands with the random shapes on the surface as the “spheroids”. In the case of Ag nanorods 500 nm/Ag film 40 nm, its morphology should be something between Figures 4.14(b) and 4.14(c), which is close to the theoretical model. According to the theory, if the length of the nanorods is larger than 200 nm, the minimum reflectance is very close to 1 and the SPR signal can not be observed. In addition, one can notice that all the nanorods have a diameter larger than 70 nm, indicating the SPR signal can not be observed in water.

It will be a little hard to discuss the trend of the width because there is a contradictory: the theory predicts that the Ag nanrods/film structure will result a broad width, while the experiments show the Ag nanorods 200 nm/Ag film 40 nm sample has a narrower width than the Ag film 40 nm sample.

Consider the conventional thin film SPR configuration and recall the SPR dispersion relation (1.13)

$$k_x = \frac{\omega}{c}\sqrt{\frac{\varepsilon_a \varepsilon_m}{\varepsilon_a + \varepsilon_m}}. \tag{4.33}$$

We have known that the resonance angle and the width are correlated to the real and imaginary part of k_x, respectively [77], i.e., a large real part induces a large resonance angle and a large imaginary part leads to a large width. Assuming $\varepsilon_m = \varepsilon' + i\varepsilon''$ and $\varepsilon'^2 >> \varepsilon''^2$, the real and imaginary part of k_x can be written as

$$\mathrm{Re}(k_x) = \left(\frac{\varepsilon_a \varepsilon'}{\varepsilon_a + \varepsilon'}\right)^{1/2}, \tag{4.34}$$

$$\mathrm{Im}(k_x) = \frac{\varepsilon_a^{3/2}\varepsilon''}{2(\varepsilon_a + \varepsilon')^{3/2}\varepsilon'^{1/2}}. \tag{4.35}$$

In addition, the complex refractive index of the metal

$$n_{com} = \sqrt{\varepsilon_m} = n_m + i\kappa_m, \tag{4.36}$$

where the absorption coefficient κ_m of noble metal is much larger than the refractive index n_m. When the thickness of the thin film increases, the absorption coefficient κ_m increases and thus $|\varepsilon'|$ increases. In general, $|\varepsilon'| > \varepsilon_a$, therefore Re($k_x$) and Im($k_x$) will decrease, indicating a small SPR angle and a narrow width. The relationships between SPR angle or width and the thin film thickness also can be simulated by the three-layer Fresnel equations and are plotted in Figure 4.21.

According to the SEM image of Ag nanorods 200 nm/Ag film 40 nm shown in Figure 4.14(a), the morphology is more close to film structure instead of nanorods structure. Therefore, the increasing film thickness results in a narrow width as listed in Table 4.1. However, the SPR angle of Ag nanorods 200 nm/Ag film 40 nm actually increases and the reason is still unknown.

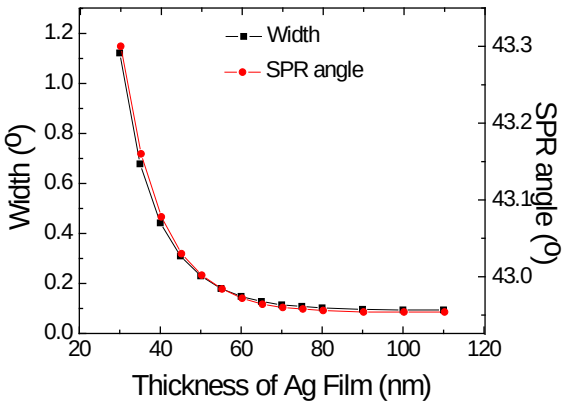

Figure 4.21 Relationships between SPR angle or width and the thin film thickness.

In the case of theoretical Ag nanorods structure, if we regard the nanorods layer and the thin film as an effective layer, the effective medium dielectric constant will have a smaller $|\varepsilon'|$ due to the porosity. According to equation (4.35), Im(k_x) will become larger and results in a large width.

Though we have not experimentally verified the enhancement predicted by the Ag nanorods/film structure, and tested the Ag nanorods mediated SPR sensor for *Salmonella* detection, we believe that there is a great potential for this sensor development.

4.4 Conclusion

In conclusion, we have carried out theoretical modeling of a nanorod mediated SPR sensor using anisotropic effective medium theory and studied the impact of various structural parameters such as the metal thin film thickness d_f, length l and diameter D of the nanorod on the properties of this SPR sensor. Compared with the conventional SPR configuration, nanorod mediated SPR sensor shows a larger resonance angle shift and its sensitivity increases with increasing refractive index of the target analyte. According to the calculation, the sensor with d_f = 30 nm, D = 30 nm and l = 20 nm performs best when the refractive index changing from n = 1 to n = 1.05; while in another index changing range, n = 1.3 to n = 1.34, the sensor with d_f = 50 nm, D = 10 nm and l = 10 nm enhances the sensitivity by two-fold. For the protein detection using a prim with the refractive index equal to 1.78, from n = 1.45 to n = 1.46, the sensor with d_f = 50 nm, D = 10 nm and l = 10 nm also enhances the sensitivity by two-fold. The results suggest that a nanorod mediated SPR sensor should be designed based on estimated index changes induced by target interactions.

Experiment investigation has been carried out for the Ag nanorods mediated SPR sensor. Due to the anisotropic property of the nanorods, it shows that different measurement orientation will result different SPR resonance angle. Compared with the conventional Ag thin film with a thickness of 40 nm, Ag nanorods 200 nm/Ag film 40 nm presents a larger SPR angle and a narrower width, therefore a higher Q-factor. However, the narrow width is thought as the result

of the “film-like” morphology, since the theory has proofed that the nanorods mediated SPR sensor should have a broadened width. Efforts have also been put on the measurements in aqueous solution such as DI water, but no SPR signal is observed for Ag nanorods/film structure. According to the theory, if the nanorods have a diameter larger than 70 nm and the measurement is performed in water, the reflectance minimum will be too close to 1 and is hard to be seen experimentally. We still believe that there is space left for the nanorods mediated SPR sensor for *Salmonella* detection, though the nanorods with a smaller diameter fabrication will be the first challenge to be faced.

CHAPTER 5

CONCLUSIONS AND FUTURE WORK

In this dissertation, the nanostructures fabricated by dynamic shadowing growth (DSG), which includes oblique angle deposition (OAD) and glancing angle deposition (GLAD), were investigated for *Salmonella* detection by means of optical sensors such as fluorescence immunosensor, localized surface plasmon resonance sensor and surface plasmon resonance sensor.

By combining GLAD and the sputtering technique, we have successfully fabricated Au/Si matchstick nanorods based immuno-fluorescence sensor for *Salmonella* detection. Single bacterium was captured by the antibodies conjugated on the Au and detected by the thousands of dye molecules immobilized on the Si nanorods. This fluorescence-based detection method provides a platform technology that may be applied to other pathogens detection, as the antibody used for capture can be substituted as required. For example, we have changed the anti-*Salmonella* antibody to *Respiratory Syncytial Virus* (RSV) antibodies, and have successfully detected the RSV infected cells.

Noble metal nanoparticles based localized surface plasmon resonance (LSPR) sensors were investigated by OAD produced Ag and Au nanoparticles (NPs). The tunable localized surface plasmon resonances of Ag NPs were achieved by simply changing the film thickness and the deposition angle. Compared with the normal deposited Ag islands film, the Ag NPs film fabricated by OAD at a large deposition angle has the advantage that the surface plasmon

resonance wavelength (SPRW) could be finely tuned in the visible range. For example, the average SPRW λ_p increment is less than 3nm per 5 nm in film thickness at $\theta = 85°$.

The response of the Au nanoparticle's localized plasmon peak to the outer environment was also investigated by depositing Ti with different thickness or deposition angle onto Au NPs. At normal deposition ($\theta_{Ti} = 0°$), we estimated that the critical distance z_c for Au NPs in this study is 20 nm and the maximum plasmon peak shift $\Delta\lambda_p$ is around 100 nm. By fixing the thickness of Ti, we also found that, with a larger deposition angle θ_{Ti}, the plasmon peak shifts less because the smaller coverage of Ti on Au NPs can only change a smaller part of the surrounding medium. We recently found that the Au NPs fabricated by GLAD were more uniform than those made by OAD, which is promising for the optimization of the Au NPs based LSPR sensor. Also, a sandwich structure of Au NPs/TiO_2/Au NPs was found that the second Au NP deposition increased the surface area of the NPs but not made the plasmon peak red-shift.

The sensor applications of Ag or Au NPs films have been explored. Though we found the Ag film could be oxidized in the aqueous solution with a blue shift of λ_p, a self-assembled monolayer such as SSC or Biotin could be used to protect the Ag surface and a stable λ_p can be achieved. We also showed that the Ag NPs based LSPR sensor can monitor the binding between Biotin and NeutrAvidin, and the limit of detection (LOD) is 10^{-10} M. There is space left for enhancement if the Ag NPs film with narrower width is used.

Since Au is more stable than Ag in aqueous solutions especially containing salt, we fabricated Au NPs based LSPR sensor for *Salmonella* detection. In this sensor application, *Salmonella* bacteria, polystyrene spheres, and silica beads were coated onto the Au NP substrates, and the absorbance spectra before and after the coating were measured. According to the results, the plasmon peaks randomly blue- or red-shift and the peak shifts were less than 6 nm. By

utilizing the Mie theory and effective medium theory, we constructed a simplified theoretical model and found that the plasmon peaks would theoretically shift 2-4 nm for the above samples, which was very close to the experimental results. Combining the considerations of the systematic error and the overestimated theoretical results, we believe that the detection ability of the LSPR sensor has a limitation for whole bacteria cells if using a conventional UV-Vis spectrometer. However, we should point out that this conclusion is based on the assumption that *Salmonella* bacteria have a rigid body. There might be other reasons for the unsuccessful detection, which are still under investigation.

Surface plasmon resonance (SPR) sensor has been commercially developed, which contains a thin film of Au or Ag with a thickness of 50 nm. To enhance the sensor sensitivity, Ag nanorods mediated SPR sensor was studied theoretically using anisotropic effective medium theory. Compared with the conventional SPR configuration, nanorod mediated SPR sensor shows a larger resonance angle shift and its sensitivity increases with increasing refractive index of the target analyte. According to the calculation, the sensor with d_f = 30 nm, D = 30 nm and l = 20 nm performs best when the refractive index changing from n = 1 to n = 1.05; while in another index changing range, n = 1.3 to n = 1.34, the sensor with d_f = 50 nm, D = 10 nm and l = 10 nm enhances the sensitivity by two-fold.

Experiment investigation has been carried out for the Ag nanorods mediated SPR sensor. Due to the anisotropic property of the nanorods, it shows that different measurement orientation will result different SPR resonance angle. Compared with the conventional Ag thin film with a thickness of 40 nm, Ag nanorods 200 nm/Ag film 40 nm presents a larger SPR angle and a narrower width, therefore a higher Q-factor. Efforts have also been put on the measurements in aqueous solution such as DI water, but no SPR signal is observed for Ag nanorods/film structure.

According to the theory, if the nanorods have a diameter larger than 70 nm and the measurement is performed in water, the reflectance minimum will be too close to 1 and is hard to be seen experimentally.

In the future, it will be interesting to perform the following search. For the Au/Si nanorods based biosensor, the fluorescent detection dye can be replaced by other types of dyes or potentially quantum dots that may allow for multiplex detection. Also, other nano-building blocks such as the spherical silica nanoparticles or the commercially available fluorescent silica nanoparticles, after partially coated with Au, can be used as the same detection biomarkers, though other techniques will be needed to deal with the Au coating and the antibody conjugation. To overcome the limitation of the Au NPs based LSPR sensor for *Salmonella*, if the technique permits, we might lyse the bacterial cells into fragments, which are smaller than the NPs. Another alternative is that we can apply the antibody labeled Au NPs to the bacteria which have been captured on the substrates. Third, the sandwich structure of Au NPs/TiO2/Au NPs has a great potential for the LSPR sensing. Regarding the nanorods mediated SPR sensor, we believe that there are ways to control the dimensions of the Ag nanorods and make the actual sensor structure close to the theoretical model, and therefore enhance the sensitivity of *Salmonella* detection. Additionally, the fine tune LSPR property of Ag or Au NPs is very useful for LSPR and SPR sensors.

REFERENCES

1. Feldsine, P.T., A.H. Lienau, S.C. Leung, L.A. Mui, F. Humbert, M. Bohnert, K. Mooijman, S. Schulten, P. in't Veld, P. Rollier, R. Leuschner, and K. Capps, *Detection of Salmonella in fresh cheese, poultry products, and dried egg products by the ISO 6579 Salmonella culture procedure and the AOAC official method: Collaborative study.* Journal of Aoac International, 2003. **86**(2): p. 275-295.
2. Munson, T.E., J.P. Schrade, N.B. Bisciello, L.D. Fantasia, W.H. Hartung, and J.J. Oconnor, *Evaluation of an automated fluorescent-antibody procedure for detection of Salmonella in foods and feeds.* Applied and Environmental Microbiology, 1976. **31**(4): p. 514-521.
3. Walker, R.L., H. Kinde, R.J. Anderson, and A.E. Brown, *Comparison of VIDAS enzyme-linked fluorescent immunoassay using Moore swab sampling and conventional culture method for Salmonella detection in bulk tank milk and in-line milk filters in California dairies.* International Journal of Food Microbiology, 2001. **67**(1-2): p. 123-129.
4. Uyttendaele, M., K. Vanwildemeersch, and J. Debevere, *Evaluation of real-time PCR vs automated ELISA and a conventional culture method using a semi-solid medium for detection of Salmonella.* Letters in Applied Microbiology, 2003. **37**(5): p. 386-391.
5. Hein, I., G. Flekna, M. Krassnig, and M. Wagner, *Real-time PCR for the detection of Salmonella spp. in food: An alternative approach to a conventional PCR system suggested by the FOOD-PCR project.* Journal of Microbiological Methods, 2006. **66**(3): p. 538-547.
6. Myint, M.S., Y.J. Johnson, N.L. Tablante, and R.A. Heckert, *The effect of pre-enrichment protocol on the sensitivity and specificity of PCR for detection of naturally contaminated Salmonella in raw poultry compared to conventional culture.* Food Microbiology, 2006. **23**(6): p. 599-604.
7. Aleixo, J.A.G. and B. Swaminathan, *A fluorescent enzyme-immunoassay for Salmonella detection.* Journal of Immunoassay, 1988. **9**(1): p. 83-95.
8. McClelland, R.G. and A.C. Pinder, *Detection of low-levels of specific Salmonella species by fluorescent-antibodies and flow-cytometry.* Journal of Applied Bacteriology, 1994. **77**(4): p. 440-447.
9. Minet, J., C. Desmonts, M. Pommepuy, and M. Cormier, *Salmonella detection in sewage waters using fluorescent-antibodies.* Water Science and Technology, 1991. **24**(2): p. 373-376.
10. Mohr, H.K., H.L. Trenk, and M. Yeterian, *Comparison of fluorescent-antibody methods and enrichment serology for detection of Salmonella.* Applied Microbiology, 1974. **27**(2): p. 324-328.
11. Thomason, B.M., *Rapid detection of Salmonella microcolonies by fluorescent antibody.* Applied Microbiology, 1971. **22**(6): p. 1064-&.

12. Kumar, S., K. Balakrishna, and H. Batra, *Enrichment-ELISA for detection of Salmonella typhi from food and water samples.* Biomedical and Environmental Sciences, 2008. **21**(2): p. 137-143.
13. Schneid, A.D., K.L. Rodrigues, D. Chemello, E.C. Tondo, M.A.Z. Ayub, and J.A.G. Aleixo, *Evaluation of an indirect ELISA for the detection of Salmonella in chicken meat.* Brazilian Journal of Microbiology, 2006. **37**(3): p. 350-355.
14. Tian, H.Z., T. Miyamoto, T. Okabe, Y. Kuramitsu, K. Honjoh, and S. Hatano, *Rapid detection of Salmonella spp, in foods by combination of a new selective enrichment and a sandwich ELISA using two monoclonal antibodies against dulcitol 1-phosphate dehydrogenase.* Journal of Food Protection, 1996. **59**(11): p. 1158-1163.
15. Tan, S., C.L. Gyles, and B.N. Wilkie, *Comparison of an LPS-specific competitive ELISA with a motility enrichment culture method (MSRV) for detection of Salmonella typhimurium and S-enteritidis in chickens.* Veterinary Microbiology, 1997. **56**(1-2): p. 79-86.
16. Scheu, P., A. Gasch, R. Zschaler, K. Berghof, and F. Wilborn, *Evaluation of a PCR-ELISA for food testing: Detection of selected Salmonella serovars in confectionery products.* Food Biotechnology, 1998. **12**(1-2): p. 1-12.
17. Rahman, H., *Dot-ELISA for detection of Salmonella enterotoxin.* Indian Journal of Medical Research, 1999. **110**: p. 47-49.
18. Tapchaisri, P., P. Wangroongsarb, W. Panbangred, T. Kalambaheti, M. Chongsa-nguan, P. Srimanote, H. Kurazono, H. Hayashi, and W. Chaicumpa, *Detection of Salmonella contamination in food samples by Dot-ELISA, DNA amplification and bacterial culture.* Asian Pacific Journal of Allergy and Immunology, 1999. **17**(1): p. 41-51.
19. Kanki, M., J. Sakata, M. Taguchi, Y. Kumeda, M. Ishibashi, T. Kawai, K. Kawatsu, W. Yamasaki, K. Inoue, and M. Miyahara, *Effect of sample preparation and bacterial concentration on Salmonella enterica detection in poultry meat using culture methods and PCR assaying of preenrichment broths.* Food Microbiology, 2009. **26**(1): p. 1-3.
20. Gallegos-Robles, M.A., A. Morales-Loredo, G. Alvarez-Ojeda, J.A. Osuna-Garcia, I.O. Martinez, L.H. Morales-Ramos, and P. Fratamico, *PCR Detection and Microbiological Isolation of Salmonella spp. from Fresh Beef and Cantaloupes.* Journal of Food Science, 2009. **74**(1): p. M37-M40.
21. Cheng, C.M., W. Lin, K.T. Van, L. Phan, N.N. Tran, and D. Farmer, *Rapid Detection of Salmonella in Foods Using Real-Time PCR.* Journal of Food Protection, 2008. **71**(12): p. 2436-2441.
22. Correa, A.A., J. Toso, J.D. Albarnaz, C.M.O. Simoes, and C.R.M. Barardi, *Detection of Salmonella typhimurium in oysters by PCR and molecular hybridization.* Journal of Food Quality, 2006. **29**(5): p. 458-469.
23. Trafny, E.A., K. Kozlowska, and M. Szpakowska, *A novel multiplex PCR assay for the detection of Salmonella enterica serovar Enteritidis in human faeces.* Letters in Applied Microbiology, 2006. **43**(6): p. 673-679.
24. Wang, X.W., N. Jothikumar, and M.W. Griffiths, *Enrichment and DNA extraction protocols for the simultaneous detection of Salmonella and Listeria monocytogenes in raw sausage meat with multiplex real-time PCR.* Journal of Food Protection, 2004. **67**(1): p. 189-192.

25. Notzon, A., R. Helmuth, and J. Bauer, *Evaluation of an immunomagnetic separation-real-time PCR assay for the rapid detection of Salmonella in meat.* Journal of Food Protection, 2006. **69**(12): p. 2896-2901.
26. Bokken, G., R.J. Corbee, F. van Knapen, and A.A. Bergwerff, *Immunochemical detection of Salmonella group B, D and E using an optical surface plasmon resonance biosensor.* Fems Microbiology Letters, 2003. **222**(1): p. 75-82.
27. Waswa, J.W., C. Debroy, and J. Irudayaraj, *Rapid detection of Salmonella enteritidis and Escherichia coli using surface plasmon resonance biosensor.* Journal of Food Process Engineering, 2006. **29**(4): p. 373-385.
28. Lan, Y.B., S.Z. Wang, Y.G. Yin, W.C. Hoffmann, and X.Z. Zheng, *Using a Surface Plasmon Resonance Biosensor for Rapid Detection of Salmonella Typhimurium in Chicken Carcass.* Journal of Bionic Engineering, 2008. **5**(3): p. 239-246.
29. Nandakumar, V., J.T. La Belle, J. Reed, M. Shah, D. Cochran, L. Joshi, and T.L. Alford, *A methodology for rapid detection of Salmonella typhimurium using label-free electrochemical impedance spectroscopy.* Biosensors & Bioelectronics, 2008. **24**(4): p. 1039-1042.
30. Ruan, C.M., L.J. Yang, and Y.B. Li, *Rapid detection of viable Salmonella typhimurium in a selective medium by monitoring oxygen consumption with electrochemical cyclic voltammetry.* Journal of Electroanalytical Chemistry, 2002. **519**(1-2): p. 33-38.
31. Ye, J.M., S.V. Letcher, and A.G. Rand, *Piezoelectric biosensor for detection of Salmonella typhimurium.* Journal of Food Science, 1997. **62**(5): p. 1067-&.
32. Babacan, S., P. Pivarnik, S. Letcher, and A. Rand, *Piezoelectric flow injection analysis biosensor for the detection of Salmonella typhimurium.* Journal of Food Science, 2002. **67**(1): p. 314-320.
33. Pathirana, S.T., J. Barbaree, B.A. Chin, M.G. Hartell, W.C. Neely, and V. Vodyanoy, *Rapid and sensitive biosensor for Salmonella.* Biosensors & Bioelectronics, 2000. **15**(3-4): p. 135-141.
34. Dill, K., L.H. Stanker, and C.R. Young, *Detection of salmonella in poultry using a silicon chip-based biosensor.* Journal of Biochemical and Biophysical Methods, 1999. **41**(1): p. 61-67.
35. Seo, K.H., R.E. Brackett, N.F. Hartman, and D.P. Campbell, *Development of a rapid response biosensor for detection of Salmonella typhimurium.* Journal of Food Protection, 1999. **62**(5): p. 431-437.
36. Zhou, C.H., P. Pivarnik, A.G. Rand, and S.V. Letcher, *Acoustic standing-wave enhancement of a fiber-optic Salmonella biosensor.* Biosensors & Bioelectronics, 1998. **13**(5): p. 495-500.
37. Ko, S.H. and S.A. Grant, *A novel FRET-based optical fiber biosensor for rapid detection of Salmonella typhimurium.* Biosensors & Bioelectronics, 2006. **21**(7): p. 1283-1290.
38. Guntupalli, R., J. Hu, R.S. Lakshmanan, T.S. Huang, J.M. Barbaree, and B.A. Chin, *A magnetoelastic resonance biosensor immobilized with polyclonal antibody for the detection of Salmonella typhimurium.* Biosensors & Bioelectronics, 2007. **22**(7): p. 1474-1479.
39. Zhang, D. and E.C. Alocilja, *Characterization of nanoporous silicon-based DNA biosensor for the detection of Salmonella Enteritidis.* Ieee Sensors Journal, 2008. **8**(5-6): p. 775-780.

40. Varshney, M., Y.B. Li, R. Nanapanneni, M.G. Johnson, and C.L. Griffis, *A chemiluminescence biosensor coupled with immunomagnetic separation for rapid detection of Salmonella typhimurium.* Journal of Rapid Methods and Automation in Microbiology, 2003. **11**(2): p. 111-131.
41. Edgar, R., M. McKinstry, J. Hwang, A.B. Oppenheim, R.A. Fekete, G. Giulian, C. Merril, K. Nagashima, and S. Adhya, *High-sensitivity bacterial detection using biotin-tagged phage and quantum-dot nanocomplexes.* Proceedings of the National Academy of Sciences of the United States of America, 2006. **103**(13): p. 4841-4845.
42. Yang, L.J. and Y.B. Li, *Quantum dots as fluorescent labels for quantitative detection of Salmonella typhimurium in chicken carcass wash water.* Journal of Food Protection, 2005. **68**(6): p. 1241-1245.
43. Thomas, E., A. Bouma, E. van Eerden, W.J.M. Landman, F. van Knapen, A. Stegeman, and A.A. Bergwerff, *Detection of egg yolk antibodies reflecting Salmonella enteritidis infections using a surface plasmon resonance biosensor.* Journal of Immunological Methods, 2006. **315**(1-2): p. 68-74.
44. Henry, R., A. Anand, M. Chowdhury, G. Cote, R. Moreira, and T. Good, *Development of a nanoparticle-based surface-modified fluorescence assay for the detection of prion proteins.* Analytical Biochemistry, 2004. **334**(1): p. 1-8.
45. Agrawal, A., R.A. Tripp, L.J. Anderson, and S.M. Nie, *Real-time detection of virus particles and viral protein expression with two-color nanoparticle probes.* Journal of Virology, 2005. **79**(13): p. 8625-8628.
46. Valanne, A., S. Huopalahti, R. Vainionpaa, H. Harma, and T. Lovgren, *Rapid and sensitive HBsAg immunoassay based on fluorescent nanoparticle labels and time-resolved detection.* Journal of Virological Methods, 2005. **129**(1): p. 83-90.
47. Wang, W., C.M. Ruan, and B.H. Gu, *Development of gold-silica composite nanoparticle substrates for perchlorate detection by surface-enhanced Raman spectroscopy.* Analytica Chimica Acta, 2006. **567**(1): p. 121-126.
48. Buyana, T., *Molecular Physics*. 1997, Singapore: World Scientific Publishing Co. Pte. Ltd.
49. Daudel, R., G. Leroy, D. Peeters, and M. Sana, *Quantum Chemistry*. 1983: John Wiley & Sons Ltd.
50. Amadeo J. Pesce, C.-G.R., Terry L. Pasby, *Fluorescence Spectroscopy*. 1971, New York: Marcel Dekker Inc.
51. Silva, M., H. Cruz, O. Rossetti, A. Arese, and A. Oliva, *Development of an optical immunosensor based on the fluorescence of Cyanine-5 for veterinarian diagnostics.* Biotechnology Letters, 2004. **26**(12): p. 993-997.
52. Vidal, M., M. Prata, S. Santos, T. Tavares, J. Hossfeld, C. Preininger, and A. Oliva, *Fluorescence IgG immunosensor based on a micro flow cell containing controlled pore glass as immobilisation support.* Analyst, 2000. **125**(8): p. 1387-1391.
53. Silvestre, O.F., M.G. Silva, A.G. Oliva, and H.J. Cruz, *Spherical vs. granular immobilization support selection and performance on an optical flow cell immunosensor based on the fluorescence of cyanine-5.* Preparative Biochemistry & Biotechnology, 2006. **36**(4): p. 333-353.
54. Chudinova, G.K., A.V. Chudinov, V.V. Savransky, and A.M. Prokhorov, *The study of the antigen-antibody reaction by fluorescence method in LB films for immunosensor.* Thin Solid Films, 1997. **307**(1-2): p. 294-297.

55. Jackson, J.D., *Classical electrodynamics*. 1999: John Wiley & Sons, Inc.
56. Pitarke, J.M., V.M. Silkin, E.V. Chulkov, and P.M. Echenique, *Theory of surface plasmons and surface-plasmon polaritons.* Reports on Progress in Physics, 2007. **70**(1): p. 1-87.
57. Sambles, J.R., G.W. Bradbery, and F.Z. Yang, *Optical-Excitation of Surface-Plasmons - an Introduction.* Contemporary Physics, 1991. **32**(3): p. 173-183.
58. Craig F. Bohren, D.R.H., *Absorption and scattering of light by small particles* 1983: New York : Wiley.
59. Otto, A., *Excitation of Nonradiative Surface Plasma Waves in Silver by Method of Frustrated Total Reflection.* Zeitschrift Fur Physik, 1968. **216**(4): p. 398-&.
60. Kishimoto, S., S. Ohshio, H. Akasaka, and H. Saitoh, *Detection of Protein Adsorption on Silica Surface Using Surface Plasmon Resonance Sensor.* Japanese Journal of Applied Physics, 2008. **47**(10): p. 8106-8108.
61. Li, X.L., M.H. Huang, H.M. Cao, Y. Chen, J.L. Zhao, and M.S. Yang, *Phosphorylation of Receptor-mimic Tyrosine Peptide on Surface Plasmon Resonance Sensor Chip Surface and Its Interaction with Downstream Proteins.* Chinese Journal of Analytical Chemistry, 2008. **36**(10): p. 1327-1332.
62. Jin, W., X.C. Lin, S.W. Lv, Y. Zhang, Q.H. Jin, and Y. Mu, *A DNA sensor based on surface plasmon resonance for apoptosis-associated genes detection.* Biosensors & Bioelectronics, 2009. **24**(5): p. 1266-1269.
63. Ladd, J., A.D. Taylor, M. Piliarik, J. Homola, and S. Jiang, *Hybrid surface platform for the simultaneous detection of proteins and DNAs using a surface plasmon resonance imaging sensor.* Analytical Chemistry, 2008. **80**(11): p. 4231-4236.
64. Prabhakar, N., K. Arora, S.K. Arya, P.R. Solanki, M. Iwamoto, H. Singh, and B.D. Malhotra, *Nucleic acid sensor for M-tuberculosis detection based on surface plasmon resonance.* Analyst, 2008. **133**(11): p. 1587-1592.
65. Lisboa, P., A. Valsesia, I. Mannelli, S. Mornet, P. Colpo, and F. Rossi, *Sensitivity enhancement of surface-plasmon resonance imaging by nanoarrayed organothiols.* Advanced Materials, 2008. **20**(12): p. 2352-+.
66. Ladd, J., A.D. Taylor, J. Homola, and S.Y. Jiang, *Detection of botulinum neurotoxins in buffer and honey using a surface plasmon resonance (SPR) sensor.* Sensors and Actuators B-Chemical, 2008. **130**(1): p. 129-134.
67. Solanki, P.R., N. Prabhakar, M.K. Pandey, and B.D. Malhotra, *Self-assembled monolayer for toxicant detection using nucleic acid sensor based on surface plasmon resonance technique.* Biomedical Microdevices, 2008. **10**(5): p. 757-767.
68. Taylor, A.D., J. Ladd, S. Etheridge, J. Deeds, S. Hall, and S.Y. Jiang, *Quantitative detection of tetrodotoxin (TTX) by a surface plasmon resonance (SPR) sensor.* Sensors and Actuators B-Chemical, 2008. **130**(1): p. 120-128.
69. Waswa, J., J. Irudayaraj, and C. DebRoy, *Direct detection of E-Coli O157 : H7 in selected food systems by a surface plasmon resonance biosensor.* Lwt-Food Science and Technology, 2007. **40**(2): p. 187-192.
70. Su, C.B. and J. Kameoka, *Forty-four pass fibre-optic loop for improving the sensitivity of surface plasmon resonance sensors.* Measurement Science & Technology, 2008. **19**(1).
71. Gupta, B.D. and A.K. Sharma, *Sensitivity evaluation of a multi-layered surface plasmon resonance-based fiber optic sensor: a theoretical study.* Sensors and Actuators B-Chemical, 2005. **107**(1): p. 40-46.

72. Verma, R.K. and B.D. Gupta, *Theoretical modelling of a bi-dimensional U-shaped surface plasmon resonance based fibre optic sensor for sensitivity enhancement.* Journal of Physics D-Applied Physics, 2008. **41**(9).
73. Yuk, J.S., D.G. Hong, J.W. Jung, S.H. Jung, H.S. Kim, J.A. Han, Y.M. Kim, and K.S. Ha, *Sensitivity enhancement of spectral surface plasmon resonance biosensors for the analysis of protein arrays.* European Biophysics Journal with Biophysics Letters, 2006. **35**(6): p. 469-476.
74. Gupta, G. and J. Kondoh, *Tuning and sensitivity enhancement of surface plasmon resonance sensor.* Sensors and Actuators B-Chemical, 2007. **122**(2): p. 381-388.
75. Yuan, X.C., B. Hong, Y.G. Tan, D.W. Zhang, R. Irawan, and S.C. Tjin, *Sensitivity-stability-optimized surface plasmon resonance sensing with double metal layers.* Journal of Optics a-Pure and Applied Optics, 2006. **8**(11): p. 959-963.
76. Szunerits, S., X. Castel, and R. Boukherroub, *Surface plasmon resonance investigation of silver and gold films coated with thin indium tin oxide layers: Influence on stability and sensitivity.* Journal of Physical Chemistry C, 2008. **112**(40): p. 15813-15817.
77. Byun, K.M., D. Kim, and S.J. Kim, *Investigation of the profile effect on the sensitivity enhancement of nanowire-mediated localized surface plasmon resonance biosensors.* Sensors and Actuators B-Chemical, 2006. **117**(2): p. 401-407.
78. Byun, K.M., S.J. Yoon, D. Kim, and S.J. Kim, *Experimental study of sensitivity enhancement in surface plasmon resonance biosensors by use of periodic metallic nanowires.* Optics Letters, 2007. **32**(13): p. 1902-1904.
79. Byun, K.M., S.J. Yoon, D. Kim, and S.J. Kim, *Sensitivity analysis of a nanowire-based surface plasmon resonance biosensor in the presence of surface roughness.* Journal of the Optical Society of America a-Optics Image Science and Vision, 2007. **24**(2): p. 522-529.
80. Gu, J.H., H. Lu, Y.W. Chen, L.Y. Liu, P. Wang, J.M. Ma, and Z.H. Lu, *Enhancement of the sensitivity of surface plasmon resonance biosensor with colloidal gold labeling technique.* Supramolecular Science, 1998. **5**(5-6): p. 695-698.
81. Kim, D., *Effect of resonant localized plasmon coupling on the sensitivity enhancement of nanowire-based surface plasmon resonance biosensors.* Journal of the Optical Society of America a-Optics Image Science and Vision, 2006. **23**(9): p. 2307-2314.
82. Leung, P.T., D. Pollardknight, G.P. Malan, and M.F. Finlan, *Modeling of Particle-Enhanced Sensitivity of the Surface-Plasmon-Resonance Biosensor.* Sensors and Actuators B-Chemical, 1994. **22**(3): p. 175-180.
83. Pang, L., G.M. Hwang, B. Slutsky, and Y. Fainman, *Spectral sensitivity of two-dimensional nanohole array surface plasmon polariton resonance sensor.* Applied Physics Letters, 2007. **91**(12).
84. Yang, X.Y. and D.M. Liu, *Sensitivity enhancement of surface plasmon resonance sensors through planar metallic film closely coupled to nanogratings.* Chinese Optics Letters, 2007. **5**(10): p. 563-565.
85. Yoon, S.J. and D. Kim, *Target dependence of the sensitivity in periodic nanowire-based localized surface plasmon resonance biosensors.* Journal of the Optical Society of America a-Optics Image Science and Vision, 2008. **25**(3): p. 725-735.
86. Zhang, D., P. Wang, X. Jiao, G. Yuan, J. Zhang, C. Chen, H. Ming, and R. Rao, *Investigation of the sensitivity of H-shaped nano-grating surface plasmon resonance biosensors using rigorous coupled wave analysis.* Applied Physics a-Materials Science & Processing, 2007. **89**(2): p. 407-411.

87. Zou, S.L. and G.C. Schatz, *Narrow plasmonic/photonic extinction and scattering line shapes for one and two dimensional silver nanoparticle arrays.* Journal of Chemical Physics, 2004. **121**(24): p. 12606-12612.
88. Byun, K.M., M.L. Shuler, S.J. Kim, S.J. Yoon, and D. Kim, *Sensitivity enhancement of surface plasmon resonance imaging using periodic metallic nanowires.* Journal of Lightwave Technology, 2008. **26**(9-12): p. 1472-1478.
89. Scaffardi, L.B. and J.O. Tocho, *Size dependence of refractive index of gold nanoparticles.* Nanotechnology, 2006. **17**(5): p. 1309-1315.
90. Lin, T.J. and M.F. Chung, *Detection of cadmium by a fiber-optic biosensor based on localized surface plasmon resonance.* Biosensors & Bioelectronics, 2009. **24**(5): p. 1213-1218.
91. Hiep, H.M., T. Endo, M. Saito, M. Chikae, D.K. Kim, S. Yamamura, Y. Takamura, and E. Tamiya, *Label-free detection of melittin binding to a membrane using electrochemical-localized surface plasmon resonance.* Analytical Chemistry, 2008. **80**(6): p. 1859-1864.
92. Hiep, H.M., T. Endo, K. Kerman, M. Chikae, D.K. Kim, S. Yamamura, Y. Takamura, and E. Tamiya, *A localized surface plasmon resonance based immunosensor for the detection of casein in milk.* Science and Technology of Advanced Materials, 2007. **8**(4): p. 331-338.
93. Shen, X.W., C.Z. Huang, and Y.F. Li, *Localized surface plasmon resonance sensing detection of glucose in the serum samples of diabetes sufferers based on the redox reaction of chlorauric acid.* Talanta, 2007. **72**(4): p. 1432-1437.
94. Endo, T., K. Kerman, N. Nagatani, Y. Takamura, and E. Tamiya, *Label-free detection of peptide nucleic acid-DNA hybridization using localized surface plasmon resonance based optical biosensor.* Analytical Chemistry, 2005. **77**(21): p. 6976-6984.
95. Barbillon, G., A.C. Faure, N. El Kork, P. Moretti, S. Roux, O. Tillement, M.G. Ou, A. Descamps, P. Perriat, A. Vial, J.L. Bijeon, C.A. Marquette, and B. Jacquier, *How nanoparticles encapsulating fluorophores allow a double detection of biomolecules by localized surface plasmon resonance and luminescence.* Nanotechnology, 2008. **19**(3).
96. Endo, T., H. Takizawa, Y. Yanagida, T. Hatsuzawa, and E. Tamiya, *Construction of a Biosensor Operating on the Combined Principles of Electrochemical Analysis and Localized Surface Plasmon Resonance for Multiple Detection of Antigen-Antibody and Enzymatic Reactions on the Single Biosensor.* Sensors and Materials, 2008. **20**(6): p. 255-265.
97. Endo, T., K. Kerman, N. Nagatani, H.M. Hiepa, D.K. Kim, Y. Yonezawa, K. Nakano, and E. Tamiya, *Multiple label-free detection of antigen-antibody reaction using localized surface plasmon resonance-based core-shell structured nanoparticle layer nanochip.* Analytical Chemistry, 2006. **78**(18): p. 6465-6475.
98. Wadayama, T., O. Suzuki, K. Takeuchi, H. Seki, T. Tanabe, Y. Suzuki, and A. Hatta, *IR absorption enhancement for physisorbed methanol on Ag island films deposited on the oxidized and H-terminated Si(111) surfaces: effect of the metal surface morphology.* Applied Physics a-Materials Science & Processing, 1999. **69**(1): p. 77-80.
99. Tarcha, P.J., J. DeSaja-Gonzalez, S. Rodriguez-Llorente, and R. Aroca, *Surface-enhanced fluorescence on SiO2-coated silver island films.* Applied Spectroscopy, 1999. **53**(1): p. 43-48.

100. Jensen, T.R., R.P. Van Duyne, S.A. Johnson, and V.A. Maroni, *Surface-enhanced infrared spectroscopy: A comparison of metal island films with discrete and nondiscrete surface plasmons.* Applied Spectroscopy, 2000. **54**(3): p. 371-377.
101. Pipino, A.C.R., R.P. VanDuyne, and G.C. Schatz, *Surface-enhanced second-harmonic diffraction: Experimental investigation of selective enhancement.* Physical Review B, 1996. **53**(7): p. 4162-4169.
102. Yang, Y., M. Nogami, J.L. Shi, H.R. Chen, G.H. Ma, and S.H. Tang, *Controlled surface-plasmon coupling in SiO2-coated gold nanochains for tunable nonlinear optical properties.* Applied Physics Letters, 2006. **88**(8).
103. Zheng, X.L., W.Q. Xu, C. Corredor, S.P. Xu, J. An, B. Zhao, and J.R. Lombardi, *Laser-induced growth of monodisperse silver nanoparticles with tunable surface plasmon resonance properties and a wavelength self-limiting effect.* Journal of Physical Chemistry C, 2007. **111**(41): p. 14962-14967.
104. Bouhelier, A., R. Bachelot, G. Lerondel, S. Kostcheev, P. Royer, and G.P. Wiederrecht, *Surface plasmon characteristics of tunable photoluminescence in single gold nanorods.* Physical Review Letters, 2005. **95**(26).
105. Barnes, W.L., A. Dereux, and T.W. Ebbesen, *Surface plasmon subwavelength optics.* Nature, 2003. **424**(6950): p. 824-830.
106. Whelan, A.M., M.E. Brennan, W.J. Blau, and J.M. Kelly, *Enhanced third-order optical nonlinearity of silver nanoparticles with a tunable surface plasmon resonance.* Journal of Nanoscience and Nanotechnology, 2004. **4**(1-2): p. 66-68.
107. Alvarez-Puebla, R.A., D.J. Ross, G.A. Nazri, and R.F. Aroca, *Surface-enhanced Raman scattering on nanoshells with tunable surface plasmon resonance.* Langmuir, 2005. **21**(23): p. 10504-10508.
108. Gao, J.N., X.L. Ren, D. Chen, F.Q. Tang, and J. Ren, *Bimetallic Ag-Pt hollow nanoparticles: Synthesis and tunable surface plasmon resonance.* Scripta Materialia, 2007. **57**(8): p. 687-690.
109. Liang, H.P., L.J. Wan, C.L. Bai, and L. Jiang, *Gold hollow nanospheres: Tunable surface plasmon resonance controlled by interior-cavity sizes.* Journal of Physical Chemistry B, 2005. **109**(16): p. 7795-7800.
110. Haynes, C.L. and R.P. Van Duyne, *Nanosphere lithography: A versatile nanofabrication tool for studies of size-dependent nanoparticle optics.* Journal of Physical Chemistry B, 2001. **105**(24): p. 5599-5611.
111. Jensen, T.R., M.D. Malinsky, C.L. Haynes, and R.P. Van Duyne, *Nanosphere lithography: Tunable localized surface plasmon resonance spectra of silver nanoparticles.* Journal of Physical Chemistry B, 2000. **104**(45): p. 10549-10556.
112. Hicks, E.M., X.Y. Zhang, S.L. Zou, O. Lyandres, K.G. Spears, G.C. Schatz, and R.P. Van Duyne, *Plasmonic properties of film over nanowell surfaces fabricated by nanosphere lithography.* Journal of Physical Chemistry B, 2005. **109**(47): p. 22351-22358.
113. De Jesus, M.A., K.S. Giesfeldt, J.M. Oran, N.A. Abu-Hatab, N.V. Lavrik, and M.J. Sepaniak, *Nanofabrication of densely packed metal-polymer arrays for surface-enhanced Raman spectrometry.* Applied Spectroscopy, 2005. **59**(12): p. 1501-1508.
114. Alvarez-Puebla, R., B. Cui, J.P. Bravo-Vasquez, T. Veres, and H. Fenniri, *Nanoimprinted SERS-active substrates with tunable surface plasmon resonances.* Journal of Physical Chemistry C, 2007. **111**(18): p. 6720-6723.

115. Gupta, R., M.J. Dyer, and W.A. Weimer, *Preparation and characterization of surface plasmon resonance tunable gold and silver films.* Journal of Applied Physics, 2002. **92**(9): p. 5264-5271.
116. You, J.B., X.W. Zhang, Y.M. Fan, S. Qu, and N.F. Chen, *Surface plasmon enhanced ultraviolet emission from ZnO films deposited on Ag/Si(001) by magnetron sputtering.* Applied Physics Letters, 2007. **91**(23).
117. Nieuwenh.Jm and H.B. Haanstra, *Microfractography of Thin Films.* Philips Technical Review, 1966. **27**(3-4): p. 87-&.
118. Tait, R.N., T. Smy, and M.J. Brett, *Modeling and Characterization of Columnar Growth in Evaporated-Films.* Thin Solid Films, 1993. **226**(2): p. 196-201.
119. Kennedy, S.R. and M.J. Brett, *Advanced techniques for the fabrication of square spiral photonic crystals by glancing angle deposition.* Journal of Vacuum Science & Technology B, 2004. **22**(3): p. 1184-1190.
120. Liu, F., M.T. Umlor, L. Shen, J. Weston, W. Eads, J.A. Barnard, and G.J. Mankey, *The growth of nanoscale structured iron films by glancing angle deposition.* Journal of Applied Physics, 1999. **85**(8): p. 5486-5488.
121. Robbie, K. and M.J. Brett, *Sculptured thin films and glancing angle deposition: Growth mechanics and applications.* Journal of Vacuum Science & Technology a-Vacuum Surfaces and Films, 1997. **15**(3): p. 1460-1465.
122. Robbie, K., J.C. Sit, and M.J. Brett, *Advanced techniques for glancing angle deposition.* Journal of Vacuum Science & Technology B, 1998. **16**(3): p. 1115-1122.
123. Zhao, Y.P., D.X. Ye, G.C. Wang, and T.M. Lu, *Novel nano-column and nano-flower arrays by glancing angle deposition.* Nano Letters, 2002. **2**(4): p. 351-354.
124. Messier, R., T. Gehrke, C. Frankel, V.C. Venugopal, W. Otano, and A. Lakhtakia, *Engineered sculptured nematic thin films.* Journal of Vacuum Science & Technology a-Vacuum Surfaces and Films, 1997. **15**(4): p. 2148-2152.
125. Zhou, C.M. and D. Gall, *Growth competition during glancing angle deposition of nanorod honeycomb arrays.* Applied Physics Letters, 2007. **90**(9).
126. Zhao, Y.-P., D.-X. Ye, P.-I. Wang, G.-C. Wang, and T.-M. Lu, *Fabrication of Si Nanocolumns and Si Square Spirals on Self-Assembled Monolayer Colloid Substrates.* International Journal of Nanoscience, 2002. **1**(1).
127. Karabacak, T., J.P. Singh, Y.P. Zhao, G.C. Wang, and T.M. Lu, *Scaling during shadowing growth of isolated nanocolumns.* Physical Review B, 2003. **68**(12).
128. McMichael, R.D., C.G. Lee, J.E. Bonevich, P.J. Chen, W. Miller, and W.F. Egelhoff, *Strong anisotropy in thin magnetic films deposited on obliquely sputtered Ta underlayers.* Journal of Applied Physics, 2000. **88**(6): p. 3561-3564.
129. Lintymer, J., J. Gavoille, N. Martin, and J. Takadoum, *Glancing angle deposition to modify microstructure and properties of sputter deposited chromium thin films.* Surface & Coatings Technology, 2003. **174**: p. 316-323.
130. Fan, J.G. and Y.P. Zhao, *Direct deposition of aligned nanorod array onto cylindrical objects.* Journal of Vacuum Science & Technology B, 2005. **23**(3): p. 947-953.
131. Kesapragada, S.V. and D. Gall, *Two-component nanopillar arrays grown by Glancing Angle Deposition.* Thin Solid Films, 2006. **494**(1-2): p. 234-239.
132. Yao, S.W., Z.X. Song, and H.Z. Wang, *Fabrication and magnetic properties of Co/Cu multilayer nanowire arrays.* Acta Physico-Chimica Sinica, 2007. **23**(8): p. 1306-1310.

133. He, Y.P., J.X. Fu, Y. Zhang, Y.P. Zhao, L.J. Zhang, A.L. Xia, and J.W. Cai, *Multilayered Si/Ni nanosprings and their magnetic properties.* Small, 2007. **3**(1): p. 153-160.
134. Y.-P. Zhao, G.-C.W., and T.-M. Lu *Characterization of Amorphous and Crystalline Rough Surface --Principles and Applications* Experimental Methods in the Physical Sciences. 2001: Academic Press.
135. Burda, C., X.B. Chen, R. Narayanan, and M.A. El-Sayed, *Chemistry and properties of nanocrystals of different shapes.* Chemical Reviews, 2005. **105**(4): p. 1025-1102.
136. Rodriguez-Gonzalez, B., A. Burrows, M. Watanabe, C.J. Kiely, and L.M.L. Marzan, *Multishell bimetallic AuAg nanoparticles: synthesis, structure and optical properties.* Journal of Materials Chemistry, 2005. **15**(17): p. 1755-1759.
137. Uwe Kreibig, M.V., *Optical properties of metal clusters* 1995: Berlin ; New York : Springer.
138. Barbillon, G., J.L. Bijeon, J. Plain, M.L. de la Chapelle, P.M. Adam, and P. Royer, *Electron beam lithography designed chemical nanosensors based on localized surface plasmon resonance.* Surface Science, 2007. **601**(21): p. 5057-5061.
139. Gish, D.A., F. Nsiah, M.T. McDermott, and M.J. Brett, *Localized surface plasmon resonance biosensor using silver nanostructures fabricated by glancing angle deposition.* Analytical Chemistry, 2007. **79**(11): p. 4228-4232.
140. Barbillon, G., J.L. Bijeon, J. Plain, M.L. de la Chapelle, P.M. Adam, and P. Royer, *Biological and chemical gold nanosensors based on localized surface plasmon resonance.* Gold Bulletin, 2007. **40**(3): p. 240-244.
141. Endo, T., K. Kerman, N. Nagatani, and E. Tamiya, *Excitation of localized surface plasmon resonance using a core-shell structured nanoparticle layer substrate and its application for label-free detection of biomolecular interactions.* Journal of Physics-Condensed Matter, 2007. **19**(21).
142. Cheng, C.S., Y.Q. Chen, and C.J. Lu, *Organic vapour sensing using localized surface plasmon resonance spectrum of metallic nanoparticles self assemble monolayer.* Talanta, 2007. **73**(2): p. 358-365.
143. Miller, M.M. and A.A. Lazarides, *Sensitivity of metal nanoparticle surface plasmon resonance to the dielectric environment.* Journal of Physical Chemistry B, 2005. **109**(46): p. 21556-21565.
144. Campbell, T., R.K. Kalia, A. Nakano, P. Vashishta, S. Ogata, and S. Rodgers, *Dynamics of oxidation of aluminum nanoclusters using variable charge molecular-dynamics simulations on parallel computers.* Physical Review Letters, 1999. **82**(24): p. 4866-4869.
145. Amin, N.K., S.A. Nosier, M.S.M. Hassan, and G.H. Sedahmed, *The role of mass transfer in the kinetics of chemical oxidation of anthracine slurry to anthraquinone in a batch stirred tank reactor.* Chemical Engineering & Technology, 2004. **27**(2): p. 146-149.
146. Rai, A., K. Park, L. Zhou, and M.R. Zachariah, *Understanding the mechanism of aluminium nanoparticle oxidation.* Combustion Theory and Modelling, 2006. **10**(5): p. 843-859.
147. Fu, J.X., A. Collins, and Y.P. Zhao, *Optical Properties and Biosensor Application of Ultrathin Silver Films Prepared by Oblique Angle Deposition.* Journal of Physical Chemistry C, 2008. **112**(43): p. 16784-16791.
148. Haes, A.J. and R.P. Van Duyne, *A nanoscale optical blosensor: Sensitivity and selectivity of an approach based on the localized surface plasmon resonance spectroscopy of*

triangular silver nanoparticles. Journal of the American Chemical Society, 2002. **124**(35): p. 10596-10604.
149. Jung, L.S., C.T. Campbell, T.M. Chinowsky, M.N. Mar, and S.S. Yee, *Quantitative interpretation of the response of surface plasmon resonance sensors to adsorbed films.* Langmuir, 1998. **14**(19): p. 5636-5648.
150. Nath, N. and A. Chilkoti, *Label-free biosensing by surface plasmon resonance of nanoparticles on glass: Optimization of nanoparticle size.* Analytical Chemistry, 2004. **76**(18): p. 5370-5378.
151. Haes, A.J., S.L. Zou, G.C. Schatz, and R.P. Van Duyne, *A nanoscale optical biosensor: The long range distance dependence of the localized surface plasmon resonance of noble metal nanoparticles.* Journal of Physical Chemistry B, 2004. **108**(1): p. 109-116.
152. Wang, Y., F.Q. Bu, Y.J. Gu, P. Xu, X.H. Ning, S.P. Xu, B. Zhao, and W.Q. Xu, *Preparation of localized surface plasmon resonance sensing film with gold colloid by electrostatic assembly.* Chemical Journal of Chinese Universities-Chinese, 2008. **29**(8): p. 1539-1543.
153. Zhou, Y., H. Xu, A.B. Dahlin, J. Vallkil, C.A.K. Borrebaeck, C. Wingren, B. Liedberg, and F. Hook, *Quantitative interpretation of gold nanoparticle-based bioassays designed for detection of immunocomplex formation.* Biointerphases, 2007. **2**(1): p. 6-15.
154. Haes, A.J. and R.P. Van Duyne, *A unified view of propagating and localized surface plasmon resonance biosensors.* Analytical and Bioanalytical Chemistry, 2004. **379**(7-8): p. 920-930.
155. Choy, T.C., *Effective medium theory : principles and applications*. International series of monographs on physics 1999: Oxford [England] : Clarendon Press ; New York : Oxford University Press.
156. Piehler, J., A. Brecht, and G. Gauglitz, *Affinity detection of low molecular weight analytes.* Analytical Chemistry, 1996. **68**(1): p. 139-143.
157. Ozkumur, E., J.W. Needham, D.A. Bergstein, R. Gonzalez, M. Cabodi, J.M. Gershoni, B.B. Goldberg, and M.S. Unlu, *Label-free and dynamic detection of biomolecular interactions for high-throughput microarray applications.* Proceedings of the National Academy of Sciences of the United States of America, 2008. **105**(23): p. 7988-7992.
158. Mackay, T.G. and A. Lakhtakia, *A limitation of the Bruggeman formalism for homogenization.* Optics Communications, 2004. **234**(1-6): p. 35-42.
159. Arai, T., P.K.R. Kumar, C. Rockstuhl, K. Awazu, and J. Tominaga, *An optical biosensor based on localized surface plasmon resonance of silver nanostructured films.* Journal of Optics a-Pure and Applied Optics, 2007. **9**(7): p. 699-703.
160. Kurihara, K., K. Nakamura, and K. Suzuki, *Asymmetric SPR sensor response curve-fitting equation for the accurate determination of SPR resonance angle.* Sensors and Actuators B-Chemical, 2002. **86**(1): p. 49-57.
161. Knoesen, A., M.G. Moharam, and T.K. Gaylord, *Electromagnetic Propagation at Interfaces and in Waveguides in Uniaxial Crystals.* Applied Physics B, 1985. **38**: p. 171-178.
162. Smith, G.B., *Effective Medium Theory and Angular-Dispersion of Optical-Constants in Films with Oblique Columnar Structure.* Optics Communications, 1989. **71**(5): p. 279-284.
163. Smith, G.B., *Theory of Angular Selective Transmittance in Oblique Columnar Thin-Films Containing Metal and Voids.* Applied Optics, 1990. **29**(25): p. 3685-3693.

164. Jen, Y.J. and C.C. Lee, *Reflection and transmission phenomena of waves propagating between an isotropic medium and an arbitrarily oriented anisotropic medium.* Optics Letters, 2001. **26**(4): p. 190-192.
165. Mendozagalvan, A., G. Martinez, and J.L. Martinez, *Effective Dielectric Function Modeling of Inhomogeneous and Anisotropic Silver Films.* Physica A, 1994. **207**(1-3): p. 365-371.
166. Sharma, A.K. and B.D. Gupta, *Absorption-based fiber optic surface plasmon resonance sensor: a theoretical evaluation.* Sensors and Actuators B-Chemical, 2004. **100**(3): p. 423-431.
167. Liu, Y.J. and Y.P. Zhao, *Simple model for surface-enhanced Raman scattering from tilted silver nanorod array substrates.* Physical Review B, 2008. **78**(7).

APPENDIX A

ABSORPTION EFFICIENCY OF METAL SPHERE BY MIE THEORY

Let us consider a homogeneous and isotropic sphere of radius *a*, which is illuminated by an arbitrarily polarized monochromatic wave. The field inside the sphere is denoted by ($\vec{E}_1, \vec{H}_1$); the field ($\vec{E}_2, \vec{H}_2$) outside the sphere is the superposition of the incident fields ($\vec{E}_i, \vec{H}_i$) and the scattered field ($\vec{E}_s, \vec{H}_s$):

$$\vec{E}_2 = \vec{E}_i + \vec{E}_s, \tag{A.1}$$

$$\vec{H}_2 = \vec{H}_i + \vec{H}_s, \tag{A.2}$$

where

$$\vec{E}_i = \vec{E}_0 \exp(i\vec{k} \cdot \vec{x} - i\omega t), \tag{A.3}$$

$$\vec{H}_i = \vec{H}_0 \exp(i\vec{k} \cdot \vec{x} - i\omega t), \tag{A.4}$$

and $\vec{k}$ is the wave vector in surrounding medium outside of the sphere. The fields should satisfy the Maxwell equations:

$$\nabla \cdot \vec{E} = 0, \tag{A.5}$$

$$\nabla \times \vec{E} = i\omega\mu\vec{H}, \tag{A.6}$$

$$\nabla \cdot \vec{H} = 0, \tag{A.7}$$

$$\nabla \times \vec{H} = i\omega\varepsilon\vec{E}. \tag{A.8}$$

Combining these equations give the vector wave equations:

$$\nabla^2\vec{E} + k^2\vec{E} = 0\,, \tag{A.9}$$

$$\nabla^2\vec{H} + k^2\vec{H} = 0\,. \tag{A.10}$$

To find the expressions for the fields, first we construct two vector functions

$$\vec{M} = \nabla \times (\vec{r}\varphi) \text{ and } \nabla \cdot \vec{M} = 0\,, \tag{A.11}$$

$$\vec{N} = \frac{\nabla \times \vec{M}}{k}\,, \tag{A.12}$$

where $\vec{r}$ is a vector from the origin of the sphere to a point outside the sphere and φ is a scalar function. If

$$\nabla^2\varphi + k^2\varphi = 0\,, \tag{A.13}$$

we have

$$\nabla^2\vec{M} + k^2\vec{M} = 0\,, \tag{A.14}$$

$$\nabla^2\vec{N} + k^2\vec{N} = 0\,, \tag{A.15}$$

which satisfy the vector wave equation. To obtain the expressions for $\vec{M}$ and $\vec{N}$, we need solve the equation (A.13). In spherical polar coordinates (Figure A.1), equation can be written as

$$\frac{1}{r^2}\frac{\partial}{\partial r}(r^2\frac{\partial\varphi}{\partial r}) + \frac{1}{r^2\sin\theta}\frac{\partial}{\partial\theta}(\sin\theta\frac{\partial\varphi}{\partial\theta}) + \frac{1}{r^2\sin\theta}\frac{\partial^2\varphi}{\partial\phi^2} + k^2\varphi = 0\,. \tag{A.16}$$

Letting the generating function $\varphi(r,\theta,\phi) = R(r)\Theta(\theta)\Phi(\phi)$ yields three separating equations:

$$\frac{d^2\Phi}{d\phi^2} + m^2\Phi = 0\,, \tag{A.17}$$

$$\frac{1}{\sin\theta}\frac{d}{d\theta}(\sin\theta\frac{d\Theta}{d\theta}) + [n(n+1) - \frac{m^2}{\sin^2\theta}]\Theta = 0\,, \tag{A.18}$$

$$\frac{d}{dr}(r^2\frac{dR}{dr}) + [k^2r^2 - n(n+1)]R = 0\,, \tag{A.19}$$

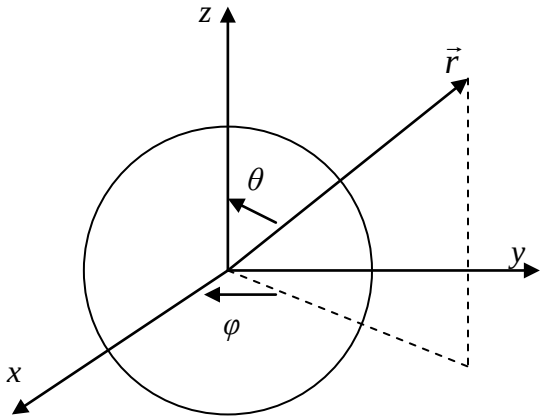

Figure A.1 Spherical polar coordinates with the origin at the center of the sphere.

where *m* and *n* are constants. By solving the three equations, we obtain

$$\varphi_{emn} = \cos m\phi P_n^m(\cos\theta) z_n(kr), \tag{A.20}$$

$$\varphi_{omn} = \sin m\phi P_n^m(\cos\theta) z_n(kr), \tag{A.21}$$

where $m = 0,1, \ldots, n = m, m+1, \ldots$, the subscripts *e* and *o* denote even and odd. $P_n^m(\cos\theta)$ is the associated Legendre function and z_n is any of the four spherical Bessel functions:

$$j_n(\rho) = \sqrt{\frac{\pi}{2\rho}} J_{n+\frac{1}{2}}(\rho), \tag{A.22}$$

$$y_n(\rho) = \sqrt{\frac{\pi}{2\rho}} Y_{n+\frac{1}{2}}(\rho), \tag{A.23}$$

$$h_n^{(1)}(\rho) = j_n(\rho) + iy_n(\rho), \tag{A.24}$$

$$h_n^{(2)}(\rho) = j_n(\rho) - iy_n(\rho), \tag{A.25}$$

$$\rho = kr, \tag{A.26}$$

where $J_{n+\frac{1}{2}}$ and $Y_{n+\frac{1}{2}}$ are Bessel functions of first and second kinds. Therefore, the vector spherical harmonics generated by φ_{emn} and φ_{omn} are

$$\vec{M}_{emn} = \nabla \times (\vec{r}\varphi_{emn}), \tag{A.27}$$

$$\vec{M}_{omn} = \nabla \times (\vec{r}\varphi_{omn}), \tag{A.28}$$

$$\vec{N}_{emn} = \frac{\nabla \times \vec{M}_{emn}}{k}, \tag{A.29}$$

$$\vec{N}_{omn} = \frac{\nabla \times \vec{M}_{omn}}{k}. \tag{A.30}$$

Then suppose a plane *x*-polarized wave illuminates the sphere, and the permeability of the particle and the surrounding medium are the same, the incident electric field is

$$\vec{E}_i = E_0 e^{ikr\cos\theta}\hat{e}_x. \tag{A.31}$$

With great difficulties, the incident fields can be expanded as a series of the above vector spherical harmonics:

$$\vec{E}_i = E_0 \sum_{n=1}^{\infty} i^n \frac{2n+1}{n(n+1)} (\vec{M}_{o1n}^{(1)} - i\vec{N}_{e1n}^{(1)}), \tag{A.32}$$

$$\vec{H}_i = \frac{-k}{\omega\mu} E_0 \sum_{n=1}^{\infty} i^n \frac{2n+1}{n(n+1)} (\vec{M}_{e1n}^{(1)} - i\vec{N}_{o1n}^{(1)}). \tag{A.33}$$

The superscript (1) denotes the generating function is specified by j_n. Similarly,

$$\vec{E}_1 = E_0 \sum_{n=1}^{\infty} i^n \frac{2n+1}{n(n+1)} (c_n\vec{M}_{o1n}^{(1)} - id_n\vec{N}_{e1n}^{(1)}), \tag{A.34}$$

$$\vec{H}_1 = \frac{-k_1}{\omega\mu_1} E_0 \sum_{n=1}^{\infty} i^n \frac{2n+1}{n(n+1)} (d_n\vec{M}_{e1n}^{(1)} + ic_n\vec{N}_{o1n}^{(1)}), \tag{A.35}$$

where c_n and d_n are coefficients.

At the boundary between the sphere and the surrounding medium, the tangent components of the field should be continuous:

$$(\vec{E}_i + \vec{E}_s - \vec{E}_1) \times \hat{e}_r = (\vec{H}_i + \vec{H}_s - \vec{H}_1) \times \hat{e}_r = 0 . \tag{A.36}$$

The expansion of the scattered field is therefore

$$\vec{E}_s = E_0 \sum_{n=1}^{\infty} i^n \frac{2n+1}{n(n+1)} (i a_n \vec{N}_{e1n}^{(3)} - b_n \vec{M}_{o1n}^{(3)}), \tag{A.37}$$

$$\vec{H}_s = \frac{k}{\omega\mu} E_0 \sum_{n=1}^{\infty} i^n \frac{2n+1}{n(n+1)} (i b_n \vec{N}_{o1n}^{(3)} + a_n \vec{M}_{e1n}^{(3)}) . \tag{A.38}$$

The superscript (3) denotes the generating function is specified by $h_n^{(1)}$. And a_n and b_n are scattering coefficients.

From the expansions (A.32) - (A.35), (A.37) – (A.38), the boundary conditions (A.36) in component form can be eventually written as the following four equations:

$$j_n(mx)c_n + h_n^{(1)}(x)b_n = j_n(x), \tag{A.39}$$

$$[mxj_n(mx)]'c_n + [xh_n^{(1)}(x)]'b_n = [xj_n(x)]', \tag{A.40}$$

$$mj_n(mx)d_n + h_n^{(1)}(x)a_n = j_n(x), \tag{A.41}$$

$$[mxj_n(mx)]'d_n + m[xh_n^{(1)}(x)]'a_n = m[xj_n(x)]', \tag{A.42}$$

where the prime indicates differentiation with respect to the argument in parentheses and

$$x = ka = \frac{2\pi\sqrt{\varepsilon}a}{\lambda}, \; m = \frac{k_1}{k} = \frac{\sqrt{\varepsilon_1}}{\sqrt{\varepsilon}}, \tag{A.43}$$

where k_1 is the wave vector inside the sphere, ε_1 and ε are dielectric functions inside and outside the sphere, respectively.

By solving above four equations, the scattering coefficients can be obtained as follows:

$$a_n = \frac{m\psi_n(mx)\psi_n^{'}(x) - \psi_n(x)\psi_n^{'}(mx)}{m\psi_n(mx)\xi_n^{'}(x) - \xi_n(x)\psi_n^{'}(mx)}, \tag{A.44}$$

$$b_n = \frac{\psi_n(mx)\psi_n^{'}(x) - m\psi_n(x)\psi_n^{'}(mx)}{\psi_n(mx)\xi_n^{'}(x) - m\xi_n(x)\psi_n^{'}(mx)}, \tag{A.45}$$

where ψ_n and ξ_n are Riccati-Bessel functions:

$$\psi_n(\rho) = \rho j_n(\rho),\ \xi_n(\rho) = \rho h_n^{(1)}(\rho). \tag{A.46}$$

So far, we have had all the expressions for the fields inside and outside the sphere. We will obtain the cross sections by investigating the energy rate going into and out of the sphere. The energy extinction rate W_{ext} is the sum of the energy absorption rate W_a and the energy scattering rate W_s:

$$W_{ext} = W_a + W_s = \frac{1}{2}\mathrm{Re}\int_0^{2\pi}\int_0^{\pi}(E_{i\phi}H_{s\theta}^{*} - E_{i\theta}H_{s\phi}^{*} - E_{s\theta}H_{i\phi}^{*} + E_{s\phi}H_{i\theta}^{*})r^2\sin\theta d\theta d\phi, \tag{A.47}$$

$$W_s = \frac{1}{2}\mathrm{Re}\int_0^{2\pi}\int_0^{\pi}(E_{s\theta}H_{s\phi}^{*} - E_{s\phi}H_{s\theta}^{*})r^2\sin\theta d\theta d\phi. \tag{A.48}$$

It follows that the extinction cross section is

$$C_{ext} = \frac{W_{ext}}{I_i} = \frac{2\pi}{k^2}\sum_{n=1}^{\infty}(2n+1)\,\mathrm{Re}\{a_n + b_n\}. \tag{A.49}$$

Similarly, the scattering cross section is

$$C_{sca} = \frac{W_s}{I_i} = \frac{2\pi}{k^2}\sum_{n=1}^{\infty}(2n+1)(|a_n|^2 + |b_n|^2), \tag{A.50}$$

where I_i is the incident irradiance. For a very small sphere, $x << 1$, we only retain the first few terms in the scattering coefficients a_n and b_n:

$$a_1 = -\frac{i2x^3}{3}\frac{m^2-1}{m^2+2} - \frac{i2x^5}{3}\frac{(m^2-2)(m^2-1)}{(m^2+2)^2} + \frac{4x^6}{9}\left(\frac{m^2-1}{m^2+2}\right)^2 + O(x^7), \tag{A.51}$$

$$b_1 = -\frac{ix^5}{45}(m^2 - 1) + O(x^7), \tag{A.52}$$

$$a_2 = -\frac{ix^5}{15}\frac{m^2 - 1}{2m^2 + 3} + O(x^7), \tag{A.53}$$

$$b_2 = O(x^7). \tag{A.54}$$

To terms of order x^4, the extinction and scattering efficiencies are

$$Q_{ext} = \frac{C_{ext}}{\pi a^2} = 4x\,\mathrm{Im}\{\frac{m^2 - 1}{m^2 + 2}[1 + \frac{x^2}{15}(\frac{m^2 - 1}{m^2 + 2})\frac{m^4 + 27m^2 + 38}{2m^2 + 3}]\} + \frac{8}{3}x^4\,\mathrm{Re}\{(\frac{m^2 - 1}{m^2 + 2})^2\}, \tag{1.55}$$

$$Q_{sca} = \frac{C_{sca}}{\pi a^2} = \frac{8}{3}x^4\left|\frac{m^2 - 1}{m^2 + 2}\right|^2. \tag{A.56}$$

The absorption efficiency

$$Q_{abs} = Q_{ext} - Q_{sca} = 4x\,\mathrm{Im}\{\frac{m^2 - 1}{m^2 + 2}\}[1 - \frac{4}{3}x^3\,\mathrm{Im}\{\frac{m^2 - 1}{m^2 + 2}\}^2]. \tag{A.57}$$

For a sufficiently small x, the absorption efficiency can be simplified as

$$Q_{abs} = 4x\,\mathrm{Im}\{\frac{m^2 - 1}{m^2 + 2}\} = \frac{24\pi a\varepsilon^{3/2}}{\lambda}\frac{\varepsilon_i}{(\varepsilon_r + 2\varepsilon)^2 + \varepsilon_i^2}, \tag{A.58}$$

$$\varepsilon_1 = \varepsilon_r + i\varepsilon_i. \tag{A.59}$$

APPENDIX B

MAXWELL-GARNETT THEORY AND BRUGGEMAN'S THEORY

A brief introduction of effective medium theories, Maxwell-Garnett (MG) theory and Bruggeman (BR) theory, will be outlined in the following. The MG theory applies to particles embedded in a host while the BR theory presumes structural equivalence between two constituents, as shown in Figure B.1.

In MG theory, there are particles with dielectric constant ε_1 imbedded in a host with the dielectric constant ε_0, we are trying to find out the effective dielectric constant ε of this composite system (Figure B.1(a)). For a particle embedded in the host, it experiences a local field $\vec{E}_{loc}$ and Lorentz assumed that

$$\vec{E}_{loc} = \vec{E} + \frac{1}{3\varepsilon_0}\vec{P}, \tag{B.1}$$

where $\vec{E}$ is the macroscopic field and $\vec{P}$ is the polarization. The dipole moment of the particle $\vec{p}$ is given by

$$\vec{p} = \varepsilon_0 \alpha \vec{E}_{loc}, \tag{B.2}$$

where α is the polarizability. Then the polarization $\vec{P}$ is

$$\vec{P} = \sum_j N_j \vec{p}_j = \sum_j N_j \varepsilon_0 \alpha_j \vec{E}_{loc}(j), \tag{B.3}$$

where the sum is over all particles *j*, and N_j is the number of particles per unit volume. Aussuming that the local field is identical for all particles, we can substitute equation (B.1) into (B.3):

$$\vec{P} = (\varepsilon_0 \vec{E} + \frac{1}{3}\vec{P})\sum_j N_j \alpha_j \,. \tag{B.4}$$

By solving for the polarization $\vec{P}$, we obtain the dielectric susceptibility

$$\chi = \frac{\vec{P}}{\varepsilon_0 \vec{E}} = \frac{\sum_j N_j \alpha_j}{1 - \frac{1}{3}\sum_j N_j \alpha_j}. \tag{B.5}$$

In terms of the dielectric constant $\varepsilon = \varepsilon_0(1+\chi)$, equation (B.5) can be rearranged as

$$\frac{\varepsilon - \varepsilon_0}{\varepsilon + 2\varepsilon_0} = \frac{1}{3}\sum_j N_j \alpha_j \,. \tag{B.6}$$

For a spherical particle with dielectric constant ε_1 and radius *a*, its dielectric susceptibility is

$$\alpha = 4\pi\left(\frac{\varepsilon_1 - 1}{\varepsilon_1 + 2}\right)a^3 . \tag{B.7}$$

Substituting equation (B.7) into (B.6) gives the Maxwell-Garnett formula:

$$\frac{\varepsilon - \varepsilon_0}{\varepsilon + 2\varepsilon_0} = \eta_1\left(\frac{\varepsilon_1 - 1}{\varepsilon_1 + 2}\right), \tag{B.8}$$

where $\eta_1 = \frac{4\pi}{3}a^3\sum_j N_j$ is the volume fraction of particles. Therefore, by solving equation (B.8), the effective dielectric constant ε of this composite system can be calculated.

However, when using Maxwell-Garnett formula, we have to choose the host and the inclusions, and different choices do not yield the same results for the effective dielectric constant ε. Also, in this theory, the effective dielectric constant reflects the host's property even the volume fraction of the inclusions is high, which means a conductor remains a conductor until the

volume fraction of the insulators becomes 1. Therefore, when the volume fraction of the inclusions is high, this formula can not give the correct result.

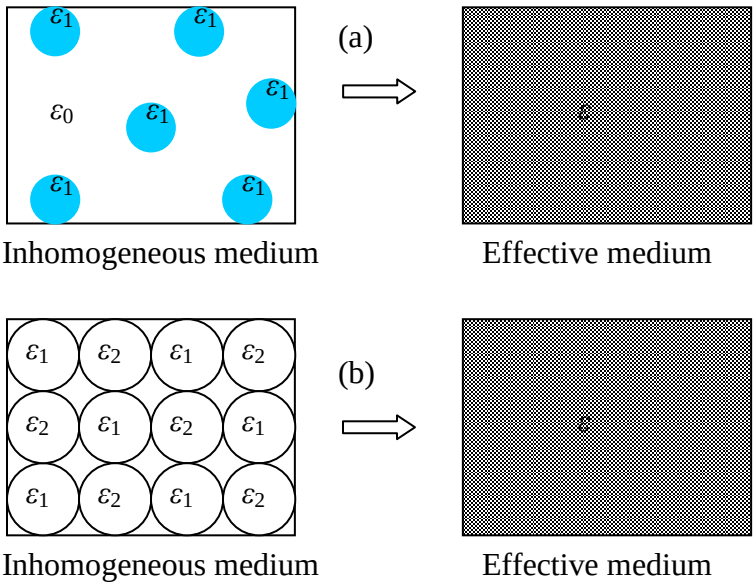

Figure B.1 Illustration of (a) Maxwell-Garnett theory and (b) Bruggeman theory.

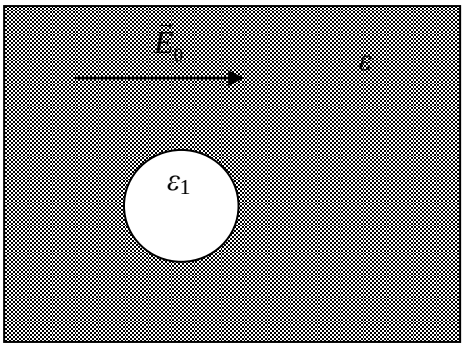

Figure B.2 A particle with dielectric constant ε_1 and radius a in a binary composite.

Bruggeman made an improvement to the Maxwell-Garnett theory by considering a binary system with fractions η_1 of dielectric constant ε_1 and η_2 of dielectric constant ε_2 respectively, as shown in Figure B.1(b). In this system, the two components are equivalent. To calculate the effective dielectric constant ε, we first exam a spherical inclusion of radius a and dielectric

constant ε_1 in the homogeneous effective medium, as illustrated in Figure B.2. Far from this inclusion, the electric field is a constant $\vec{E}_0$, then the potential inside the sphere can be calculated as:

$$\Psi_{in} = -\left(\frac{3\varepsilon}{\varepsilon_1 + 2\varepsilon}\right) E_0 r\cos\theta\,. \tag{B.9}$$

The electric field inside the sphere therefore is

$$E_{in} = \left(\frac{3\varepsilon}{\varepsilon_1 + 2\varepsilon}\right) E_0\,. \tag{B.10}$$

With these expressions we can now calculate the electric flux deviation due to the polarization by the inclusion. For a sphere, we take the cross section normal to the direction of $\vec{E}_0$ and its area is πa^2. Then the flux deviation $\Delta\Phi_1$ is

$$\Delta\Phi_1 = \pi a^2 \varepsilon_1 E_{in} - \pi a^2 \varepsilon E_0 = 2\pi a^2 \varepsilon E_0 \left(\frac{\varepsilon_1 - \varepsilon}{\varepsilon_1 + 2\varepsilon}\right). \tag{B.11}$$

Similarly, for the particle of radius *a* and dielectric constant ε_1 in the homogeneous effective medium, we have

$$\Delta\Phi_2 = 2\pi a^2 \varepsilon E_0 \left(\frac{\varepsilon_2 - \varepsilon}{\varepsilon_2 + 2\varepsilon}\right). \tag{B.12}$$

Bruggeman hypothesized that there should be zero average flux deviations in this system, i.e. [1]

$$\eta_1 \Delta\Phi_1 + \eta_2 \Delta\Phi_2 = 0\,, \tag{B.13}$$

Then equation (B.13) can be written as

$$\eta_1 \left(\frac{\varepsilon_1 - \varepsilon}{\varepsilon_1 + 2\varepsilon}\right) + \eta_2 \left(\frac{\varepsilon_2 - \varepsilon}{\varepsilon_2 + 2\varepsilon}\right) = 0\,. \tag{B.14}$$

This is the Bruggeman formula. Both MG and BR theories can be applied to the inclusions with spheroid shape, which is used in chapter 4.

APPENDIX C

FRESNEL EQUATION OF THREE-LAYER STRUCTURE CONTAINING AN ANISOTROPIC LAYER

Consider a three-layer structure containing an anisotropic layer as shown in Figure C.1. To simplify the problem, the notations might be different from those in chapter 4.

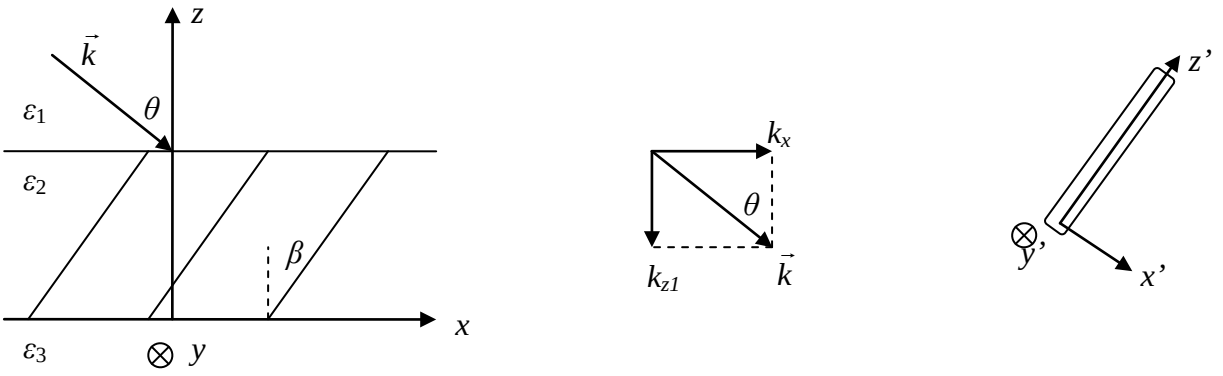

Figure C.1 Illustration of three-layer structure containing an anisotropic layer.

In the medium with a dielectric constant ε_1, we have

$$k_x = k_0\sqrt{\varepsilon_1}\sin\theta\,, \tag{C.1}$$

$$k_{1z} = k_0\sqrt{\varepsilon_1}\cos\theta\,, \tag{C.2}$$

$$k_0 = \frac{w}{c} = w\sqrt{\mu_o\varepsilon_0}\,, \tag{C.3}$$

Where the *x*-component k_x of the wave vector $\vec{k}$ is conserved in all the layers. Suppose the incident light is a plane wave:

$$\vec{E} = \vec{E}_0 e^{i(\vec{k}\cdot\vec{r}-wt)}, \tag{C.4}$$

$$\vec{B} = \vec{B}_0 e^{i(\vec{k}\cdot\vec{r}-wt)}. \tag{C.5}$$

Appling Maxwell's equations

$$\nabla \times \vec{E} + \frac{\partial \vec{B}}{\partial t} = 0, \tag{C.6}$$

$$\nabla \times \vec{H} = \frac{\partial \vec{D}}{\partial t}, \tag{C.7}$$

$$\nabla \cdot \vec{D} = 0, \tag{C.8}$$

$$\nabla \cdot \vec{B} = 0, \tag{C.9}$$

to equations (C.4) and (C.5) gives:

$$\vec{k} \times \vec{E} = \omega \mu_0 \vec{H}, \tag{C.10}$$

$$\vec{k} \times \vec{H} = -\omega \varepsilon_0 \varepsilon \vec{E}, \tag{C.11}$$

$$\vec{k} \cdot \varepsilon \vec{E} = 0, \tag{C.12}$$

$$\vec{k} \cdot \vec{H} = 0. \tag{C.13}$$

The dielectric function ε_2 of the anisotropic layer is a tensor. In the coordinate *x'y'z'*,

$$\varepsilon_2' = \begin{pmatrix} \varepsilon_{x'} & 0 & 0 \\ 0 & \varepsilon_{y'} & 0 \\ 0 & 0 & \varepsilon_{z'} \end{pmatrix}, \tag{C.14}$$

and

$$\varepsilon_{x'} = \varepsilon_{y'}. \tag{C.15}$$

In the coordinate *xyz*,

$$\varepsilon_2 = \begin{pmatrix} \varepsilon_{xx} & \varepsilon_{xy} & \varepsilon_{xz} \\ \varepsilon_{yx} & \varepsilon_{yy} & \varepsilon_{yz} \\ \varepsilon_{zx} & \varepsilon_{zy} & \varepsilon_{zz} \end{pmatrix}$$

$$= \begin{pmatrix} \cos\beta & 0 & \sin\beta \\ 0 & 1 & 0 \\ -\sin\beta & 0 & \cos\beta \end{pmatrix} \begin{pmatrix} \varepsilon_{x'} & 0 & 0 \\ 0 & \varepsilon_{y'} & 0 \\ 0 & 0 & \varepsilon_{z'} \end{pmatrix} \begin{pmatrix} \cos\beta & 0 & -\sin\beta \\ 0 & 1 & 0 \\ \sin\beta & 0 & \cos\beta \end{pmatrix} \quad . \qquad \text{(C.16)}$$

$$= \begin{pmatrix} \varepsilon_{x'}\cos^2\beta + \varepsilon_{z'}\sin^2\beta & 0 & -\varepsilon_{x'}\sin\beta\cos\beta + \varepsilon_{z'}\sin\beta\cos\beta \\ 0 & \varepsilon_{y'} & 0 \\ -\varepsilon_{x'}\sin\beta\cos\beta + \varepsilon_{z'}\sin\beta\cos\beta & 0 & \varepsilon_{x'}\sin^2\beta + \varepsilon_{z'}\cos^2\beta \end{pmatrix}$$

Let $\hat{c}$ is a unit vector along *z'*, then in the coordinate *xyz*:

$$\hat{c} = c_x\hat{x} + c_y\hat{y} + c_z\hat{z}\,, \quad |\hat{c}|^2 = 1, \qquad \text{(C.17)}$$

where

$$c_x = \sin\beta\,,\ c_y = 0\,,\ c_z = \cos\beta\,. \qquad \text{(C.18)}$$

It is easy to write the components of ε_2 as

$$\begin{aligned} \varepsilon_{ii} &= \varepsilon_{x'} + (\varepsilon_{z'} - \varepsilon_{x'})c_i^{\,2} \\ \varepsilon_{ij} &= (\varepsilon_{z'} - \varepsilon_{x'})c_i c_j \end{aligned}\ , \ i,j = x, y, z. \qquad \text{(C.19)}$$

Decompose equations (C.10) – (C.13) into the coordinate *x'y'z'* and let *x'*→1, *y'*→2, *z'*→3 for simplicity:

$$k_2E_3 - k_3E_2 = \omega\mu_0H_1, \qquad \text{(C.20)}$$

$$k_3E_1 - k_1E_3 = \omega\mu_0H_2\,, \qquad \text{(C.21)}$$

$$k_1E_2 - k_2E_1 = \omega\mu_0H_3\,, \qquad \text{(C.22)}$$

$$k_2H_3 - k_3H_2 = -\omega\varepsilon_0\varepsilon_1E_1, \qquad \text{(C.23)}$$

$$k_3H_1 - k_1H_3 = -\omega\varepsilon_0\varepsilon_1E_2\,, \qquad \text{(C.24)}$$

$$k_1H_2 - k_2H_1 = -\omega\varepsilon_0\varepsilon_1E_3\,. \qquad \text{(C.25)}$$

$$k_1\varepsilon_1 E_1 + k_2\varepsilon_2 E_2 + k_3\varepsilon_3 E_3 = 0\,, \tag{C.26}$$

$$k_1 H_1 + k_2 H_2 + k_3 H_3 = 0\,. \tag{C.27}$$

Multiplying equation (C.20) by $k_2\varepsilon_2$ gives:

$$k_2\varepsilon_2 k_3 E_2 = {k_2}^2\varepsilon_2 E_3 - \omega\mu_0 k_2\varepsilon_2 H_1\,. \tag{C.28}$$

Multiplying equation (C.21) by $k_1\varepsilon_1$ gives:

$$k_1\varepsilon_1 k_3 E_1 = {k_1}^2\varepsilon_1 E_3 + \omega\mu_0 k_1\varepsilon_1 H_2\,. \tag{C.29}$$

Substituting equations (C.28) and (C.29) into equation (C.26) gives:

$${k_1}^2\varepsilon_1 E_3 + \omega\mu_0 k_1\varepsilon_1 H_2 + {k_2}^2\varepsilon_2 E_3 - \omega\mu_0 k_2\varepsilon_2 H_1 + {k_3}^2\varepsilon_3 E_3 = 0\,. \tag{C.30}$$

Substitute equation (C.25) into (C.30) and recall $\varepsilon_1 = \varepsilon_2$:

$${k_1}^2\varepsilon_1 E_3 + {k_2}^2\varepsilon_1 E_3 + {k_3}^2\varepsilon_3 E_3 + \omega\mu_0\varepsilon_1(-\omega\varepsilon_0\varepsilon_3 E_3) = 0\,. \tag{C.31}$$

We can rewrite (C.31) as:

$$[\varepsilon_1\vec{k}\cdot\vec{k} + (\varepsilon_3 - \varepsilon_1)(\vec{k}\cdot\hat{c})^2 - {k_0}^2\varepsilon_1\varepsilon_3]E_3 = 0\,. \tag{C.32}$$

Multiplying equation (C.23) by k_2 gives:

$$k_2 k_3 H_2 = {k_2}^2 H_3 + \omega\varepsilon_0\varepsilon_1 k_2 E_1\,. \tag{C.33}$$

Multiplying equation (C.24) by k_1 gives:

$$k_1 k_3 H_1 = {k_1}^2 H_3 - \omega\varepsilon_0\varepsilon_2 k_1 E_2\,. \tag{C.34}$$

Substituting equations (C.33) and (C.34) into (C.27) gives:

$${k_1}^2 H_3 - \omega\varepsilon_0\varepsilon_1 k_1 E_2 + {k_2}^2 H_3 + \omega\varepsilon_0\varepsilon_1 k_2 E_1 + {k_3}^2 H_3 = 0\,. \tag{C.35}$$

Substituting equation (C.22) into (C.35) gives:

$$(\vec{k}\cdot\vec{k} - {k_0}^2\varepsilon_1)H_3 = 0\,. \tag{C.36}$$

One should note that

$$\vec{k}'\cdot\vec{k}' = \vec{k}\cdot\vec{k}\ ,\ \vec{k}'\cdot\hat{z}' = \vec{k}\cdot\hat{c}\ , \tag{C.37}$$

where the "prime" means the corresponding vectors in coordinate *x'y'z'*.

When the incident light is *p*-polarized,

$$E_3 \neq 0\ ,\ k_{2y} = 0\ , \tag{C.38}$$

the term in square bracket in equation (C.32) should vanish:

$$\varepsilon_1\vec{k}\cdot\vec{k} + (\varepsilon_3 - \varepsilon_1)(\vec{k}\cdot\hat{c})^2 - {k_0}^2\varepsilon_1\varepsilon_3 = 0\ . \tag{C.39}$$

Recall equation (C.19) and rewrite equation (C.39) in the coordinate *xyz*:

$$\varepsilon_1{k_x}^2 + \varepsilon_1{k_{2z}}^2 + (\varepsilon_3 - \varepsilon_1)(k_x c_x + k_{2z}c_z)^2 - {k_0}^2\varepsilon_1\varepsilon_3 = 0\ . \tag{C.40}$$

Therefore,

$$\varepsilon_1{k_x}^2 + \varepsilon_1{k_{2z}}^2 + {k_x}^2(\varepsilon_{xx} - \varepsilon_1) + {k_{2z}}^2(\varepsilon_{zz} - \varepsilon_1) + 2k_x k_{2z}\varepsilon_{xz} - {k_0}^2\varepsilon_1\varepsilon_3 = 0\ . \tag{C.41}$$

Rearranging equation (C.41) gives:

$$\varepsilon_{zz}{k_{2z}}^2 + 2k_x\varepsilon_{xz}k_{2z} + ({k_x}^2\varepsilon_{xx} - {k_0}^2\varepsilon_1\varepsilon_3) = 0\ . \tag{C.42}$$

Solve equation (C.42) and use ${\varepsilon_{xz}}^2 - \varepsilon_{xx}\varepsilon_{zz} = -\varepsilon_1\varepsilon_3$ to obtain the expression for k_z:

$$k_{2z\pm} = \frac{-k_x\varepsilon_{xz} \pm \sqrt{\varepsilon_1\varepsilon_3}\sqrt{{k_0}^2\varepsilon_{zz} - {k_x}^2}}{\varepsilon_{zz}}\ . \tag{C.43}$$

This is equation (4.12) in chapter 4. And k_{2z+} and k_{2z-} are thought of as the forward and reverse waves. The effective dielectric constant of the anisotropic layer is:

$$\begin{aligned}\varepsilon_{2\pm} &= \left(\frac{k_2}{k_0}\right)^2 = \left(\frac{k_x}{k_0}\right)^2 + \left(\frac{k_{2z\pm}}{k_0}\right)^2 \\ &= \varepsilon_1\sin^2\theta + \left[\frac{-\sqrt{\varepsilon_1}\sin\theta\,\varepsilon_{xz} \pm \sqrt{\varepsilon_{x'}\varepsilon_{z'}}\sqrt{\varepsilon_{zz} - \varepsilon_1\sin^2\theta}}{\varepsilon_{zz}}\right]^2\end{aligned}\ . \tag{C.44}$$

This is equation (4.13) in chapter 4.

Since the *z* component of the wave vector in the anisotropic layer has two solutions, k_{2z+} and k_{2z-}, the reflection of the wave vector inside the anisotropic layer is not symmetric, as shown in Figure C.2. The electric fields can be written as

$$\vec{E}_i = \hat{x}E_0 \cos\theta_i e^{i(k_{ix}x - k_{iz}z)} + \hat{z}E_0 \sin\theta_i e^{i(k_{ix}x - k_{iz}z)}, \tag{C.45}$$

$$\vec{E}_r = -\hat{x}E_0 r_{12} \cos\theta_r e^{i(k_{rx}x + k_{rz}z)} + \hat{z}E_0 r_{12} \sin\theta_r e^{i(k_{rx}x + k_{rz}z)}, \tag{C.46}$$

$$\vec{E}_t = \hat{x}E_0 t_{12} \cos\theta_t e^{i(k_{tx}x - k_{tz}z)} + \hat{z}E_0 t_{12} \sin\theta_t e^{i(k_{tx}x - k_{tz}z)}. \tag{C.47}$$

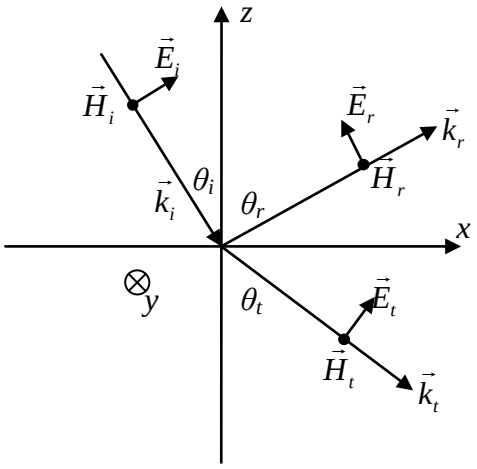

Figure C.2 Illustration of the ansymmetric reflection on the interface between an anisotropic layer and an isotropic layer. The incident light is *p*-polarized.

Recall equation (C.10), we have

$$\vec{H}_i = \hat{y}\frac{1}{\omega\mu_0}(-k_{iz}E_0 \cos\theta_i - k_{ix}E_0 \sin\theta_i)e^{i(k_{ix}x - k_{iz}z)}, \tag{C.48}$$

$$\vec{H}_r = \hat{y}\frac{1}{\omega\mu_0}(-k_{rz}E_0 r_{12} \cos\theta_r - k_{rx}E_0 r_{12} \sin\theta_r)e^{i(k_{rx}x + k_{rz}z)}, \tag{C.49}$$

$$\vec{H}_t = \hat{y}\frac{1}{\omega\mu_0}(-k_{tz}E_0 t_{12} \cos\theta_t - k_{tx}E_0 t_{12} \sin\theta_t)e^{i(k_{tx}x - k_{tz}z)}. \tag{C.50}$$

Because the tangential components of electric and magnetic fields are continuous, we have

$$\cos\theta_i - r_{12}\cos\theta_r = t_{12}\cos\theta_t\,, \tag{C.51}$$

$$-k_{iz}\cos\theta_i - k_{ix}\sin\theta_i - k_{rz}r_{12}\cos\theta_r - k_{rx}r_{12}\sin\theta_r = -k_{tz}t_{12}\cos\theta_t - k_{tx}t_{12}\sin\theta_t\,. \tag{C.52}$$

Solve the reflection coefficient r_{12} from equations (C.51) and (C.52):

$$r_{12} = \frac{-k_{iz}\cos\theta_i\cos\theta_t - k_{ix}\sin\theta_i\cos\theta_t + k_{tz}\cos\theta_i\cos\theta_t + k_{tx}\sin\theta_t\cos\theta_i}{k_{tz}\cos\theta_r\cos\theta_t + k_{tx}\sin\theta_t\cos\theta_r + k_{rz}\cos\theta_r\cos\theta_t + k_{rx}\sin\theta_r\cos\theta_t}\,. \tag{C.53}$$

Considering

$$\begin{aligned} k_{jx} &= k_j\sin\theta_j \\ k_{jz} &= k_j\cos\theta_j\,,\ j = i,\ r,\ t, \\ k_j &= k_0\sqrt{\varepsilon_j} \end{aligned} \tag{C.54}$$

equation (C.53) can be rewritten as:

$$r_{12} = \frac{\sqrt{\varepsilon_r}}{\sqrt{\varepsilon_i}}\frac{-k_{tz}\varepsilon_i + k_{iz}\varepsilon_t}{k_{rz}\varepsilon_t + k_{tz}\varepsilon_r}\,. \tag{C.55}$$

Similarly, the transmission coefficient t_{12} is:

$$t_{12} = \frac{\sqrt{\varepsilon_t}}{\sqrt{\varepsilon_i}}\frac{k_{iz}\varepsilon_r + k_{rz}\varepsilon_i}{k_{rz}\varepsilon_t + k_{tz}\varepsilon_r}\,. \tag{C.56}$$

Then consider three-layer structure A/B/C, where A and C are isotropic layers, B is an anisotropic layer with a thickness of t (Figure C.3). The notations are different from those in section C.2.1. Using equations (C.55) - (C.56) and $k_{iz} = k_{rz}$, we can write the reflection and transmission coefficients at the points on the interfaces A/B and B/C:

$$r_{AB1} = \frac{-k_{+z}\varepsilon_A + k_{iz}\varepsilon_{B+}}{k_{iz}\varepsilon_{B+} + k_{+z}\varepsilon_A}\,, \tag{C.57}$$

$$t_{AB1} = \frac{\sqrt{\varepsilon_{B+}}}{\sqrt{\varepsilon_A}}\frac{2k_{iz}\varepsilon_A}{k_{iz}\varepsilon_{B+} + k_{+z}\varepsilon_A}\,, \tag{C.58}$$

$$r_{BC2} = \frac{\sqrt{\varepsilon_{B-}}}{\sqrt{\varepsilon_{B+}}} \frac{-k_{tz}\varepsilon_{B+} + k_{+z}\varepsilon_C}{k_{-z}\varepsilon_C + k_{tz}\varepsilon_{B-}}, \tag{C.59}$$

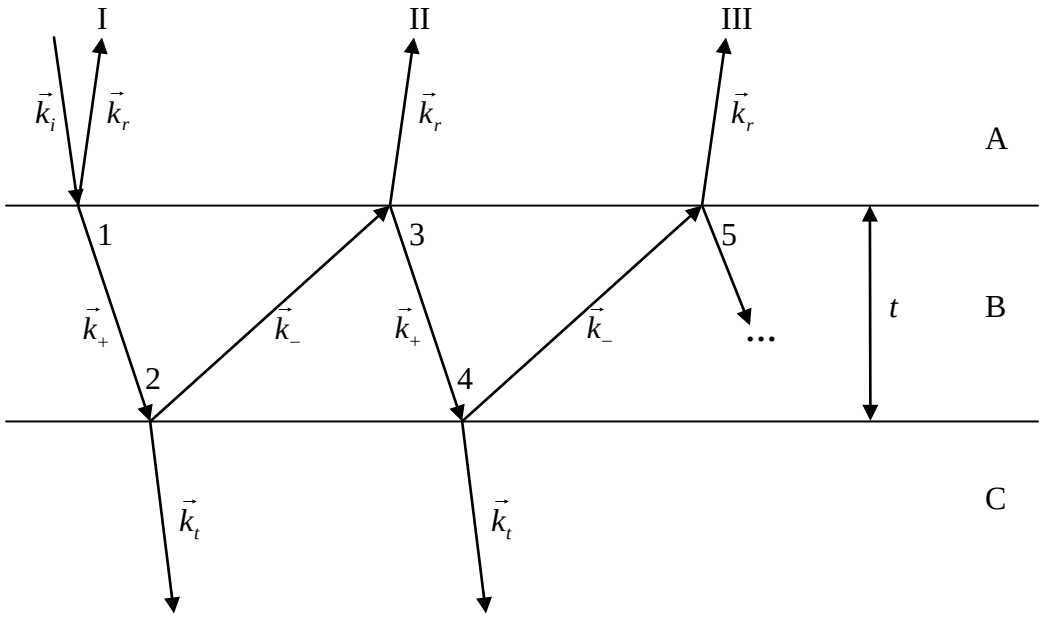

Figure C.3 Illustration of three-layer structure sandwiching an anisotropic layer.

$$r_{BA3} = \frac{\sqrt{\varepsilon_{B+}}}{\sqrt{\varepsilon_{B-}}} \frac{-k_{iz}\varepsilon_{B-} + k_{-z}\varepsilon_A}{k_{+z}\varepsilon_A + k_{iz}\varepsilon_{B+}}, \tag{C.60}$$

$$t_{BA3} = \frac{\sqrt{\varepsilon_A}}{\sqrt{\varepsilon_{B-}}} \frac{k_{-z}\varepsilon_{B+} + k_{+z}\varepsilon_{B-}}{k_{+z}\varepsilon_A + k_{iz}\varepsilon_{B+}}, \tag{C.61}$$

$$r_{BC4} = r_{BC2}, \tag{C.62}$$

$$r_{BA5} = r_{BA3}, \tag{C.63}$$

$$t_{BA5} = t_{BA3}, \tag{C.64}$$

… and so on.

Then the reflection at each point on the interface A/B can be written as:

I: $E_0 r_{AB1}$,

II: $$E_0 t_{AB1} e^{ik_{+z}t} r_{BC2} e^{-ik_{-z}t} t_{BA3} = E_0 t_{AB1} r_{BC2} t_{BA3} e^{i(k_{+z}-k_{-z})t},$$

III: $$E_0 t_{AB1} e^{ik_{+z}t} r_{BC2} e^{-ik_{-z}t} r_{BA3} e^{ik_{+z}t} r_{BC4} e^{-ik_{-z}t} t_{BA5} = E_0 t_{AB1} r_{BC2} r_{BA3} r_{BC2} t_{BA3} e^{i2(k_{+z}-k_{-z})t},$$

… and so on.

Therefore, the total reflection from the three-layer structure A/B/C is

$$r_{ABC} = r_{AB1} + \frac{t_{AB1} r_{BC2} t_{BA3} e^{i(k_{+z}-k_{-z})t}}{1 - r_{BA3} r_{BC2} e^{i(k_{+z}-k_{-z})t}}. \qquad \text{(C.65)}$$

This is equation (4.14) in chapter 4.